The background features a decorative graphic consisting of several overlapping circles in shades of blue and purple. Two thin, light-colored lines intersect at the top right, extending towards the center of the page. The circles vary in size and are arranged in a way that creates a sense of depth and movement.

*Characterisation of Melt Spun Al-Fe-Si-V Flakes and  
Process Optimization for Enhanced Mechanical  
Properties at Elevated Temperatures*

*By: NNAMCHI PAUL SUNDAY UGWU*

*Supervisor: Dr JIE ZHOU and  
Dr. JUREK DUSZCZYK*

**Department of Materials Science and Engineering  
Delft University of Technology, The Netherlands**

**APRIL, 2007**

## Acknowledgments

I would like to thank the management of Forming, Coatings and Powder Technology Group in the Department of Materials Science and Engineering and the Netherlands Institute of Metals Research (NIMR) for their financial assistance during this project and for co-funding my Master Studies, respectively.

I would like to thank Prof.ir. Laurens Katgerman, Dr. Jie Zhou and Dr.ir. Jurek Duszczyk for their support and for the provision of the laboratory facilities in the Section of Light Metals Processing. I am in a special way very grateful to my supervisor Dr. Jie Zhou for his advice and encouragement. Special thanks are due to Dr. Bogdan Lonyuk, Dr. Joanna Dzwonczyk, Dr. Simon-Peter Edwards, Dr. Dmitry Eskin and Dr. Iulian Apachitei for sharing with me their experience and practical knowledge in general aluminium alloys. I am especially grateful to Mr. Sander Leeftang, Mr. Tjeerd Tobi and Mr. Jan Boomsma for their assistance and useful discussions at the laboratory of the Light Metals Processing Section.

I am also grateful to those who have in no small measure been of great assistant to me during my study in TU Delft, in particular Chief Don Onyia, Miss. Cecilia Ikerionwu, Mrs. Okolo Modester, Mr. Ndubisi Nichodemus Nechi, Ir. Augustine Ajah, Ir. Beckley, Dr. Odo Jerome, Mrs. Sietske Zinkstok-Hoekstra and in a special way to the head of Joining and Mechanical Behaviour Section, Prof.Dr. Ian Richardson for his fatherly advice and assistance at all times.

Finally, I would like to thank my dear mother, Mrs. Angelina, and my late father, Mr. Robert Ugwu Aneke Nnamchi, and my sister, Miss. Cynthia Chinenye Nnamchi, for their efforts in making this dream come true. I am particularly thankful to my wife Mrs. Carol Hanchard Goodwin, who has been truly behind me with love and understanding during this period. I remain grateful to her.

## Summary

The use of rapidly solidified Al-Fe-V-Si (AA8009) alloy in various automotive and aerospace structures where a high strength to weight ratio is desired, started after the invention of the melt spinning technique by Mr. Pol Duwez at the California Institute of Technology and intensive research in Allied Signal. One of the main attributes exhibited by this alloy is high strength at elevated temperatures, due to low diffusivities and low misfit interfacial energies of the alloying elements in aluminium. The balance between high strength and low cost has been an added advantage to the use of this alloy. However, despite great success in developing this alloy, the market still demands further improved performance, particularly with regard to elevated-temperature strength to be comparable to titanium alloys. Elevated temperature strength requires careful control and optimization of processes from melt-spinning to extrusion.

The work presented hereafter concerns the characterisation of three batches of melt-spun Al-Fe-V-Si (AA8009) flakes, seemingly produced using similar conditions and alloying ingredients, and the optimization of elevated-temperature mechanical strength. This experimental study was conducted using optical microscopy, x-ray diffraction, wet chemical analysis, x-ray fluorescence spectroscopy, differential scanning calorimetry, microhardness, tensile tests and direct extrusion methods. Some of the conclusions are summarised below.

The results of the characterisation of the melt spun Al-Fe-V-Si (AA8009) flakes coded:  $A_1$ ,  $A_2$  and  $A_3$  corresponding to the flakes produced in 2003, 2004 and 2005 respectively, varied significantly. This is based on the microstructures, compositions and thermal analyses. Flake  $A_1$  consisted of a fine globular microstructure (Zone A) and a coarser microstructure (Zone B) in a ratio of 40 to 60%, while flakes  $A_2$  and  $A_3$  consisted predominantly of a coarser Zone B microstructure with some equiaxed dendritic features. These variations in the as-melt-spun microstructure were considered to be due to variations in solidification rates.

In addition, from the correlation analyses between the flake thickness/dendrite structures and the cooling rates, it was found that the cooling rate during the melt spinning operations decreased over the years (2003 to 2005) from  $5.2 \times 10^6$  in flake  $A_1$  to  $2.14 \times 10^5$   $\text{Ksec}^{-1}$  in  $A_3$ . These variations in cooling rate must have resulted from variations in the melt-spinning conditions.

The extrusion of the melt-spun Al-Fe-V-Si (AA8009) was characterised by a high pressure requirement rising with decreasing extrusion temperature. This was considered to be caused by a stronger internal resistance to metal flow with decreasing temperature. The material exhibited a narrow temperature window: extrusion at a low extrusion temperature of 370 °C reached the pressure limit of the press, while after a high temperature extrusion at 430 °C and at a reduction ratio of 10:1, the flakes were unaligned due to a low extrusion pressure. The low extrusion pressure peak and the unaligned microstructure with rising temperature reflects two competing mechanisms, *i.e.* strain hardening and recovery, with recovery becoming easier at higher temperatures, resulting in a decrease in strain hardening rate.

The microhardness study on flake  $A_3$  after annealing treatments at temperatures from 23 to 450 °C for 1 hr showed that 350 °C was the upper limit above which the hardness of the flakes decreased remarkably. This is considered to be due to the coarsening of the initial melt-spun microstructure due to increased instability of the dispersed particles after annealing at a high temperature. Small precipitates of a high density in this melt-spun flake tend to coarsen into larger particles of a lower density with a smaller interfacial area. This result has very important implications for the use of this material and development of high-performance elevated-temperature aluminium alloys.

The room- and elevated-temperature mechanical strengths of the extruded rods were studied by means of optical microscopy and tensile tests at 23 °C and up to 350 °C with particular reference to the extrusion and annealing temperatures. Some bands of coarsened microstructure after tensile tests at 350 °C were noted from the optical micrographs on the samples annealed for 100 hr at 300 and 350 °C. The extent of

coarsening led to undesirable degradation of properties, such as a loss in strength. Microhardness and tensile tests showed that the mechanical strength of the material decreased markedly with rising extrusion and annealing temperature especially above 300 °C. The reason was similar to that of the flakes. Volume diffusion as a rate controlling factor at a high temperature, following the relationship that diffusion coefficient and equilibrium solubility increase exponentially with temperature, implied that the interfacial energy as well as the coarsening rate of the matrix would increase rapidly with increasing annealing temperature after a considerable time.

# Table of Contents

ACKNOWLEDGMENTS .....	2
SUMMARY .....	3
<b>1. CHAPTER ONE.....</b>	<b>8</b>
1.1 Introduction .....	8
1.2 Background.....	9
1.2.1 Rapid solidification by the melt spinning technique.....	9
1.2.2 Process characteristics of the melt spinning technique .....	9
1.2.3 Effect of processing condition on ribbons .....	11
1.3 Advantages of melt spinning over the conventional ingot casting.....	13
1.4 The Melt spun aluminium alloy AA8009 (Al-Fe-V-Si).....	14
1.4.1 Microstructure development and stability of the alloy AA8009 .....	15
1.4.2 Physical Properties.....	18
1.4.3 Mechanical Properties.....	20
<b>2. CHAPTER TWO .....</b>	<b>25</b>
2.1 Materials and investigations .....	25
2.1.1 Materials .....	25
2.1.2 Experimental Methods.....	26
2.1.3 Mechanical Properties.....	31
<b>3. CHAPTER THREE .....</b>	<b>35</b>
3.1 Characteristics of the flakes.....	35
3.1.1 Compositions .....	35
3.1.2 The as-melt-spun microstructure .....	36
3.1.3 Correlation between the microstructure / flake thickness with cooling rate .....	40
3.1.4 X-ray diffraction results .....	42
3.1.5 Lattice parameter .....	44
3.1.6 Thermal analyses .....	46
3.1.7 Influence of annealing temperatures on the microhardness of the flakes .....	51
<b>4. CHAPTER FOUR .....</b>	<b>54</b>
4.1 Processing optimization for enhanced elevated-temperature properties .....	54
4.1.1 Extrusion characteristics .....	54
4.1.2 Precipitation and transformations .....	58
4.1.3 The as-extruded microstructure .....	60
4.1.4 The as-annealed microstructure .....	65

<b>4.2</b>	<b>Mechanical properties of the material as affected by extrusion and annealing temperatures.....</b>	<b>72</b>
4.2.1	Hardness .....	73
4.2.2	Tensile properties.....	74
<b>5.</b>	<b>CHAPTER FIVE.....</b>	<b>79</b>
<b>5.1</b>	<b>Discussion on the characteristics of the flakes .....</b>	<b>79</b>
5.1.1	Relationship between composition/microstructure and cooling rate.....	79
5.1.2	Relationship between exposure temperatures and flake microhardness .....	81
<b>5.2</b>	<b>Discussion on the extrusion conditions and mechanical properties .....</b>	<b>82</b>
5.2.1	Extrusion characteristics and particles/dispersoids interactions .....	82
5.2.2	Precipitation and transformation due to extrusion characteristics.....	84
5.2.3	Mechanical properties in relation to extrusion and annealing temperatures .....	86
<b>6.</b>	<b>CHAPTER SIX .....</b>	<b>87</b>
<b>6.1</b>	<b>Conclusions.....</b>	<b>87</b>
<b>7.</b>	<b>RECOMMENDATIONS.....</b>	<b>90</b>
<b>8.</b>	<b>REFERENCES .....</b>	<b>93</b>

# 1. Chapter One

## *1.1 Introduction*

Melt-spun alloys can be visualised as the materials containing micro/nano-dispersed low soluble particles embedded in a metallic matrix. The particles impart strength to the material by interaction with dislocations. Since the invention by Mr. Pol Duwez and his co-workers [1] at the California Institute of Technology, there has been a large amount of research on the rapidly solidified Al-Fe based alloys for possible applications in automotive and aerospace structures [1-5].

These alloys possess good elevated-temperature properties that are comparable with those of Ti alloys on a specific strength basis. The elevated-temperature properties of the alloys are due to the presence of thermally stable dispersoids in the microstructure. The basic requirements for forming thermally stable dispersoids in the microstructure are that the alloying elements should have a low solid solubility and a low diffusivity to have minimal coarsening during high temperature exposure [6]. The alloying elements should have high liquid solubility to allow a large volume fraction of dispersoid formed in the microstructure after rapid solidification. Furthermore, since the particles have low solid solubility in the base metal, the strengthening persists to a high fraction of the alloys melting temperature. To date, one of the most successful techniques to manufacture dispersion-strengthened alloys has been melt spinning where a molten metal is rapidly solidified by systematic contact with a rotating heat sink. A very high cooling rate realised in the process is paramount to the formation of the required dispersoids on a fine scale.

There have been several alloy systems developed and manufactured by using the melt-spinning technique. Among these, the Al-Fe-V-Si (AA8009) alloy has shown the best combinations of room-temperature and elevated-temperature mechanical properties, which makes this alloy quite suitable for applications at elevated temperatures up to 350 °C. However, recent studies have shown that the microstructure and mechanical properties of this alloy have become less desirable, due to variations in melt-spinning conditions and subsequent processing.

The present research was set up (i) to understand the variables that led to different microstructural developments during melt spinning of three batches of flakes, which were produced over a period of three years (2003 - 2005, flakes  $A_1$ - $A_3$ ), using supposedly similar conditions and alloying ingredients, and (ii) to optimize the extrusion process for enhanced elevated-temperature mechanical properties. This research was divided into two parts: characterisation of the three batches of flakes, to ascertain if identical conditions and alloying ingredients were indeed used, followed by extrusion at 370 – 460 °C and subsequent annealing treatments.

Before the work is detailed, a brief description of the melt-spinning process and the alloy used will be given.

## **1.2 Background**

### **1.2.1 Rapid solidification by the melt spinning technique**

The practice of rapid solidification involves the removal of heat from a molten material at high rates. Rapid solidification is defined as any solidification process in which the rate of change of temperature (cooling rate) is at least  $10^2$  K/sec and typically in the order of  $10^6$  -  $10^{11}$  K/sec for the melt-spinning process. The technique was invented about 35 years ago by Mr. Pol Duwez and his co-workers at the California Institute of Technology [1]. The technique involves chilling a thin layer of liquid metal by rapid heat transfer to a highly conductive and relatively cold substrate, known as the melt-spinning technique.

### **1.2.2 Process characteristics of the melt spinning technique**

Melt spinning generally involves stabilizing any molten metal stream to generate a continuous or semi-continuous filament or a thin strip. A thin layer of liquid is ejected through a slotted nozzle onto a rotating copper drum (wheel). See Fig. 1.1. One feature is that it is possible to achieve a relatively large (hundreds of degrees) supercooling of the melt before a significant amount of solid phase can form. This can result in *constitutional* changes, in that retained equilibrium phases can have

compositions outside their equilibrium limits (*solid solubility extension*), or that non-equilibrium phases can form as a result of being favoured kinetically over the equilibrium phases.

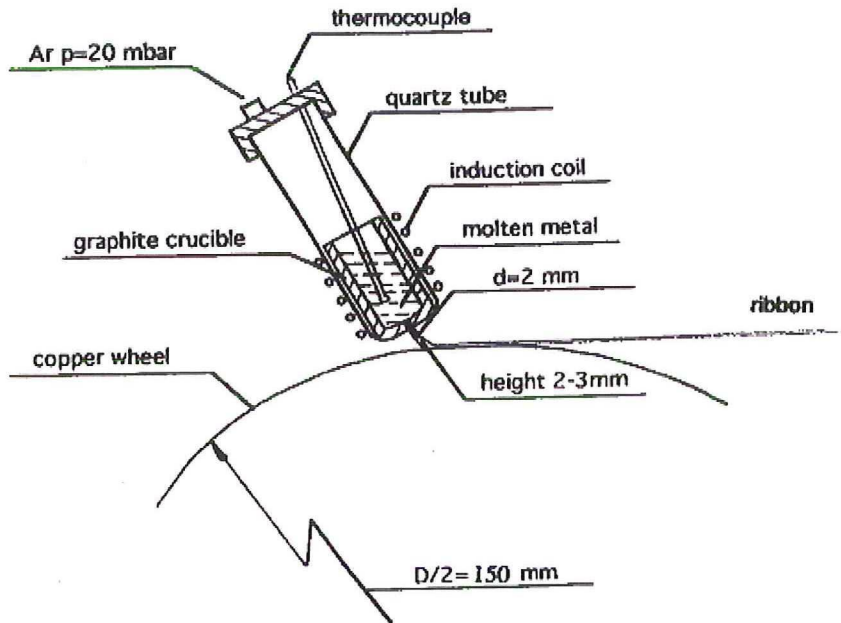


**Figure 1.1.** Schematic showing the process of melting spinning.

Principles: the liquid is pulled over the rotating drum surface (by wetting), cools and solidifies, while intimately in contact with the copper drum. According to Fourier's

law, the heat flow between the bodies is described by the relation:  $q = -kA \frac{\partial T}{\partial x}$ , where  $q$  is the heat flow, defined as the quantity of heat, transmitted in time  $t$  through a thickness  $L$ , in a direction normal to a surface of area  $A$ ; due to a temperature difference  $\Delta T$ ,  $k$  is the thermal conductivity,  $A$  is the cross-section area and  $\frac{\partial T}{\partial x}$  is the temperature gradient in the direction of flow.  $K$  is the intensive property of a material that indicates its ability to conduct heat.

The exact cooling rate of a melt-spinning operation depends on many details such as the degree of intimate contact between the melt and the rotating wheel, the thermal conductivity of both the liquid and copper wheel. One advantage of the melt-spinning technique is the achievement of cooling rates in the range of  $10^5$  to  $10^9$  K/sec [7] that

is dependent on the rapid formation of a sufficiently small dimension on the cross-section in good contact with an effective heat sink. For effective contact conditions between the metallic melt and chilling surface, standard heat flow analyses predict a cooling rate at the uncoated boundary equal to  $B/z \sim 10^2$ , where  $B$  is a function of relevant temperature interval and material properties and has a value of about  $10^4 \text{ mm}^2 \text{ K/sec}$ , and  $z$  is the surface area of the drum. The magnitude of the heat transfer coefficient  $h$  at the chilled boundary required to ensure effectively perfect contact is estimated to be about  $10^6 \text{ Wm}^{-2}/\text{K}$  for aluminium alloys. The need to ensure good thermal contact is increasingly important with an increase in desired cooling rate and a decrease in required  $z$  under the conditions of sufficiently high solidification rate [8].

### 1.2.3 Effect of processing condition on ribbons

The effect of solidification in melt spinning is characterised by the growth velocity, chemical composition, long-range order and microstructure of a growing phase. These are the functions of the local conditions at the crystal/melt interface, *e.g.* temperature, composition, orientation, curvature, crystal structure, cooling rate and wheel speed.

A previous investigation concerning the effect of wheel rotational speed on the levels of thickness that were greater than  $40 - 80 \text{ }\mu\text{m}$ , predicted on the basis of an assumed upper-limit heat transfer coefficient of  $10^5 \text{ Wm}^{-2}/\text{K}$ , showed that fluid flow and cooling rate determined the product thickness. By using the solidification time,  $\theta$  (s),  $X$  = distance from the 'nose' of the puddle to the solidification point (cm), and  $V$  = speed of the chill surface (cm/s), solidification time is given  $\theta = X/V$  [8].

Both analytical [8, 9, 10] and numerical heat flow modelling [11, 12, 13] have helped to confirm this prediction. A mathematical relationship has been employed to relate the thickness of the ribbons  $t$  to the volumetric flow rate and cooling conditions.  $t \propto Q^A U_s^{-B}$  and  $Q = v_r w t$ , where  $v_r$  is the ribbon or substrate velocity,  $Q$  is the volumetric flow rate,  $A$  and  $B$  are the constants for planar flow casting ( $A \sim 1$  and  $B \sim 1$ ) and  $w$  within a narrow range of  $0.67 - 0.83 \text{ mm}^2$  for various alloys determined for

large-scale solidification in aluminium alloy in an ingot mould or in the water-cooled mould and the secondary cooling zone of a continuous casting operation, predict a perfect relationship for the cooling rate. The similarity between glass forming and crystalline alloys suggests that both are solidification-controlled, since the solidification processes for glass formation and conventional freezing are very different.

The relative importance of fluid flow and solidification rate in determining the ribbon thickness led to several different studies on the issue. In relationship with the second

Bernoulli equation  $\frac{v^2}{2} + \phi + \omega = \text{const}$ ,  $\phi$  = gravitational potential energy per unit

mass, is given as  $\phi = gh$  in the case of a uniform gravitational field,  $\omega = \varepsilon + \frac{P}{\rho}$ , given

as the fluid thermodynamic energy per unit mass, also known as the specific internal energy and  $P$  expulsion pressure (*Transport Phenomena (Poirier & Geiger)* [14]), the relationship where  $\phi$  is related to the melt orifice diameter,  $\rho$  which is the density of the liquid metal and  $\omega$  chill-block rotational speed, is a linear one with the thickness described by the equation  $\sim \phi^2 \rho^{0.5} / \omega$ . See Fig. 1.2. [15].

Kavesh [15] concluded in his model that the results available for the dependence of  $t$  and  $w$  on  $Q$  and  $v$  were not in perfect agreement with control by either thermal or momentum boundary layers, but values were nearer to his predictions for thermal control than for momentum control. Both the details of formulation and the conclusions of Kavesh's model were questioned in the references [6, 16], leading to remodelling in terms of momentum alone and models involving combinations of thermal and momentum control [6]. Good agreement with measured values of  $t$  as a function of  $v$  for metallic-glass ribbon has been obtained both for momentum control alone and its combination with thermal control. From these studies, it has also been found that the magnitude of  $h$  is sensitive to the degree of wetting of the roll by the melt.  $h$  tends to increase with increasing  $U_s$ .

The effect of cooling rate has been a generally accepted phenomenon both in structural characterisation and analytical models. Significant variations in

microstructures and mechanical properties between the wheel side and the air side of the ribbon are evident to the variation of cooling rates. See Fig. 1.3.

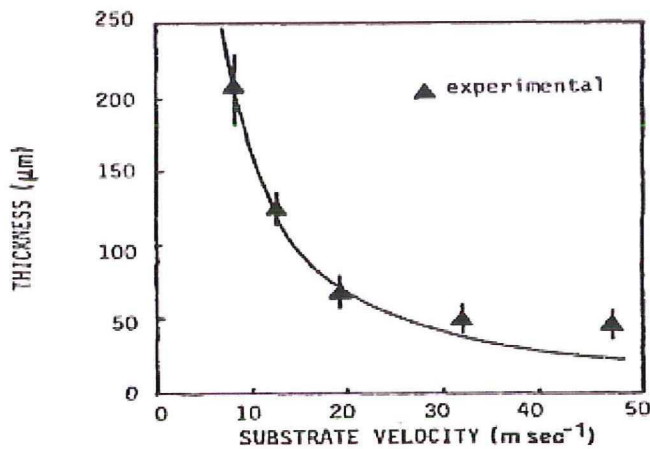


Figure 1.2 Effect of wheel velocity on the thickness of ribbon (Al-Fe alloy).

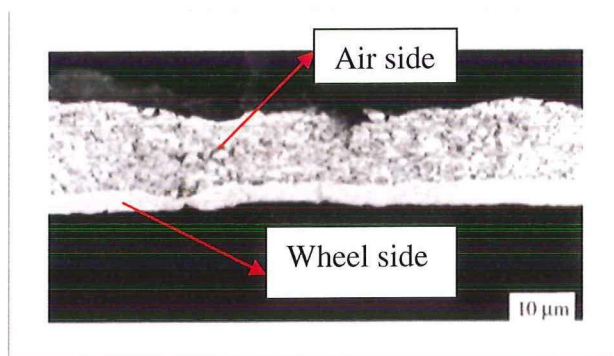


Figure 1.3 Microstructure on the cross-section of the as-cast ribbon (light microscopy).

### 1.3 Advantages of melt spinning over the conventional ingot casting

1. Ability to form a part nearer to the final shape by a shorter route with economics in input material and in final machining, resulting in cost savings as high as 10 to 30% [5].
2. Improved hot-workability due to the absence of macro-segregation and the presence of a uniform fine dendritic microstructure and grain size, allowing previously non-forgeable compositions to be rendered hot-workable and even superplastic [40].

3. Insensitivity both of processing variables and of final properties to billet size. The rapid-solidification processing route overcomes limitations in properties, such as low melting point, fracture toughness and tensile strengths [29,40].
4. Extended solid solubility of formerly insoluble and less soluble elements in the matrix of an aluminium alloy is seen as the most important property of the melt-spinning technique [5,16,17,54].
5. Improved microstructures that can lead to desirable properties over many ranges of temperatures are also an attribute inherent to this technique [1-7].

#### **1.4 The Melt spun aluminium alloy AA8009 (Al-Fe-V-Si)**

To form a thermally stable microstructure, alloying elements are required to have a low solid solubility and a low diffusivity, which should lead to a minimum coarsening rate during high temperature exposure [16]. A high liquid solubility will also be necessary for a high volume fraction of dispersoids in the microstructure. A balancing factor to all the qualities is that the required dispersoids formed from these elements during rapid solidification are on a fine scale.

Since the kinetics of coarsening is controlled by volume or bulk diffusion, the most likely candidate elements to alloy with aluminium for elevated-temperature strength are those of low diffusivities and low misfit interfacial energies. From the investigations reported in the literature [16, 17], vanadium and iron are the two prime choices as the slowest moving elements in aluminium. See Table 1.1. Rapid solidification results in grain refinement, with grain sizes typically in the range from 1 to 10  $\mu\text{m}$ . Aluminium-based alloys (*e.g.* Al-Fe-Si-V) [18] can be rapidly solidified and consolidated via hot isostatic pressing (HIP) and extrusion to produce structures which contain small (about 50 nm) dispersoids of a cubic phase with very low coarsening rates.

Among various quaternary compositions of the alloy proposed, AA8009 and AA8019 remain the serious candidates for high-temperature (250 - 300  $^{\circ}\text{C}$ ) applications. In this report, emphasis will be placed on the AA8009 alloy, which was examined in more detail by many researchers. The research to understand the properties and deformation

mechanisms of this alloy was performed essentially first at Allied Signal and then at ONERA [19].

**Table 1.1** Diffusivity, liquid and solid solubility of some transition metals in aluminum

<i>Transition metal</i>	<i>D (cm<sup>2</sup> s<sup>-1</sup>) at 618 K</i>	<i>Liquid solubility at 1400 K (wt.% (at.%))</i>		<i>Maximum equilibrium solid solubility at indicated temperature (wt.% (at.%))</i>		
Fe	$5.4 \times 10^{-14}$	32	(18.52)	0.04	(0.025)	at 928 K
V	$7.4 \times 10^{-15}$	1.6	(0.85) <sup>a</sup>	0.6	(0.32)	at 934 K
Zr	$3.4 \times 10^{-18}$	11.5	(3.7)	0.28	(0.085)	at 934 K
Cr	$1.1 \times 10^{-12}$	15	(8.4)	0.77	(0.40)	at 934 K
Ce	$8.4 \times 10^{-16}$	41.5	(12)	0.05	(0.01)	at 910 K
Mo	$2.4 \times 10^{-14}$	3	(0.86)	0.25	(0.056)	at 934 K
Ti	$1 \times 10^{-16}$	6.3	(3.6)	1.3	(0.57)	at 938 K

<sup>a</sup> At 1200 K.

#### 1.4.1 Microstructure development and stability of the alloy AA8009

Several reports on the microstructure of ribbons produced by the melt-spinning technique showed varying microstructures that were correlated to the processing conditions. The wheel side and the other side freely exposed to air had remarkable differences in their structural features and properties. The ribbons had microstructures made up of a nearly structure-less part on the wheel-side, while on the free side, the silicide particles were about 1  $\mu\text{m}$  in diameter and less global in structure. These microstructures were influenced by the solidification rate. The structures were generally classified as Zone A (microcellular) and Zone B (cellular) and sometime Zone 'O' which was a mixture of both the A and B structures. See Fig. 1.4. Transmission electron microscopy images clearly demonstrated the size differences in silicide particles on the cross section of the ribbons [16, 19, 20, 21].

The microstructure consisted of very fine, nearly spherical quaternary intermetallics with a general composition  $\text{Al}_{13}(\text{Fe},\text{V})_3\text{Si}$  (bcc-silicide dispersoids homogeneously or sparsely distributed throughout the aluminium matrix with a lattice parameter of about 1.26 nm [20, 22]). They were described as empty (Fe+V) icosahedra, *i.e.* with an unoccupied centre situated at the sites of a bcc lattice, all parallel to and connected to its eight neighbours along the three fold axes parallel to its  $\langle 112 \rangle$  direction. The

connecting atoms formed a slight distorted octahedron. Each of these (Fe+V) icosahedra contained an empty (Al+Si) icosahedron of the same orientation and these were connected through a chain of empty (Al+Si) octahedrally sharing triangular faces. See Figs. 1.5a and b. The elevated-temperature stability of the alloy is due to the slow coarsening rate of silicides homogeneously distributed within the aluminium matrix. The coarsening rate of the silicide phase formed by this alloy is  $2.9 \times 10^{-26}$  to  $8.4 \times 10^{-7} \text{ m}^3/\text{hr}$  at room temperature and  $425 \text{ }^\circ\text{C}$ , respectively [14]. The microstructure in the quaternary alloy is seen as a carry-over of the formerly unreported microstructures found by Jones [23] and categorized into three zones: Zone A (wheel side), Zone B (free-air side) and the probable combination of Zone A and Zone B (referred to as Zone O).

Bendersky and his co-workers and some others sharing the same view [24] linked the microstructures to the alloy composition and suggested that the fine precipitates were due to segregation during solidification rather than solid-state decomposition after solidification, because of their random orientations with respect to the  $\alpha$ -Al matrix. Other authors like Park *et al* [25] attributed these to the effect of post-solidification cooling (rather than the effect of alloy composition). The formation of the final microstructure near the wheel side in the form of globular particles suggested that they did not form as the primary phase. Rucingdaj *et al* [26] claimed that, in the case of the material produced from atomised powder, the size of powder particle exerted the most influence on microstructure than any other factors. The extrudates produced from thin ribbons were said to exhibit microstructures containing ultra fine spherical particles distributed homogeneously throughout the  $\alpha$ -Al matrix.

There has been a general understanding of the effect of cooling rate on microstructure. The scale of the microstructure depends upon cooling rate, which is directly related to the ribbon thickness. The difference in microstructural scale is clearly visible in Fig. 1.6 which shows the microstructures of the 30 and 250  $\mu\text{m}$  thick ribbons. The investigations made by Kalkanli *et al* [21] concluded that (i) increasing solidification rate refined the dispersoid size for both gas-atomised and melt-spun Al-Fe-V-Si alloy and (ii) average dispersoid sizes for the as-melt-spun ribbons measured by TEM were 0.02 – 0.06  $\mu\text{m}$  for 30 – 250  $\mu\text{m}$  thick ribbons, having a possible cooling rate of

$10^5 - 10^6 \text{ Ksec}^{-1}$ , similar to the results obtained from melt-spinning experiments reported by previous investigators [27,16]. After annealing for 1 h at 473 K, the microstructure appeared coarser and the spherical particles with sizes between 0.3 and 1  $\mu\text{m}$  were found, but not uniformly distributed in the matrix [16].

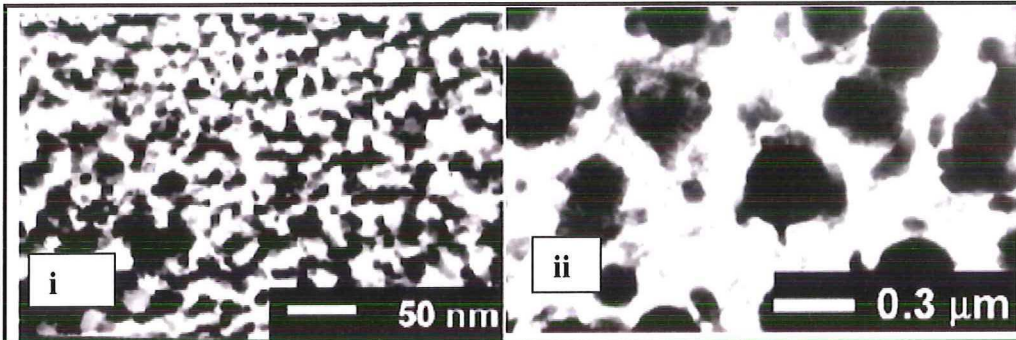


**Figure 1.4.** TEM analysis: (i) spherical particles on the wheel-side of the ribbon; (ii) spherical particles at the free side of the ribbon.

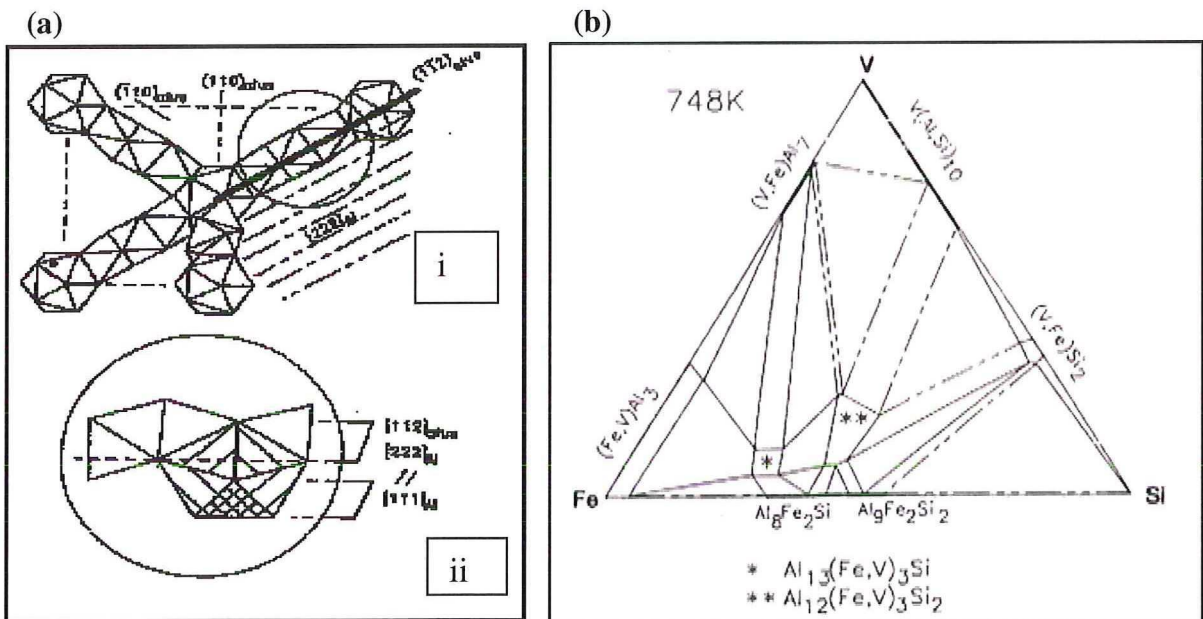


**Figure 1.5.** (a) (i) Schematic representation of a (110) plane through the silicide plane showing the orientation relationship with the matrix, (ii) schematic illustration of the localized 5 fold symmetry atomic bonding between the aluminium matrix and the (Al+ Si) octahedral within the silicide phase and the relationship found. (b) The equilibrium phases within the quaternary alloy at 748 K.

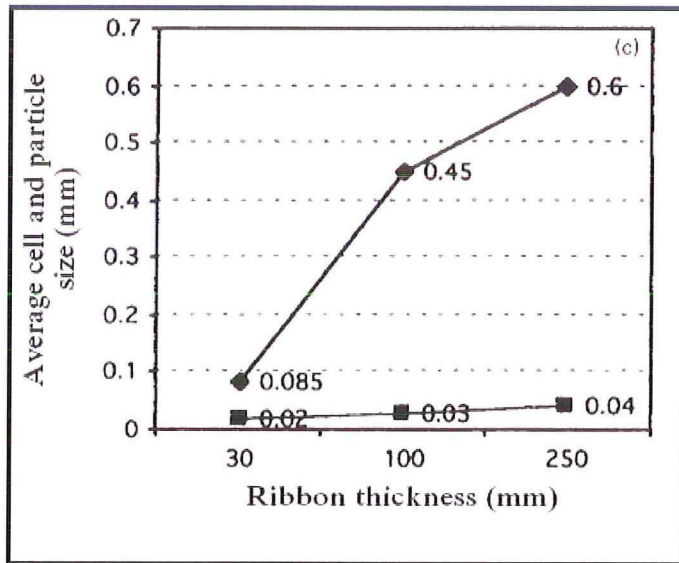


Figure 1.6. A correlation between ribbon thickness and ◆ average cell and ■ particle size.

## 1.4.2 Physical Properties

An important physical property is the nature of the interface existing between the silicide phase and the aluminium matrix in consideration of the coarsening rates within the alloy system. Of equal importance are the modulus and thermal expansion coefficient. A TEM analysis by Skinner and his co-workers [28] showed that the aluminium matrix and the silicide phase had the following orientation relationship:

$$[112]_{(Fe,v)} // [222]_{Al} // [111]_{Al}$$

$$\langle 111 \rangle_{(Fe,v)} // \langle 110 \rangle_{Al}$$

Ledges which were found at the interfaces between these two phases were attributed to a result of the crystal structure of the silicide phase. The octahedral chains linking the (Al+Si) icosahedra lay on the {112} planes and the size of these octahedral chains were very close to that of the octahedral in the aluminium matrix. The angle between the {112} planes in the silicide and the {222} planes was also the same (109.47°), thus providing further evidence about the nature of the interface. The combination of this orientation relationship, ledge formation and high site interface (with five fold symmetry) resulted in a low interfacial energy and a low driving force for the coarsening of the silicide phases in the AA8009 alloy [28]. See Fig. 1.5.

The changes in lattice parameter were considered to be caused by the solid solubilities of the elements and the resultant volume fraction, mostly of the Fe:V ratio in the dispersoid. Investigations on the coarsening rates of the dispersoids within this alloy offered some indications of reasonable changes in matrix/dispersoid interfacial energy at an increased volume fraction due to varied Fe:V ratios. The data indicated that there was a greater relationship between the volume fraction of the compound related to the Fe:V ratio and increased strength and stability of the alloy (constant volume fraction and lattice parameter) [16]. Both dynamic fracture toughness and coarsening rate data gave the correlation of the changes in the interfacial energy between the aluminium matrix with the cubic dispersoid with an Fe:V ratio [16].

The measurements of the thermal expansion coefficient of the silicides vary from one investigator to another. Skinner gave a value of  $11.6 \times 10^{-6}$  m/m/K [16, 28], while Allied Signals had a value  $22 \times 10^{-6}$  m/m/K in its patent [27]. The variation could be due to varying alloy compositions and conditions. Young’s modulus was found to be about 110 GPa which was also correlated with the volume fraction of the silicide particles[5]. See Figs. 1.7a and 1.7b and Table 1.2.

**Table 1.2.** Physical properties of the dispersion-strengthened alloy AA8009.

<b>Density Mg/m<sup>3</sup></b>	<b>2.92</b>
<b>Melting point K</b>	<b>933</b>
<b>Thermal expansion coefficient /K</b>	<b><math>22 \times 10^{-6}</math></b>
<b>Electrical resistivity, micro Ohm cm at 25 °C</b>	<b>6.3</b>
<b>Useful service temperature</b>	<b>400 °C</b>
<b>Thermal conductivity, W/cm/K</b>	<b>1.05</b>

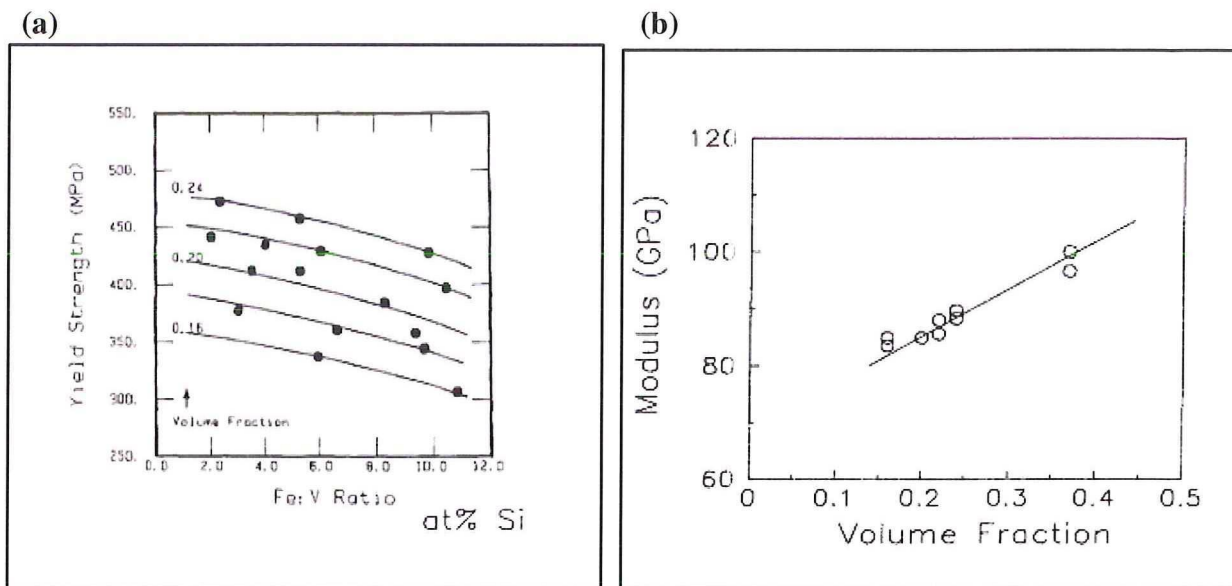


**Figure 1.7.** (a) Effect of Fe: V ratio and volume fraction on yield strength and (b) modulus vs. volume fraction of the silicide particles.

### 1.4.3 Mechanical Properties

The mechanical properties of the alloy depict the effect of the dispersoids as well as the volume fraction of the intermetallics within the matrix. These two factors exhibit an overlap in data, which is attributed to the role that they play in the strengthening of the material. These descriptions point to the fact that up to a temperature of 500°C the deformation mechanism is obstacle-controlled glide. Above this temperature, the mechanism changes to diffusional flow and the sizes of the dispersoids will not have any effect on the strength of the material.

**Tensile and fractural properties:** The mechanical properties of the nano-metric dispersion-strengthened AA8009 alloy are far superior to those of micro-metric dispersion-strengthened alloys with a similar volume fraction of particles. The evolution of the 0.2% proof strength with temperature is shown in Fig. 1.8a. The proof strength of this dispersion-strengthened aluminium alloy is attributed to the low solubilities of the alloying elements in the aluminium matrix. An investigation by Skinner [27] raised the concern for an increased volume ratio of Fe:V in the AA8009 alloy. Alloys with an Fe:V ratio of 9.82:1 has a slower coarsening rate than the alloy that has an Fe:V ratio of 2.35:1. Both were shown to have much slower coarsening rates than for an Al-12wt. % Fe alloy at a temperature of 698 °C.

The reported yield strength value of the alloy AA8009 is about 400 MPa at room temperature and 270 MPa at 523 K. Furthermore, it can be seen from Fig. 1.8b that the yield strength values are similar in the longitudinal (L) and transverse (T) directions. Improved strength and stiffness at elevated temperatures compared to other rapidly solidified alloys are due to the presence of fine-scale inert dispersions,  $Al_{12}(Fe, V)_3Si$ , which stabilize the structures at high temperatures.

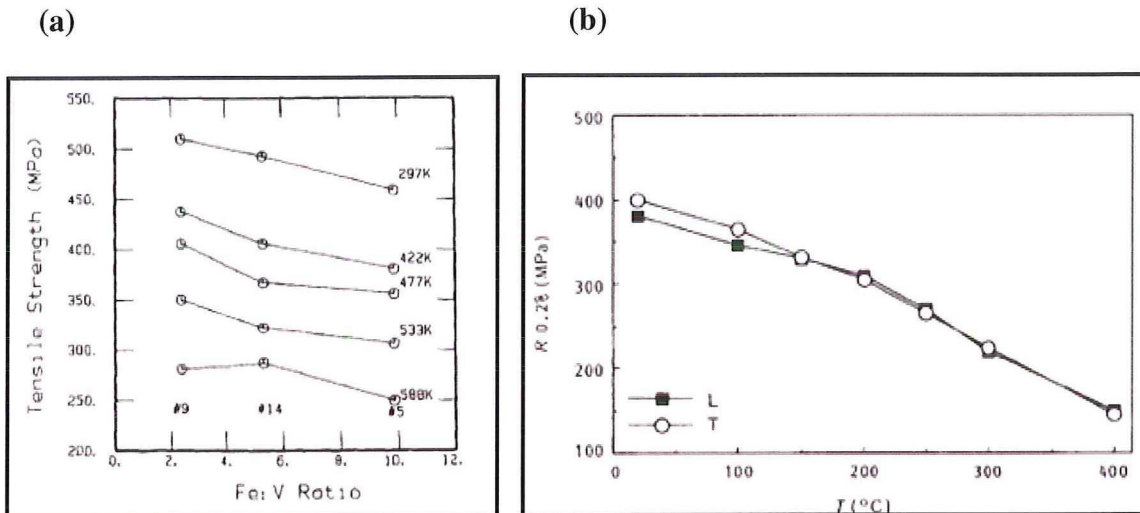


**Figure 1.8.** (a) Ultimate tensile strength vs. Fe: V ratio and (b) 0.2% proof strength of the AA8009 alloy as a function of temperature. L = longitudinal (parallel to the extrusion direction), T = transverse.

The rate of strain hardening in the rapidly solidified AA8009 alloy was found to increase with increasing volume fraction of dispersoids and decreasing particle size [30]. The fracture toughness ( $K_{1C}$ ) is about  $15 \text{ MPa}\sqrt{m}$  [31], being independent of temperature. The material is directionally textured to have better toughness when measured in the lateral -transverse regions. Fracture crack propagates parallel to the tensile direction, or in the longitudinal direction instead of the transverse direction. This directionality of the microstructure of thick extruded product is responsible for the anisotropy properties [30], since it provides preferential paths for cracks between the strips. On the basis of tensile tests, the ductility of thin products shows no anisotropic [29].

After exposure for 100 hours, the alloy does not show any significant changes in fracture toughness up to a temperature of 703 K. See Fig. 1.9. The low ductility and toughness at this temperature with the T-L orientation are attributed to the influence

of anisotropic properties as well as to micro-precipitation [29]. Fig. 1.9 gives the room-temperature strength stability of the alloy after exposure to temperatures up to 755 K for 100 hr. The intermetallic silicides  $Al_{12}(Fe,V)_3Si$  in this alloys have a remarkable resistance to coarsening and exhibited only a 10% reduction in strength after 100 hr annealing at 755 K [27].

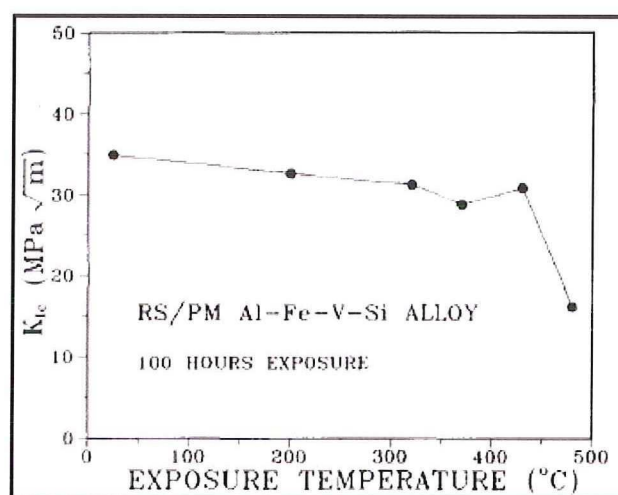


**Figure 1.9.** Variation of room-temperature fracture toughness with exposure temperature for Al-Fe-V-Si alloy.

**Creep behaviour:** The high-temperature creep strength of this alloy is greatly improved by the addition of the nano-structured and stable dispersed silicide phase, due to grain boundary pinning. It is different from the alloys strengthened by grain refinement, which is not desirable in high-temperature materials, as it results in a higher rate of grain boundary sliding, a key mechanism of creep. For this reason, the dispersion-strengthened alloy in general has a creep resistance better than the conventional cast alloys. Therefore, dispersion strengthening is of particular importance in creep-resistant alloys. The creep behaviour of this dispersion-strengthened alloy (AA8009) was investigated in the temperature range of 573 – 723 K [30].

The alloy exhibits a high apparent stress exponent of 5 and high apparent activation energy for creep (296 kJ/mol). See Fig 1.10. The result obtained indicates the dislocation–climb mechanisms providing the resistance needed for creep. The dislocation creep theories neither lead to correct values nor explain the origin of the

temperature dependence of the threshold stress, other than that attributable to the shear modulus [31]. The reason for the difference is attributed to the modification of the chemistry of grain boundaries in aluminium, due to the low solubility of most of the alloying elements in the alloy [30].

Creep tests of this alloy at temperatures between 510 and 752 K showed the tensile strength level preceded 90% of its compressive strength [31]. The slope of the curve for the stress exponent and stress indicates that the deformation mechanism changes from obstacle-controlled glide to diffusional creep at high temperatures. See Fig. 1.10 [31].

**Corrosion resistance:** The excellent thermal stability exhibited by this alloy leads to the applications at high temperatures and in corrosive environments. The delay in the onset of capitation and the corrosion resistance of this alloy were attributed to the fine silicides, which were homogeneously distributed in the matrix [31].

The corrosion resistance of the aluminium alloy extends to its resistance to stress corrosion cracking (SCC). The threshold stress for SCC is essentially the yield strength. An investigation of extruded sample stressed to 360 MPa, 95% of tensile yield strength, in the short transverse direction, did not fail after 100 hr in 3.5% sodium chloride. See Fig. 1.11 [27].

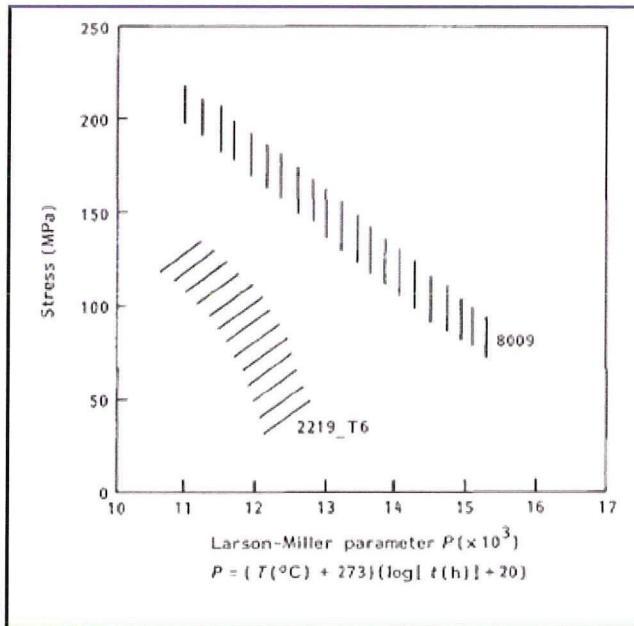


Figure 1.10. Creep rupture properties of AA8009 compared to the 2219 aluminium alloy.

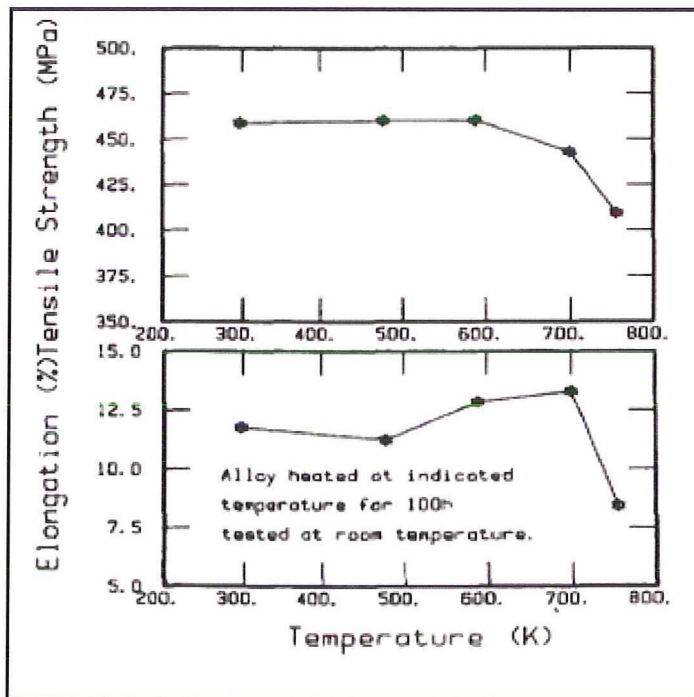


Figure 1.11. Tensile strength of the alloy after exposure at 755 K for 100 hr.

## 2. Chapter Two

### 2.1 Materials and investigations

This chapter is meant to provide information about the materials, investigation methods and the types of equipment used for the study. Fig. 2.1 illustrates the process techniques that were used for the characterisation of the melt spun flakes and for the optimization of the elevated-temperature mechanical properties of the material. The flakes were consolidated by cold compaction with a laboratory press prior to extrusion. The composition and microstructure analyses of the flakes were investigated by optical microscopy, wet chemical analyses, X-ray diffraction and differential scanning calorimetry. The correlations between extrusion temperature and pressure were employed to determine the extrusion characteristics and the limits for the alloy within the prevailing laboratory conditions. Furthermore, microhardness and tensile tests at room and elevated temperatures were carried out to verify the effects of extrusion temperature and demoisturing prior to extrusion on the mechanical properties of the material.

#### 2.1.1 Materials

The flakes used for this study were supplied by RSP Technology in the Netherlands. The flakes were seemingly produced using similar conditions and alloying ingredients. In this work, the materials were coded:

$A_1$  = flakes produced in 2003

$A_2$  = flakes produced in 2004

$A_3$  = flakes produced in 2005

$B$  = hot isostatic pressed billet produced from flakes  $A_3$  (upper surface region of the billet),

$C$  = the as-received extruded rod produced from flakes  $A_3$ .

$D$  = cold compacted and extruded rod experimentally produced from flakes  $A_3$  (present research)

Note that only flake  $A_3$  (2005 batch) was provided for the extrusion experiment.

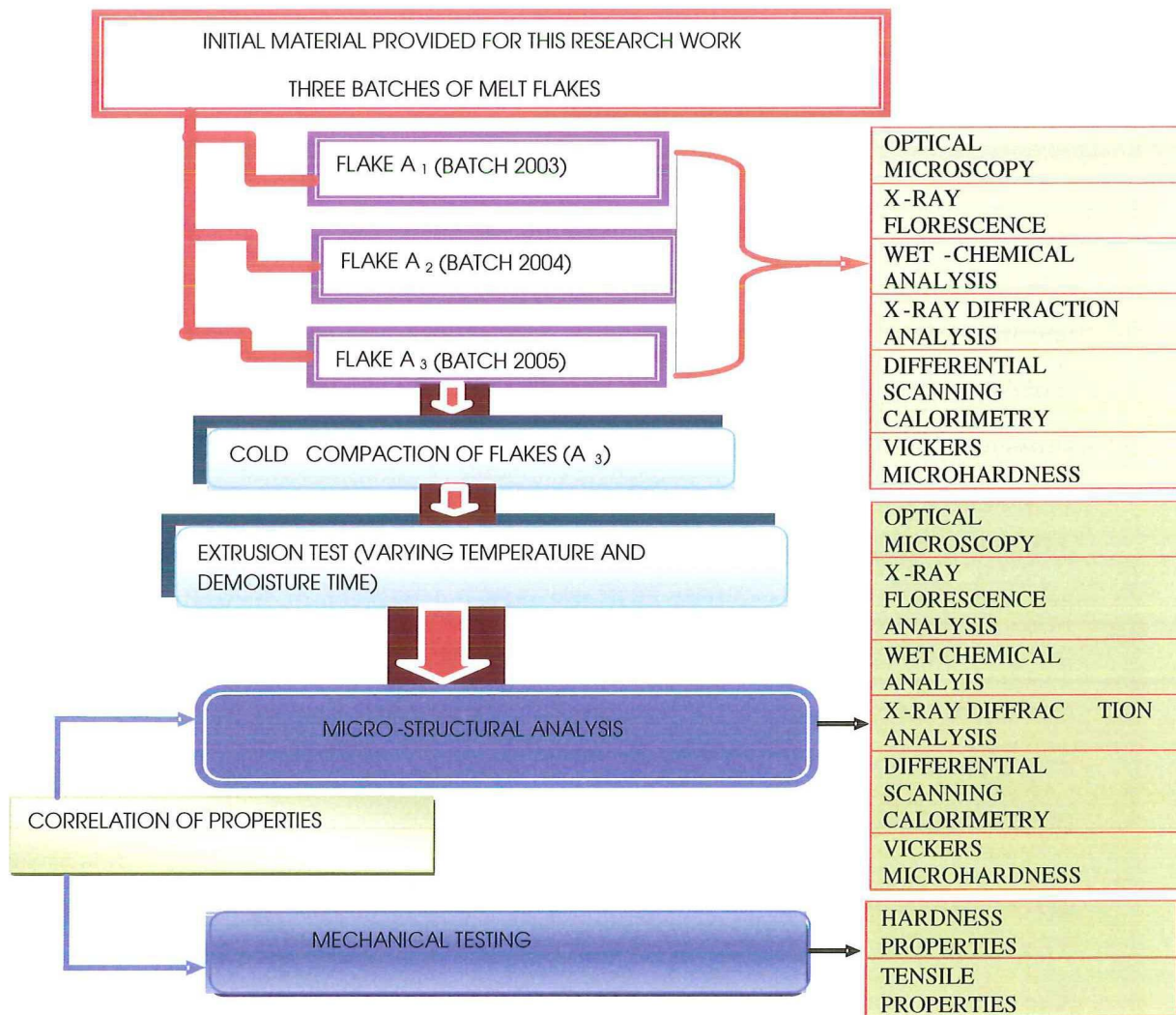
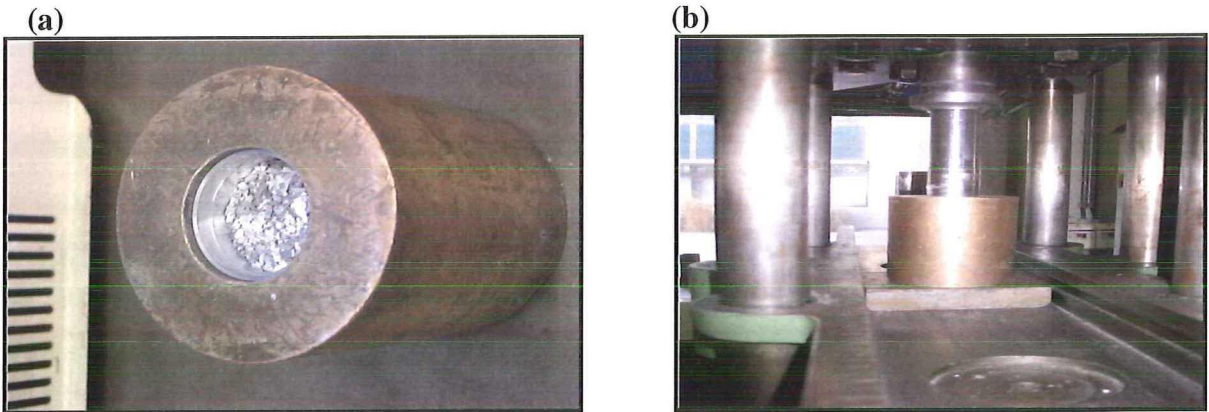


Figure 2.1 Flow chart describing the experimental procedures for the study

## 2.1.2 Experimental Methods

### 2.1.2.1 Compaction

The preliminary consolidation was done by cold compaction using an Amsler laboratory press to 80% of the theoretical density under a load of 30 tons applied to the ribbons in an aluminium container with a length of 121.8 mm and an inside diameter of 45 mm. During this process, zincstearic acid was used as the lubricant between the aluminium container and the die to reduce the friction between them. See Fig. 2.2. The billets were subsequently demoistured by a preheating treatment at 150 °C for various times between 0 – 300 min before extrusion.



**Figure 2.2.** (a) The flakes having been compacted on the container and (b) shows the setup used for the compaction of the flakes.

### 2.1.2.2 Extrusion

Extrusion is usually the first thermomechanical processing step applied in forming high-strength melt-spun flakes after compaction. As the name *thermomechanical* implies, it incorporates both mechanical working and thermal treatment by intensely shearing the flakes, breaking up the surface layer of oxide, while the force and heat generated by the process allow the compacted flakes to weld together easily in the solid state. A large proportion of the mechanical work used during extrusion is converted to heat, leading to an increase in temperature in the deformation zone. See Fig. 2.3.

The most important variables in extrusion are temperature, ram speed and reduction ratio. In the present investigation, ram speed and reduction ratio were kept constant while billet temperature was varied. The correlation between extrusion temperature and pressure at a constant ram speed and reduction ratio, together with microstructure and strength, was used to determine the extrusion window of the material. This is because the extrusion pressure is said to be directly related to the internal resistance of the material to deformation [56].

In the present work, the as-compacted billets were extruded at temperatures from 370 to 460 °C at a constant reduction ratio of 10:1 and a ram speed of 2 mm/sec using a 250 MT direct (horizontal) laboratory press. During extrusion, the variation of pressure as a function of temperature and ram displacement was recorded. The extrusion temperatures were measured by inserting a thermocouple into a hole at the

centre of the extrusion die, while the extrusion pressure was registered by a sensor within the hydraulic system. The billets were extruded into 10 mm x 2 mm strips horizontally by pushing the cylindrical billet in the container towards the stationary round shaped die ( $\phi = 15.8$  mm). Upon leaving the die the strip was cut by a clamp through the die opening and gradually pulled out. The extruded strip was then allowed to cool down in air. The effect of demisting on the extrusion conditions was investigated by holding the billet in a furnace at 150 °C for various times varying between 0 to 300 min.

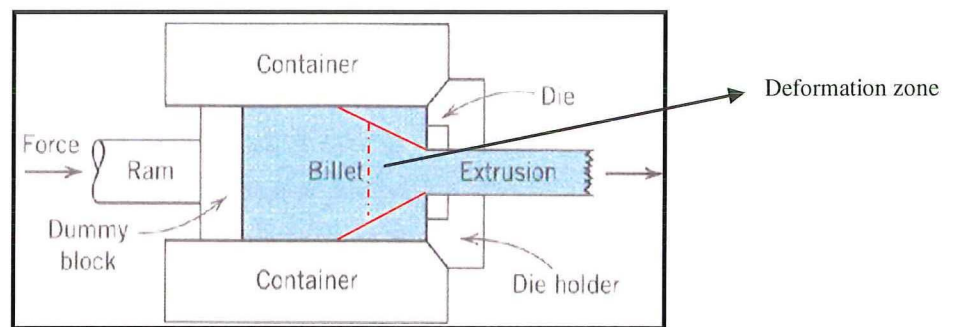


**Figure 2.3.** Schematic representation of direct extrusion process

### **2.1.2.3 Characterisation techniques and procedures**

To assess the physical and mechanical properties of the ribbons in relation to the as-received extruded rods, the extruded samples were separately heat treated at 200, 300 and 350 °C for 100 hr. The characterisation included chemical composition, phase transformation and microstructure/morphology. These were followed by the evaluation of mechanical strengths at room and elevated temperatures by microhardness and tensile tests (UTS, elongation and yield strength) at elevated temperatures (100, 200, 300 and 350 °C).

#### ***2.1.2.4 Wet chemical analysis***

In order to qualitatively verify the differences in composition between the ribbons and the as-received extruded rod, wet chemical analysis was used to characterize the flakes. The technique of the wet chemical analysis by flame atomic absorption spectroscopy (FAAS) requires a liquid or dissolved sample to be aspirated, aerosolized and mixed with combustible gases, such as acetylene and air or acetylene and nitrous oxide. The mixture is ignited in a flame whose temperature ranges from 2100 to 2800 °C. During combustion, the atoms of the element of interest in the sample are reduced to free, unexcited ground state atoms, which absorb light at characteristic wavelengths.

The characteristic wavelengths of this technique are element specific to the accuracy of 0.01 - 0.1 nm. To provide element specific wavelengths, a light beam from a lamp whose cathode is made of the element being determined is passed through the flame. A device such as photon multiplier can detect the amount of reduction of the light intensity due to absorption by the analyte, and this can be directly related to the amount of the element in the sample. This technique is one of the best so far in determining the composition of an aluminium alloy.

#### ***2.1.2.5 Optical Microstructure analyses***

The microstructures of the flakes and the extruded billets were examined by using an optical microscope in order to monitor the changes that occurred during the processing of the sample. The microscopic observations were performed using a Neophot 2" optical microscope. Images were recorded with a Nikon DXM 1200 camera attached to the microscope and evaluated using an Aquinto software image processing program. Some of the observable differences included the features such as dendrite arm spacing, phase/particle distributions and structures/sizes in the microstructure of the samples.

The steps followed in preparing a highly polished surface were cutting, mounting of a specimen on a cylindrical polymer resin, grinding using various grades of abrasive paper and polishing with a 3  $\mu\text{m}$  diamond paste automatically in a machine (Figs.

2.4a and b) before etching with the Keller's reagent (consisting of  $\text{HBF}_4=50\%$ ) and Wilcox etchant, Nital (2%), and ethanol) for 3 second. This was found to be appropriate for the material to reveal the features of interest in the sample (grain structure and size, distribution and shape of dispersoids and type of the phases / inclusions). There was followed by the microstructure investigation using Neophot 2'' optical microscope.

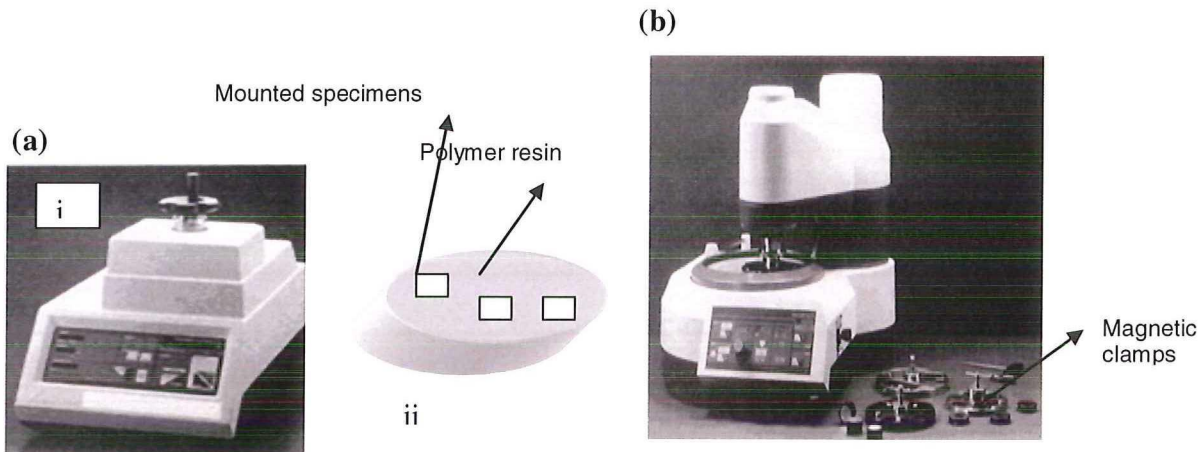


**Figure 2.4.** (a) (i) Automatic mounting machine and (ii) mounted samples. (b) an automatic polishing machine.

#### 2.1.2.6 X-ray diffraction analysis

The flakes and the extruded samples were analysed with a diffractometer type Bruker-Nonius D5005. Lattice parameter measurements were made using a high purity Si monochromator that had a  $\{511\}$  orientation as a standard on X-ray diffractometer with  $\text{Co K}\alpha$  radiation. Diffraction patterns were recorded in the step-scan mode at steps of  $0.02^\circ$  ( $2\theta$ ) and a counting time of 3 sec per step, in the angle interval from  $15^\circ$  to  $130^\circ$  ( $2\theta$ ). The samples represented rectangular pieces of compacted ribbons with dimensions of  $10 \times 15$  mm and flakes of  $3 \times 1$  mm. This  $\{511\}$  orientation had no reflection and therefore would not interfere with the reflections from the sample. Cobalt beam  $\lambda$  reflection of  $1.789 \text{ nm}$  and energy  $0.6931 \text{ KeV}$  was used instead of copper, because copper reflections would cause a fluorescence effect in the present alloy containing iron as one of its major alloying element leading to high background noise, while cobalt tended to reduce this background noise. However, the inherent low reflection of cobalt was a disadvantage to its use. The use of the cobalt beam for the

X-ray analyses of this alloy with a density of  $2.92 \text{ g/mm}^3$  showed by the calculated absorption (photoelectric + Compton's effect + Rayleigh) that 90% of the diffracted beam would contribute to a  $37.68 \text{ }\mu\text{m}$  penetration depth in the sample.

### 2.1.2.7 Differential Scanning Calorimetry

The Stanton Redcroft 1200 DSC (Fig. 2.5) instrument was used to study the phase transformations, precipitation reactions and the stability of the flakes and the extruded material. In the broadest sense, this thermal analysis technique refers to the measurement of changes in the properties of substances under a controlled temperature program. Calorimetry generally involves the thermal analyses that measure the heat evolution from a sample under a controlled temperature program. The program used for the present analysis involved heating (scanning) a  $0.012 \text{ g}$  sample at a constant rate of  $20 \text{ }^\circ\text{C}$  per min from  $200$  to  $800 \text{ }^\circ\text{C}$ . At this temperature, the material was held isothermally for  $5 \text{ min}$  before cooling. The signals were used to measure the transformations or reactions which led to heat flows and temperature changes.



**Figure 2.5.** The differential scanning calorimeter used for the study.

### 2.1.3 Mechanical Properties

To establish the effects of extrusion conditions and annealing treatment on the mechanical properties, exposure time and temperature combination were selected based upon potential applications and material characteristics. Tensile tests and

hardness measurements were conducted on the samples after an exposure for 100 hr at temperatures of 100, 200, 300 and 350 °C. The effect of temperature on typical yield strength and ductility at elevated temperatures were established by correlating these annealing temperatures with microhardness and tensile properties.

### 2.1.3.1 Microhardness

The term microhardness test is used to refer to static indentation made with a load not exceeding 1 kg/mm<sup>2</sup> using a diamond pyramid indenter. The procedure for testing is very similar to that of the standard Vickers hardness test, except that it is done on a microscopic scale with higher precision instruments. The surface of the samples were polished prior to the measurement under a 0.1 N (10 g) load using Reichert and Leitz Vickers equipment affixed on a precision microscope. The magnification of the microscope used was 500 and it measured the indentations to an accuracy of  $\pm 0.05 \mu\text{m}$ . Also with the microscope, an observer differences of  $\pm 0.2 \mu\text{m}$  could usually be resolved. See Fig. 2.6b.

The Vickers diamond pyramid indenter presses upon the sample in the form of a squared pyramid with an angle of 136° relative to the surface of the sample. See Fig. 2.6a. The depth of indentation is about 1/7 of the diagonal length. When calculating the Vickers Diamond Pyramid hardness number, both diagonals of the indentation are measured and the mean of these values is used in a formula with the load used to determine the value of hardness. This Vickers Diamond Pyramid hardness number is given by the applied load (kg/mm<sup>2</sup>) divided by the surface area of the indentation

$$(\text{mm}^2) \quad HV \approx \frac{2F \sin \frac{136^\circ}{2}}{d^2} \quad HV \cong 1.854 \frac{F}{d^2} \quad \text{Where } F = \text{load in kg/mm}^2, \quad d = \text{arithmetic}$$

mean of  $d_1$  &  $d_2$  in mm.  $HV$  = the Vickers hardness.

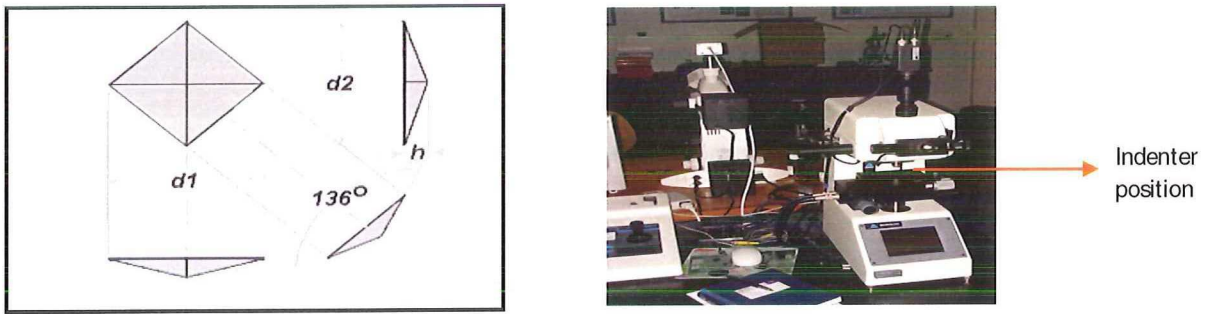


**Figure 2.6.** (a) Vickers pyramid diamond indentation description. (b) Vickers microhardness tester.

### 2.1.3.2 Tensile tests

In order to test the mechanical strength of the material after extrusion, uniaxial tensile tests were performed by using a constant strain rate of  $3.3 \times 10^{-3} \text{ sec}^{-1}$  between 23 – 350 °C. All the experiments were carried out using an Instron testing machine (Model TT-c-L) with a calibrated load cell of 100 kN, which was equipped with a microprocessor. Cylindrical specimens were machined from the as-extruded material, with a gauge length of 20 mm and diameter was 4 mm. See Fig. 2.7. To investigate the mechanical response at elevated temperatures the machined specimens were tested at four different temperatures (room temperature, 200, 300 and 350 °C), after annealing for 100 hr at 100, 200, 300 and 350 °C. The furnace used for the high temperature tensile experiments had three controlling heat elements (top, centre and bottom) that enabled it to achieve excellent temperature control during tensile testing. Two thermocouples were placed in touch with the specimen necks to help measure the testing temperature accurately according to standard described in ASTM E8. See Fig. 2.8.

Three main parameters which the Instron data file recorded automatically in the program that was used to calculate the mechanical properties of the material were time, force and elongations. The 0.2% proof stress is defined as the stress needed to produce a permanent strain of 0.2% based on the gauge length. It is used instead of yield stress in the present material that did not exhibit pronounced yielding. Ultimate tensile strength was the strength at which failure occurred.

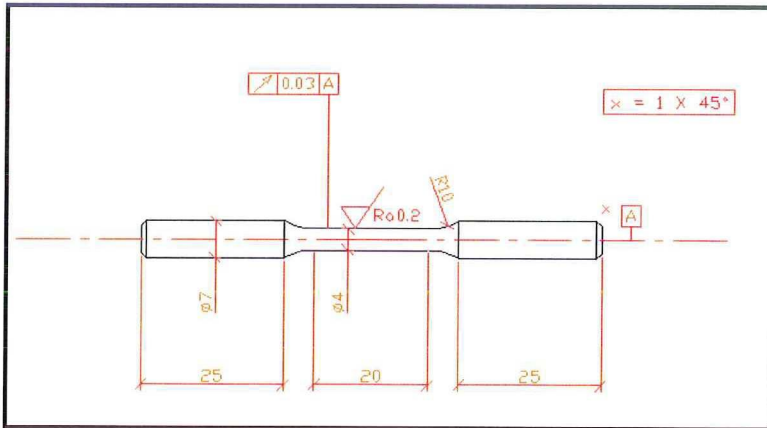


**Figure 2.7.** Schematic drawing of the tensile specimen.

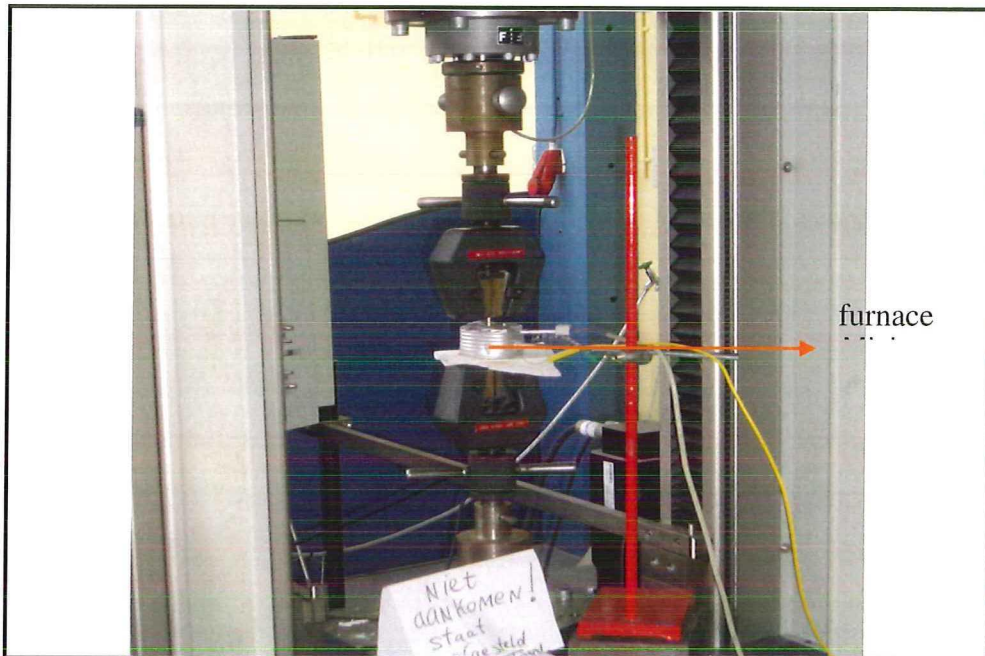


**Figure 2.8.** Instron tensile tester 1190 series with a mini-oven mounted for heating during the elevated-temperature testing.

## 3. Chapter Three

### 3.1 Characteristics of the flakes

#### 3.1.1 Compositions

One of the structural parameters that can be used to indicate the concentrations of the elements in the material is the lattice constant. This parameter refers to a constant distance between unit cells in a crystal lattice. This is especially in the case of cubic crystal structures where all of the distances between the unit cells are equal in a pure state. In line with this equidistance character of cubic crystal lattice, previous reports showed that lattice constant could qualitatively be used to determine the compositions of elements in a polycrystalline material. The linear dependence of the lattice constant on the composition of this melt-spun alloy was used to determine the concentration (solid solubility)  $X_{XRD}$  of Fe in the Al lattice by the x-ray diffraction technique. This was applied to complement the wet chemical analysis. The results obtained in this material are similar to previous data reported by Jones [32] who summarised values from a large number of experimental data. Previous reports by other investigators on the dependence of the lattice parameter on Fe concentrations in Al-Fe-V and Al-Fe-V-Si alloys showed that no reasonable variation existed between them. As a result of these findings, the depressions of lattice parameter observed in this investigation were ascribed to the dissolution of iron (Fe) in aluminium matrix [26, 33]. The equation used for the linear dependence on the composition is as follows.

$$\chi_{XRD} = \frac{0.4050 - \alpha}{0.00072} \quad \text{Eq. 3.1}$$

where  $\chi$  is expressed in atomic percent (at. %), and  $\alpha$  in nanometre. The results obtained from the x-ray diffraction analysis and wet chemical techniques are summarized in Table 3.1. The wet chemical results show that the dissolved iron in the samples of flake  $A_2$  and flake  $A_3$ , in comparison with the dissolved iron in flake  $A_1$  (2003), decreased over the years by 1.25 wt.% in flake  $A_2$  (2004) and 3.8 wt.% in flake  $A_3$  (2005). See Table 3.1. However, the general compositions still represented supersaturation of the elements in the matrix. Rivlin *et al* [34] reported that the

solubility of iron depended on the crystal structure and casting temperature. However, they agreed with Roberts *et al* that 1.8 wt.% was the equilibrium solubility of iron in aluminium [35]. Gephardt and his co-workers also affirmed previous reports on the vanadium solubility and showed that the equilibrium solubility of vanadium in liquid aluminium was 0.91 at.% at 1008 K [36].

A major contrast was noted in the lattice parameters correlated with the dissolved Fe in the HIP and extruded samples. The x-ray diffraction results showed that the lattice parameter expanded, suggesting that the solubility limit of Fe was also extended. See Table 3.1 These contrasting observations could be linked to the increased dissolution of V and its phase in the Al matrix due to the high temperatures of HIP and extrusion. Previous reports showed that vanadium apart from acting as a grain refiner for aluminium alloys could increase the lattice constant in an aluminium matrix, even though its atomic radius (1.35 Å) is lower than iron (1.40 Å) [27].

**Table 3.1.** Composition determined by wet chemical analysis test (approx. inst. error of  $\pm 0.05\%$  for the XRD)

Sample	Al[m%]	Fe[m%]	V[m%]	Si[m%]	Fe[at%] $X_{XRD}$
$A_1$	86.41	8.77	1.27	0.31	8.75
$A_2$	87.71	8.66	1.28	0.51	8.74
$A_3$	89.08	8.43	1.35	1.08	8.17
HIP sample from $A_3$	84.23	8.44	1.36	1.57	8.38
Extruded billet from $A_3$	86.45	9.08	1.33	1.40	8.38

Concentrations in [mass %], HIP sample  $\rightarrow$  compacted

### 3.1.2 The as-melt-spun microstructure

Figs. 3.1 to 3.3(b) show the typical microstructures of the ribbons in the as-melt spun state, which were obtained from the materials under varying rapid solidification conditions. These microstructures were clearly different as opposed to the supposed using of similar alloying ingredients and melt-spinning conditions. In general, the microstructures of melt-spun ribbons can be categorized into two zones: Zone A (the wheel side) (Fig. 3.1), and B (the free side) according to the classification of Jones

[37]. Several reports affirmed that the microstructure of ribbons produced by the melt-spinning technique showed varying microstructures that were correlated to the processing conditions. The wheel side and the other side freely exposed to air had remarkable differences in their structural features and properties. The details of the as-melt-spun microstructures of Zone A and Zone B in the flakes are shown in the optical micrographs (Figs. 3.1 to 3.3b). These micrographs correspond to flakes,  $A_1$ ,  $A_2$  and  $A_3$  (the batch produced in 2003, 2004 and 2005, respectively). Zone A microstructure in general and for this alloy in particular consists of nearly structureless particles in the Al matrix and the morphologies may be described as featureless. Zone B microstructures are those that are solidified near the air side of the ribbons, with particles ranging between 0.1-1  $\mu\text{m}$  in diameter. The microstructures are coarser and less global in comparison to Zone A, implying less fast solidification that occurs as the ribbon moves away from the wheel region. These two scales of microstructures as observed in these flakes are typical of any as-melt-spun microstructures [2].

Detailed optical microstructure study was conducted to characterise the nature of the microstructures and the phases in the flakes. Fig. 4.1 (flake  $A_1$ ) showed the presence of these two zones. Zone A was mostly a featureless structure. Zone B was less fine and could be described as globular, covering more than 60% of the area observed when the ribbon was edge mounted on its cross section. This zone was sandwiched by many uniformly dispersed fine particles measuring ( $\leq 0.2\mu\text{m}$ ) in between. The shape of these particles could be described as relatively spherical fine dispersoids. This microstructural feature can be regarded as an indication of the expected faster cooling rate as it depicts the level of dissolution beyond the solubility in equilibrium. An estimate of grain size could not be done, because of the limited magnification of the instrument. However, they seemed to be of many magnitudes finer than the conventional aluminum alloys (about 100  $\mu\text{m}$ ).

In the microstructure of flake  $A_2$  presented in Fig. 3.2a, Zone B was mostly dominant in the flake, which consisted of equiaxed dendrites and grains predominantly. The equiaxed grains in this particular case denoted dendrite growth in several space directions according to Steinbach, *et al.* [38]. Zone B covered more than 90% of the

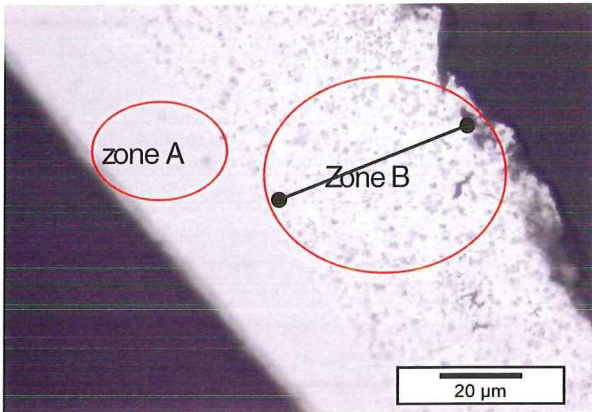
area observed when the ribbon was edge mounted and extended all the way across the flake. The dendrite arm spacing in this flake were in the ranges of 2.0 - 3.1  $\mu\text{m}$  in size. Fig. 3.2b shows a magnified image of the Zone B microstructure of the flake.

Steinbach and his co-workers reported that equiaxed dendrites were formed due to the interactions of the thermal fields with local nuclei density during solidification. The thermal fields from neighboring dendrites would overlap as the dendrites grew towards each other, while the tip velocities would decrease with time until the supercooling was completely dissipated and any tip growth stopped. Further solidification occurred through the thickening of the dendrite arms. The dynamics of such equiaxed solidification was strongly dependent on the distance between the grains or, in other words, the local nuclei density. For large distances, the thermal fields would not significantly overlap until late in the solidification process and the dendrites could grow relatively undisturbed for at least some time. Then, large dendritic structures could be observed in the as-solidified microstructure. For smaller distances, however, as in grain refined castings or rapid cooling, the thermal interactions could be so strong from the beginning that the grains could retain a globular shape and dendritic growth would not take place [38].

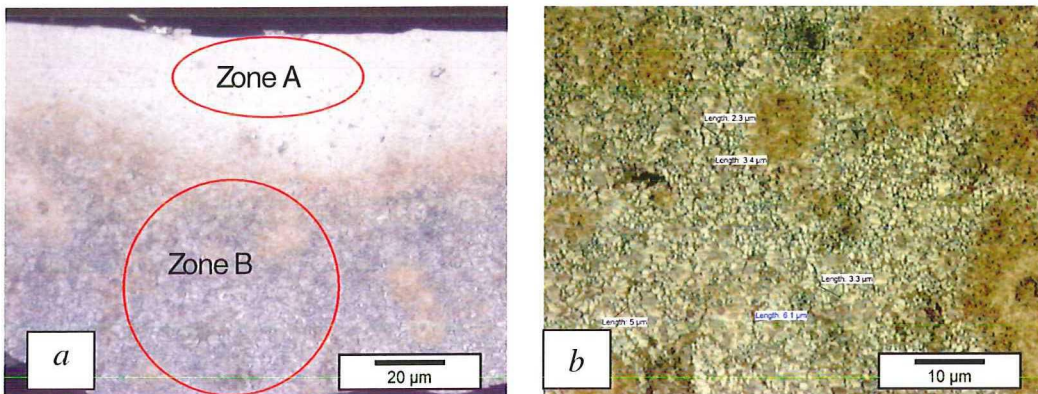
Previous investigation by Bhadeshia also showed that the dendritic condition could arise when a small perturbation at the interface ended up in even more supercooled liquid so the interface became unstable in several directions. This type of dendrite growth was a frequently observed growth mode in some conventional aluminium casting and in the welding process where cooling rate was less rapid [39].

Fig. 3.3a shows the optical micrographs of flake  $A_3$ . The microstructure also consisted of mainly Zone B. The microstructure showed that the dendrite arm spacing and morphologies were larger than those observed in flake  $A_2$ . Other significant features observed in the flake included (i) very little Zone A microstructures and (ii) several equiaxed dendrites commonly observed in the Zone B microstructure with a range between 3.0 - 3.5  $\mu\text{m}$ . Fig. 3.3b shows a magnified image of the zone B microstructure of flake  $A_3$ . In line with the similar reports, the presence of the dendrites in these microstructures was an indication of a lower solidification rate

applied during the melt-spinning operation. In general, the present study contrary to the popular views and reports shows that the coarser microstructure (Zone B) can also be formed almost on the wheel side. The results show that the thickness in each of the zones depends on the melt-spinning conditions. A low cooling rate can lead to outrightly Zone B in the microstructure of the flake and vice versa.



**Figure 3.1.** Optical micrograph of etched flake  $A_1$  showing the presence of Zone A and Zone B surrounded by relatively spherical dispersoids.



**Figure 3.2.** (a) Optical micrograph of etched flake  $A_2$  showing a limited area of Zone A as well as the dendrite structures existing within Zone B and (b) a high magnification micrograph of Zone B.

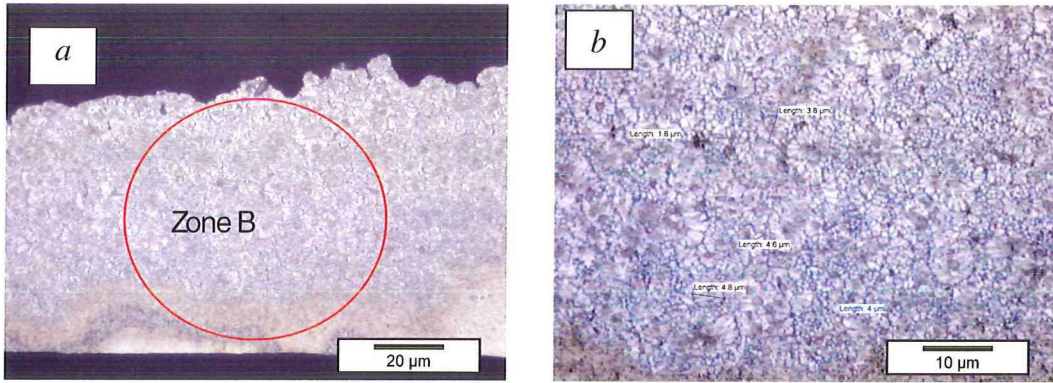


**Figure 3.3.** (a) Optical micrograph of etched  $A_3$  (batch 2005) showing a limited Zone A structure as well as equiaxed dendrite structures within Zone B and (b) a high magnification micrograph of Zone B

### 3.1.3 Correlation between the microstructure / flake thickness with cooling rate

It has been well established that in melt spinning the local cooling velocity decreases as the distance from the heat sink increases except for the chilling surface. Previous results in melt spinning showed that low cooling velocity could occur as a result of low cooling rate and an increasing heat conduction distance between solidifying melt and heat sink [40]. This is so because during melt spinning the cooling conditions are near Newtonian and thus the ribbon temperature decreases exponentially with time [41].

$$T - T_w = (T_i - T_w) \exp\left(-ht/X\rho c\right) \quad \text{Eq. 3.2}$$

where  $T_w$  is the wheel temperature,  $T_i$  the initial melt temperature of 278 and 1223K, respectively,  $h$  the heat transfer coefficient ( $6 \times 10^5 \text{ W/m}^2\text{K}$ ) at the ribbon-wheel interface,  $X$  the ribbon thickness,  $\rho$  the melt density ( $2.92 \text{ g/m}^3$ ), and  $c$  the specific heat for the flake  $C_p = 100 \text{ Jk}^{-1}\text{K}^{-1}$ . Over a small solidification temperature range, the equation is approximately linear and thus the mean cooling rate  $\frac{dT}{dt}$  may be given by [40, 41]:

$$\frac{dT}{dt} = h(T_i - T_w)X\rho c \quad \text{Eq. 3.3}$$

It was also reported that for a given rapid-quenching technique the thickness of the specimen obtained is indicative of the average cooling rate, provided that the experimental conditions are reasonably constant. The thinner the specimen, the higher the cooling rate and hence the larger the concentrations of some elements (Fe, Si) in the solid solution [9]. See Fig. 2.10. For splat-cooled aluminium, the lattice parameter was reported to decrease with decreasing specimen thickness, an effect that was initially attributed to the presence of quenched-in excess vacancies by Kirin *et al* [43]. More recent reports however ascribed this to cooling rate and the supersaturation of elements in the matrix of the material. A direct correlation for the cooling rate was also made from the ribbon thicknesses as given by Bowel *et al* [42]:

$$\lambda \approx \beta \varepsilon^{-n}$$

Eq. 3.4

where  $\lambda$  = spacing/cell arm space size,  $\varepsilon$  = cooling rate (K/s);  $\beta = 50\mu\text{m} (\text{Ks}^{-1})^{1/3}$ , and the constant  $n = 0.3$ . The values obtained from these calculations are approximately  $\approx 2.2 \times 10^5 \text{ K/sec}$  and  $2.15 \times 10^5 \text{ K/sec}$  for flakes  $A_2$  and  $A_3$ , respectively. The cooling rates based on Equations 3.3 and 3.4 were in close agreement with the predictions by other authors for this type of flakes. However, Equation 3.4 could not be used in calculating the cooling rate in flake  $A_1$ , because no dendrite structure was observed in the microstructure by the optical microscope. It implies that a higher cooling rate was employed during the melt spinning of flake  $A_1$  than other flakes. This is in common with the observed microstructures and composition analysis.

Also, the measurements of the distributions and sizes of dispersoids in flake  $A_1$  revealed that it had a narrower range than the other flakes, between  $0.1 - 0.2\mu\text{m}$ . As expected, flakes  $A_2$  and  $A_3$  had broader variations in the aspect ratio and size of dispersoids. Their sizes range between  $0.1 - 1.5\mu\text{m}$ . This was ascribed to the solidification phenomena during the melt-spinning processing of the ribbons. The trend found in the results is consistent with that reported in other works in the case that higher cooling rate is essential for reducing the time necessary for solidification

and suppressing growing dendrites. This eventually results in a dispersion of finer particles and microstructure materials. See Fig 3.1.

**Table 3.2.** Ribbon thickness and calculated cooling rate of the flakes

Samples	Thickness	Cooling rate (Ksec <sup>-1</sup> )
A <sub>1</sub> [the batch of 2003]	56.41 μm	5.2x10 <sup>6</sup>
A <sub>2</sub> [the batch of 2004]	87.71 μm	2.28x10 <sup>5</sup>
A <sub>3</sub> [the batch of 2005]	89.08 μm	2.14x10 <sup>5</sup>

### 3.1.4 X-ray diffraction results

X-ray diffraction patterns from the three batches of flakes, the compacted block and the as-received extruded rod (coded C<sub>3</sub>) are presented in Fig. 3.4. The comparison between the diffraction lines of the wheel side and those of the free surface from flake A<sub>3</sub> are shown in Fig. 3.5. From Fig. 3.4, it was found that the overall appearance of the diffraction intensities of the Al matrix in this alloy were ‘random’ like in relation to the pure aluminium diffraction lines. The diffraction peaks of the α-Al phase occurred randomly within 2θ; most of them were shifted to larger 2θ values. This suggested that the matrix was saturated with the alloy elements as expected, after melt spinning [44].

Also the intensities of the aluminum peaks decreased dramatically with respect to the α-Al diffraction lines of the same alloy processed by the conventional casting. This meant that the sizes of particles in this material were smaller or more refined due to melt spinning. The most reduced peak occurred to flake A<sub>1</sub>. The reductions of the aluminium intensities from A<sub>3</sub> seemed to be the least. On the other hand, the decrease of diffraction peaks can be attributed to thermal vibrations resulting from the rapid quenching of the elements in the aluminium matrix during melt spinning. Thermal agitation decreases the intensity of diffracted lines because it has the effect of smearing out the lattice planes; in such a situation atoms can be regarded as lying no longer on mathematical planes but rather in platelike regions of ill-defined thickness. Thus, the scattering of the diffracted beams at the Bragg angle by various parallel planes will not be as perfect as it is for a crystal with fixed atoms [45].

It was also observed that the diffraction lines for the extra phase(s) in all the samples were similar. This implies that the compositions of extra phase(s) within the samples differed insignificantly. A good match from the extra phases with data in the PDF (Powder Diffraction File) was made and the relative amounts of phases represented by major and minor traces were determined by comparing the peak heights, which showed all the flakes contained similar types of phases. The phases included:  $\alpha Al$ ,  $Al_{11}V$ ,  $FeAl_2$ ,  $AlFe_3$ . Surprisingly, these are all the equilibrium phases. The presence of these equilibrium phases in the ribbons after repeated tests was confirmed, which was inconsistent with the previous reports that showed that metastable phases were likely to occur in a melt-spun flake, because of rapid cooling. This result apart from the instrument sensitivity or resolution of elements / intermetallic phases in the samples has been ascribed to the low cooling rate applied during the melt spinning of the flakes.

Fig. 3.5 shows the diffraction pattern determined from the free surface and the chill surface of flake  $A_3$  (batch 2005). The results showed that the two zones have similar diffraction lines. This meant that the compositions within the two zones were similar and could have the same amounts and types of phases. Again, these results are not in common with other reports. Previous report by Bendijk *et al* [9] showed that there was no solute rejection on the wheel side as against the free side of the ribbon. Their analysis with the aid of lattice parameter and microhardness on the ribbons gave good indications of higher strength on the wheel side than the free side, indicating higher solubilities of the elements in the alloy on the wheel side. The limited amount of chilled surface area (Zone A) in this flake ( $A_3$ ) can be the reason for the abnormality.

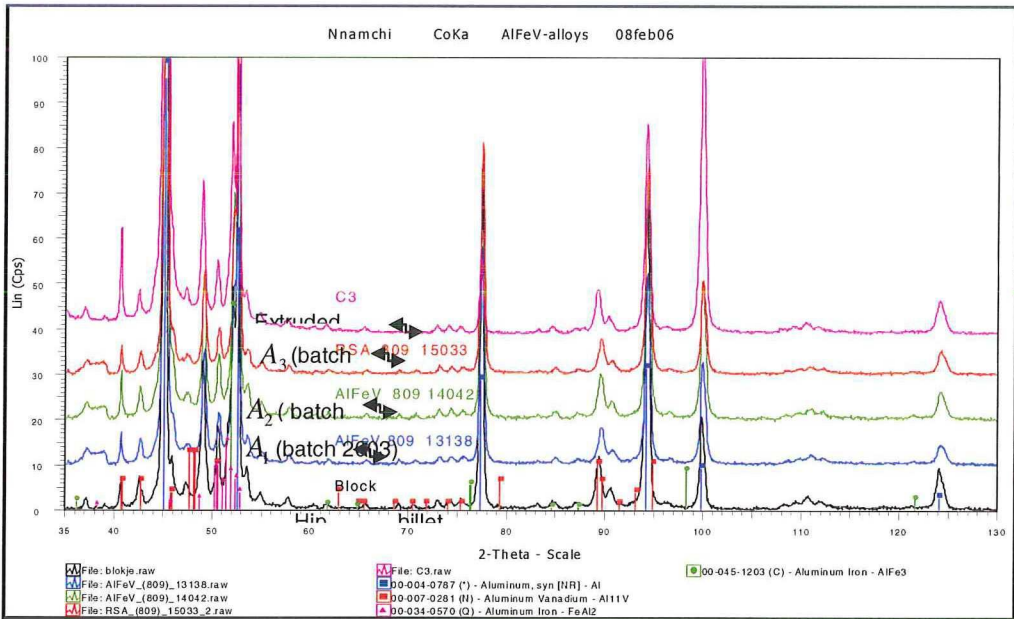


Figure 3.4. Diffraction from the flakes, ( $A_1$ ,  $A_2$  and  $A_3$ ) the compacted billet (block) and the extruded rod (C3).

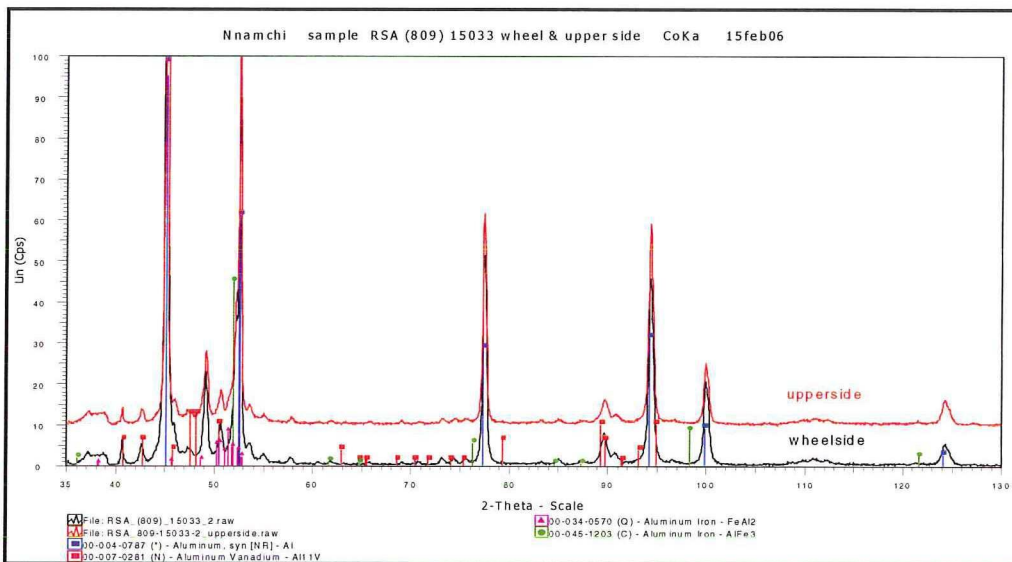


Figure 3.5. Comparison of the diffraction lines of the wheel side with the free side of flake  $A_3$ .

### 3.1.5 Lattice parameter

It has been established that the changes in the lattice parameter of a melt-spun alloy are related to micro residual strains and gradients in composition. This is because micro-strains are produced by a distribution of both tensile and compressive forces and the resulting diffraction profiles are broadened about the original position. Both crystal size and strain effects generally produce a symmetric broadening in diffraction lines of materials. The observed broadening of diffraction lines in the samples

especially at large  $2\theta$  values apart from instrument effects are therefore related to the gradients in composition and residual strains [46].

All these can be deduced from the analysis of the lattice parameters of the flakes and the as-received extruded sample. The lattice parameters of the three flakes, compacted billet and those of the extruded rods are listed in Table 3.4. The results showed that considerable line broadening occurred within the samples; most occurred to the sample  $A_1$  (batch 2003). This is because flake  $A_1$  has the largest concentration of dissolved iron than the other flakes. See Table 3.4. The broadening from  $A_3$  seems to be the least, which has the least concentration of dissolved iron. Previous investigation by J. Mittemeijer *et al* [46] showed that the variations in dissolved iron within the diffracting domains of the aluminum-rich phase and differences in the average concentrations of silicon and vanadium in solid solution between the domains (noting that the fraction of elements dissolved depends on the ribbon thickness (Fig. 2f)), could have contributed to this line broadening, thus leading to apparent strain values [46].

It was also observed that flake  $A_1$  has the strongest diffraction line, being in line with a higher concentration of dissolved iron and a cooling rate observed from previous results in this flake. This was attributed to a build-up of strains within the flakes due to the supersaturation of the iron element due to melt spinning. [47]

The lattice parameter changes of the  $\alpha$ -Al phase in the flakes with respect to the perfect crystal lattice were also examined by quantitative measurements using XRD as shown in Table 3.4. From the results, it can be concluded that the decrease in lattice parameter in all the melt-spun flakes is a confirmation to the supersaturation in the aluminum matrix. Going from sample  $A_1$  (batch 2003) to  $A_3$  (batch 2005), the lattice parameter changes are less, being also in common with the previous results of composition analysis and cooling rate. Bendijk [9] *et al* in their report attributed the decreases in lattice parameter from 4.0494 Å for aluminium to 4.039 Å and 4.043 Å on the wheel side and free side, respectively, to the supersaturation of silicon in the aluminium matrix.

The observed increases of the lattice parameter in the as-received HIPed billet and extruded rod will be explained later by the precipitation of silicon crystals and iron-containing intermetallic phases during the hot isostatic pressing (HIP) and extrusions operations.

**Table 3.3.** Lattice Parameters for the materials.

$CoK_{\alpha}$									
<b>Al DF -&gt; 04-0787:a[A]</b>	<b>4.0494</b>								
Materials Al {400}	Lat. para. Angstrom	OBS Max 2-Theta°	$d$ (Obs. Max) Angstrom	Max. Int. Cps	Net Height Cps	FWHM 2-Theta	I. Breadth 2-Theta	Gr 2.T	
$A_1$ (batch 2003)	4.0463	124.280	1.0118	3.620	3.480	0.706	0.728	124	
$A_2$ (batch 2004)	4.0468	124.292	1.0117	4.950	4.800	0.656	0.696	124	
$A_3$ (batch 2005)	4.0470	124.174	1.0116	4.290	4.100	0.616	0.693	124	
<b>Billet HIPed at 375 °C</b>	4.0490	124.319	1.0123	7.660	7.520	0.564	0.658	124	
<b>Rod extruded at 450 °C</b>	4.0490	124.175	1.0122	5.600	5.520	0.724	0.835	124	

**Table 3.4.** Lattice Parameters for the materials continued.

Materials Al {400}	$d$ (Gravity C.) Angstrom	Net area Cps x 2-Theta°
$A_1$ (batch 2003)	1.0115	2.534
$A_2$ (batch 2004)	1.0119	3.326
$A_3$ (batch 2005)	1.0116	2.852
Billet HIPed at 425 °C	1.0123	4.950
Rod extruded rod at 450 °C	1.0125	4.610

### 3.1.6 Thermal analyses

The DSC traces of these flakes obtained during continuous heating at a rate of 20 °C/min for the three batches of flakes as well as the as-received extruded rod processed from flake  $A_3$  are presented in Figs. 3.6 to 3.9. From these figures, an increase in heat flow represents an exothermic reaction (a re-solidification peak), while a decrease in heat flow is used to represent an endothermic reaction (a re-melting peak). The traces showed a two-stage structural change that took place in the samples – decomposition and melting (exothermic and endothermic peaks) until 600

°C. The traces of flakes  $A_1$  and  $A_2$  consisted of two endothermic peaks, first in the range of 649.5 - 680.5 °C, while the second peak is in the range of 730 - 800.8 °C. The second peak in flakes  $A_1$  and  $A_2$  at 730.2 °C is small in size, but the broadest of them is in flake  $A_1$ .

Previous investigation by Dunlap *et al* [48] on the rapid quenching of the Al-Fe alloy system using melt spinning at a cooling rate of  $2 \times 10^6$  K/s affirmed the presence of the Al-Fe metastable phase  $Al_{0.86}Fe_{0.14}$  having a non-Bravais structure at 597 °C. It was reported that this phase transformed to  $Al_6Fe$  on further heating up to 657 °C. ( $Al_6Fe$  then transformed to  $FeAl_2$  and/or  $AlFe_3 + \alpha Al$ .) The transformation of  $FeAl_6 \rightarrow FeAl_2$  and/or  $AlFe_3 + \alpha Al$  was a diffusion-dependent process, which could have occurred easily by continuous heating/cooling at a rate of 20 °C/min as applied during the DSC analysis.

The DSC trace of flake  $A_3$  is presented in Fig. 3.8. The flake had different thermal reactions; one melting peak with an onset melting temperature in the range of 640 - 680 °C and a slight doublet re-solidification peak in the range of 600 - 612 °C. (The word doublet is in common with the description given by Allen *et al.* [49].) It was also found that all the flakes were solidified in a similar doublet peak manner and almost at the same temperature range between 612 - 617 °C, apparently showing that similar mechanism might be responsible for the re-solidification of the flakes.

Comparing the three traces in Figs. 3.6 to 3.8 with the trace of the extruded sample processed from flake  $A_3$ , the second endothermic peak which was not present in the trace of flake  $A_3$  was seen in the trace of the as-received extruded rod processed from the same flake  $A_3$ . However, the DSC cycle exhibited by the as-received extruded rod processed from flake  $A_3$  presented in Fig. 3.9 has almost the same type of thermal cycle with flakes  $A_1$  and  $A_2$ ; two melting peaks, the first is in the range of 650 - 670 °C and the second between 710 - 800 °C. The solidification peak is also broad between 580 - 599.9 °C. The activation energy  $Q$  for full decomposition in the flakes is 2.4890.27eV as calculated by DSC. This value is in good agreement with the

reported activation energy of 1.9 - 2.7 eV in literatures. The high value of the activation energy was said to be because of the low volume diffusion of Fe in aluminum [48]. This indicates that the transformation mechanism is controlled by coarsening and not by transformation sequence [40].

Based on the temperature ranges in combination with the peak features, the first endothermic peaks (649.5 - 680.5°C) that appeared in all the traces may be easily identified as the melting of the binary phase ( $FeAl_2$ ) in a ternary Al-Fe-Si eutectic and the primary aluminum dendrites, respectively. The second peaks found in flakes  $A_1$ ,  $A_2$  and the melting of the primary aluminum were the results of peak split of the binary Al-Fe and Al-V eutectic melting, which reflected a different melting sequence of Al-Fe-V-Si in the matrix of the ribbons. Based on a gap between the nucleation temperatures of iron and silicon at grain boundaries and in the interior of grains during thermal reactions, C.R. Ho [52] reported that iron or silicon first nucleated along the grain boundaries and cooling rate played a dominant role in determining the size of the temperature gap. The precipitation of these particles during extrusion could account for the appearance of this melting peak in the extruded sample processed from flake  $A_3$ , which was not in the trace of flake  $A_3$ .

In the same vein, Surikov *et al* [53], while working on an Al-V alloy affirmed that an ordered phase occurred at the stoichiometry of rapidly quenched of Al-V after annealing at 400 °C for 90 h. This phase was identified as  $Al_{11}V$ . Their DSC result proved that there was also a split temperature gap during the quaternary Al-Fe-V-Si eutectic melting for iron at the two different temperature ranges by the continuous heating process. The size and the broadness of the peaks were related to the variations in cooling rate during melt spinning and the resolution of the elements in the matrix. The phases were also the component phases identified by the x-ray diffraction analysis.

The traces and peaks found in the DSC analysis correspond to temperature range for the transformation of these phases ( $\alpha Al$ ,  $Al_{11}V$ ,  $FeAl_2$ ,  $AlFe_3$ ) reported earlier by the X-ray diffraction analysis.

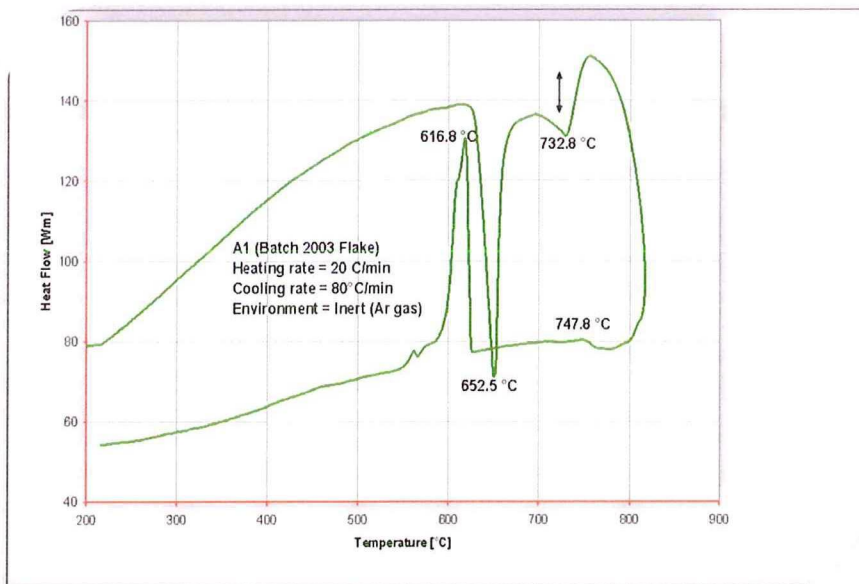


Figure 3.6. DSC curve representing the transformations in flakes  $A_1$ .

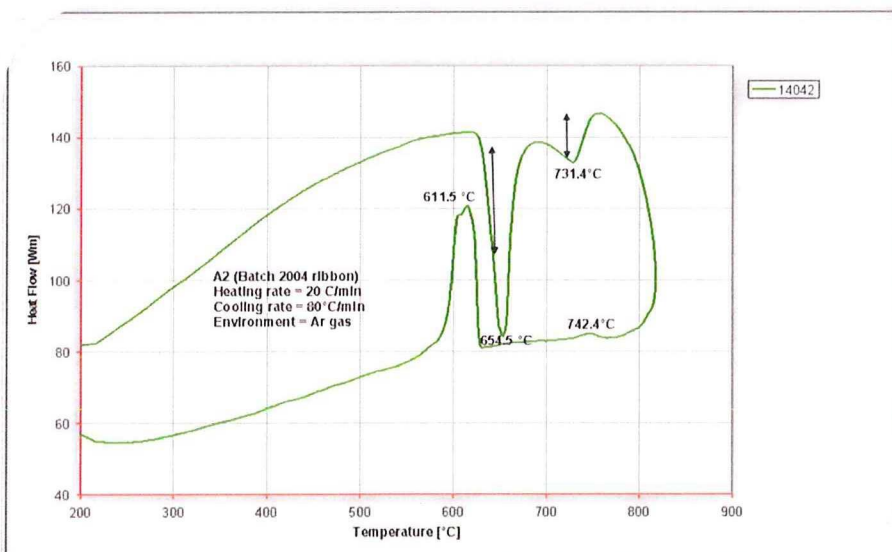
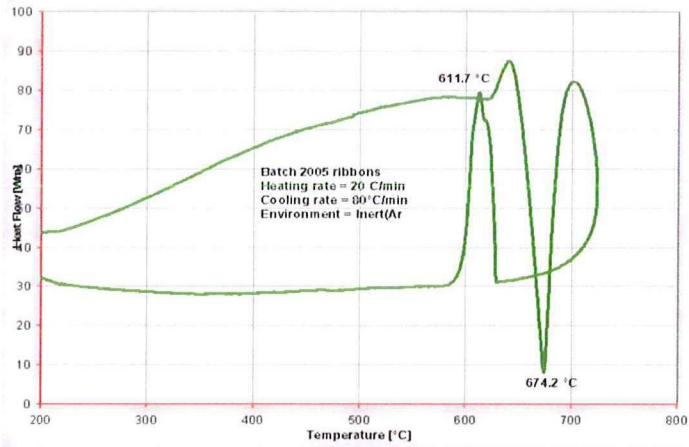
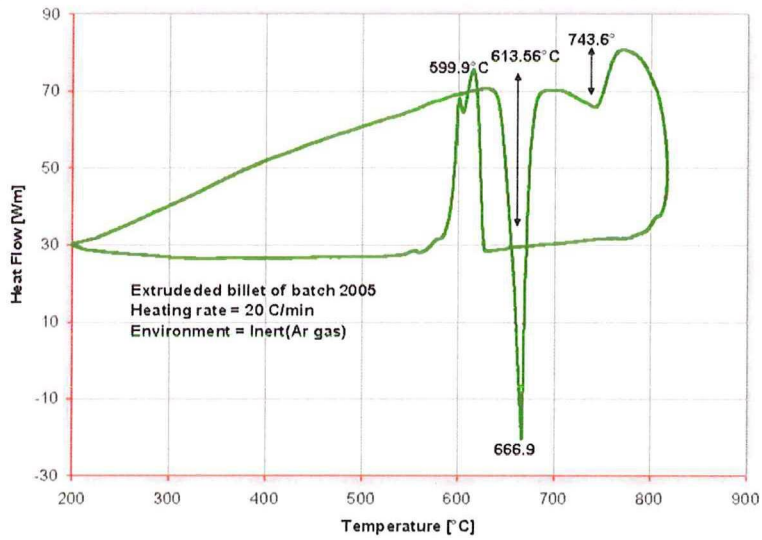


Figure 3.7. DSC curve representing the transformations in flakes  $A_2$



**Figure 3.8.** DSC curve representing the transformations in flakes  $A_3$ .



**Figure 3.9.** DSC curve representing the transformations in the as-received extruded rod produced from flakes  $A_3$ .

### 3.1.7 Influence of annealing temperatures on the microhardness of the flakes

The influences of annealing temperature on the microhardness of the flakes were evaluated as a measure of the mechanical strength between room temperature to 450 °C for 1 hour. This was done in a bid to determine the dispersion hardening response of the flakes to micro Vickers hardness. During the measurement, untypical low micro-hardness values were rejected on the assumption that sub-surface defects were responsible. Therefore, the measurements excluded the areas where normal melt-spinning defects, particularly porosity, were present.

The results in Figs. 3.10 and 3.11 show the distribution of microhardness measurement through the cross section of the flakes and the influence of temperature on the microhardness of annealed flakes  $A_3$ , respectively. It can be observed from Fig. 3.10 that the microhardness value around the areas of the wheel side described as Zone A and the areas around it are higher than in areas around Zone B. In common with this result, flake  $A_1$  (batch 2003) which had a high percentage of Zone A possessed the highest microhardness values. This demonstrates that the hardness of the AA8009 alloy may be enhanced when more iron is dissolved in the aluminium matrix, instead of existing as a free phase. Bendijk *et al* carried out an electron probe analysis of the wheel side and the free side of a melt-spun ribbon [9]. They found out that there was no solute rejection on the wheel side as against the free side of the ribbon. Their analysis with the aid of lattice parameter and microhardness on the ribbons gave good indications of higher strength on the wheel side than the free side, indicating higher solubilities of the elements in the alloy on the wheel side. The decreases in lattice parameter from 4.0494 Å for aluminium to 4.039 Å and 4.043 Å on the wheel side and free side, respectively, were attributed to the supersaturation of silicon in the aluminium matrix. The results agree with those of Tewfik [54]. This trend is also consistent with the results obtained by Jones [37] and affirmed by others [55]. The high hardness was attributed to the effect of the solute atoms on the aluminium lattice and the interactions of different atomic species in the ribbon matrix.

Fig. 3.11 shows that effect of exposing the flakes to certain temperatures. An exposure to temperature at above 350 °C resulted in low microhardness in the flakes. This result can be an indication about what effect of an increase in temperature will be on the microstructure and mechanical properties of the sample. This could have happened due to the particle coarsening occurring at temperatures above 350 °C. The higher microhardness of the alloy AA8009 was due to these iron-containing phases and silicon crystals, where the thermal activation energy was enough to nucleate these intermediate phases which were coherent with the matrix, leading to a sharp rise in microhardness up to 370 °C when thermal exposure was carried out for 1 hr. This temperature can be termed as the upper limit for enhancing the mechanical property of the material.

This microhardness result may be extended to give an indication of the tensile strength of this RSP AA8009 aluminium alloy, since  $HV = 3\sigma_y$ , where  $\sigma_y$  and HV are the yield stress and Vickers microhardness, respectively. Experimentally, the microhardness values can be compared with the 0.2% strength of aluminium.

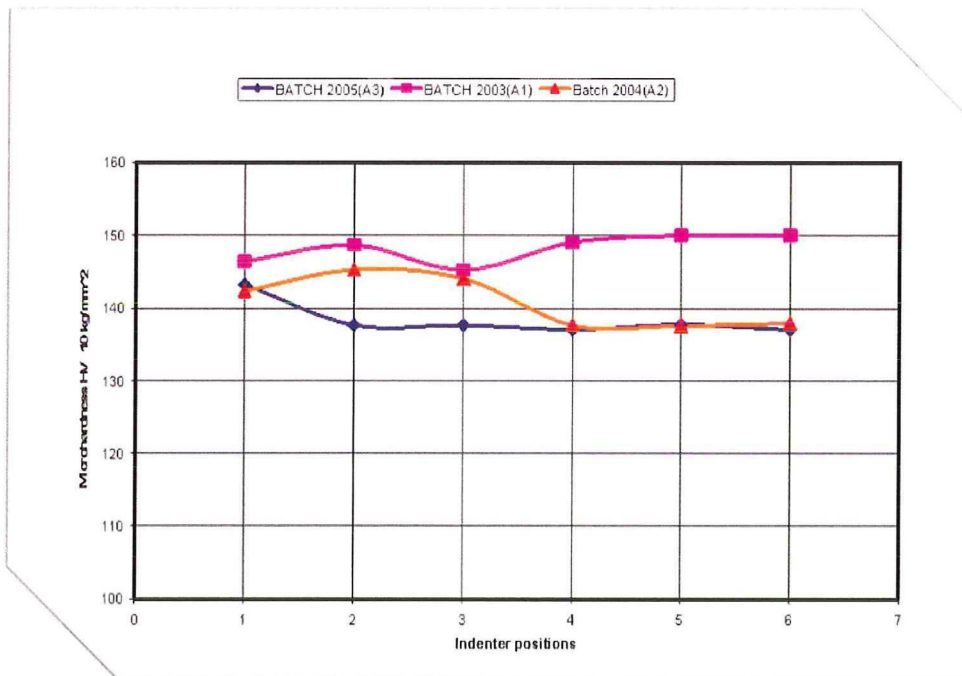
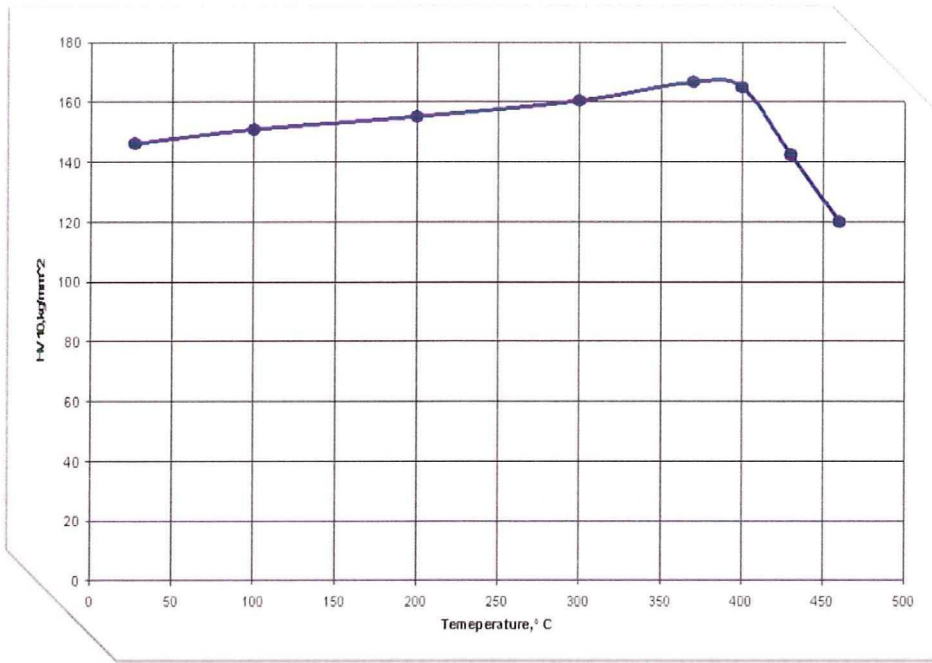


Figure 3.10. Cross sectional microhardness values of the flakes



**Figure 3.11.** Influence of temperature on the microhardness of annealed flakes A<sub>3</sub>.

## 4. Chapter Four

### 4.1 Processing optimization for enhanced elevated-temperature properties

#### 4.1.1 Extrusion characteristics

The investigation of the extrusion characteristics and the optimization of the elevated temperature mechanical properties were carried out using flake  $A_3$  (batch 2005), since the other batches were no longer in stock for these experiments. Fig. 4.1 shows the representative variation of extrusion pressure with ram displacement as exhibited by the initially compacted ribbons extruded at a reduction ratio of 10:1 and at different temperatures. It was observed that the alloy required high extrusion pressures. This showed clearly the material resistance to deformation. The high extrusion peak is true especially at a low extrusion temperature (370 °C) where the dissolution of silicon crystals and intermetallic particles during demisting at 150 °C and preheating at 400 °C prior to extrusion did not take place.

In addition, it was observed in the pressure versus ram displacement curves that the slope increased with rising temperature before the attainment of a peak value. This suggests that the work hardening rate increases with decreasing extrusion temperature. The pressure increase is consistent with the observation of the microstructures consisting of a high volume fraction of supersaturated dispersoids in other melt-spun ribbons [6]. The work-hardening was attributable to the Zener pinning on dislocations by dispersoids. This is evidenced in the as-extruded microstructure.

The comparison between the extrusion behaviour of the present alloy with that of a conventional 2000 series aluminium alloy showed an increased pressure requirement by the present alloy, indicating an increased resistance to deformation resulting from hard intermetallic particles incorporated in the microstructure as a result of melt spinning. These particles formed effective obstacles to dislocation motion throughout the deformation stages. The uniformity of the extrusion diagrams at the test temperatures showed that similar mechanisms were in operation during extrusion. See Fig. 4.1.

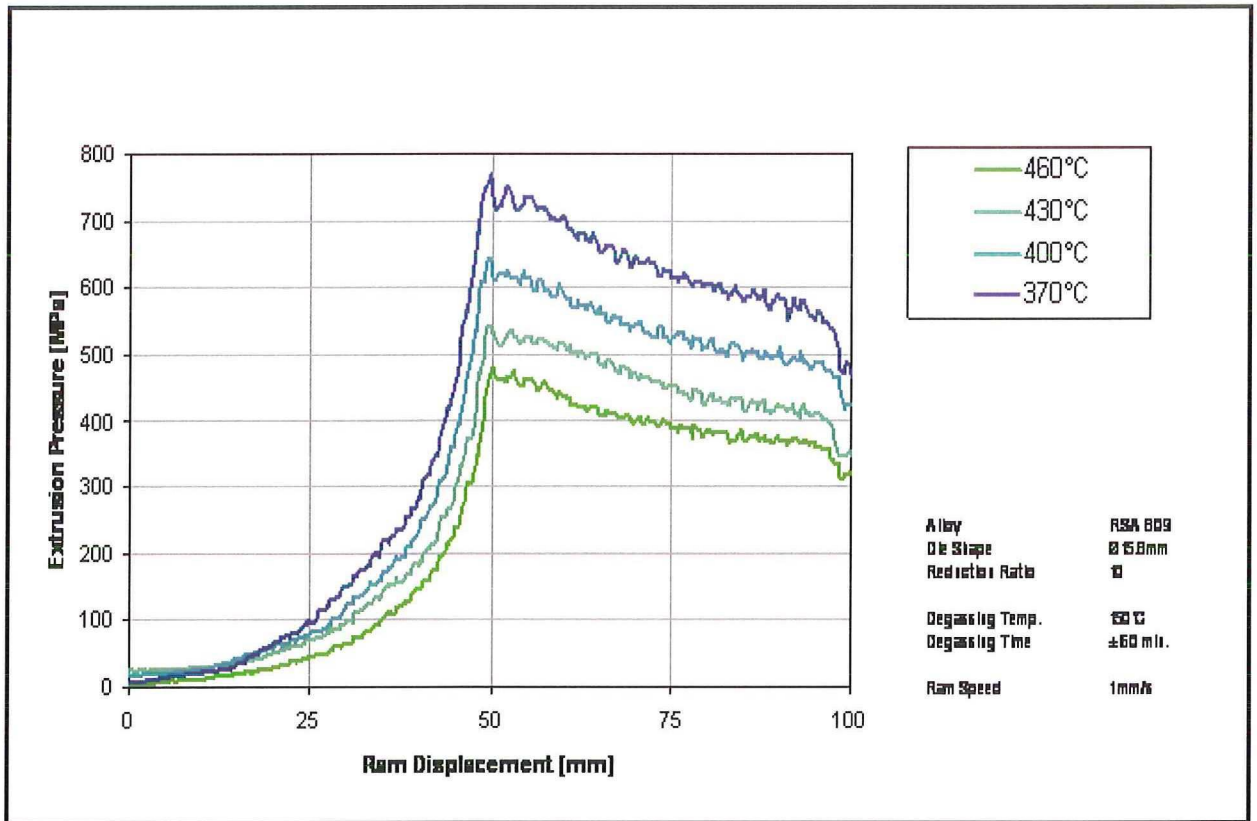


**Figure 4.1.** Representative variations of extrusion pressure with ram displacement and extrusion temperatures

Another important characteristics exhibited by the material during extrusion was the strong dependence of peak pressure on the extrusion temperature. During the experiment, the lower temperature limit reached was 370 °C and at this billet temperature the pressure required was 800 MPa, quite close to the pressure capacity of the press used. This temperature limit and the concern for surface defects were the main reasons why 370 and 460 °C were used as the temperature range for the alloy during the extrusion experiments. The results reported hereafter are restricted to this temperature range. In view of the strong dependence of work hardening of the material on temperature, the work reported below, focused on the structural evolutions during extrusion, takes extrusion temperature as the prime process variable, while reduction ratio and ram speed (strain rate) remain unchanged. A correlation between extrusion peak pressure and temperature was found to be of practical importance to this study, because the peak pressure is a breakthrough value in determining whether the execution of an extrusion cycle is possible [50]. See Fig. 4.2.

A linear slope was found from the correlation between extrusion peak pressure and the reciprocal of the absolute temperature for this material. The correlation showed that the peak pressure decreased steadily with rising temperatures without sudden changes between 370 and 430 °C. The linearity observed in this figure is in agreement with the rise in the microhardness value of the flakes at the same annealing temperatures. It thus suggests that the work hardening mechanisms operating in the material at these temperatures are similar. However, the appearance of a kink (non-uniformity) after 430 °C signaled the end of the correlation and an indication of a narrow usable extrusion temperature range of 370 – 430 °C for the material.

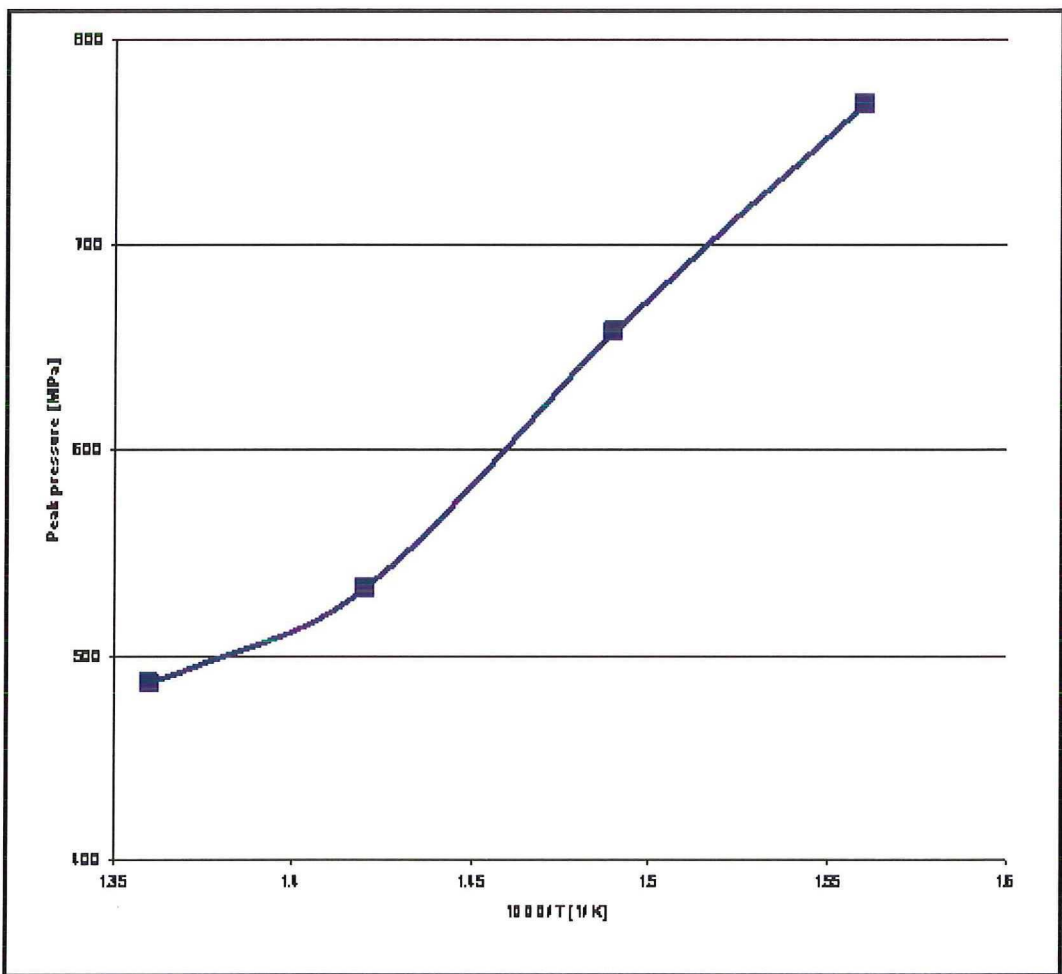


**Figure 4.2.** Plot of peak extrusion pressure against the reciprocal of the absolute extrusion temperature.

The observation of cracks in the internal structure of the samples extruded at 370 °C prompted the use of demisting to prevent cracking during the extrusion experiments. The cracks were initially thought to be due to strong work hardening

required in shearing silicon crystals dispersed in the material. The concern for this defect was high such that demoisturing of compacted billet prior to extrusion was considered important. These compacted billets were not degassed because the aluminum cans used for the compaction of the flakes did not have any provision for direct connection to argon or nitrogen gas before extrusion.

The billets were demoistured at 150 °C for varying times between 0 - 300 min prior to extrusion. This was to enable the determination of an optimum demoisturing time to enhance the mechanical strength of the material. Fig. 4.3 shows the representative variation of extrusion pressure and demoisturing time prior to extrusion as exhibited by the initially compacted ribbons.

It can be seen that the exhibited high extrusion peaks resulted from a moderate demoisturing time between 60 - 70 min. In contrast, the samples that were demoistured shorter or longer exhibited a characteristic similar to the non-demoistured ones. These characteristics borne by the material were ascribed to the onset of evolution and dissolution of iron-containing intermetallic particles and silicon crystals in the microstructure, in common with other works where aging time influenced the dissolution of silicon crystals into the matrix of aluminium alloys [43, 56].

A time limit between 60 and 70 min with an increase of  $\pm 10\%$  of the extrusion pressure was found to be the upper limit of demoisturing time in order to strike a balance between the dissolution of dispersoids and the increase of the volume fraction of the precipitated crystals in the material. Over 50 min eventually led to the high extrusion peaks noted in the samples. See Fig. 4.3.

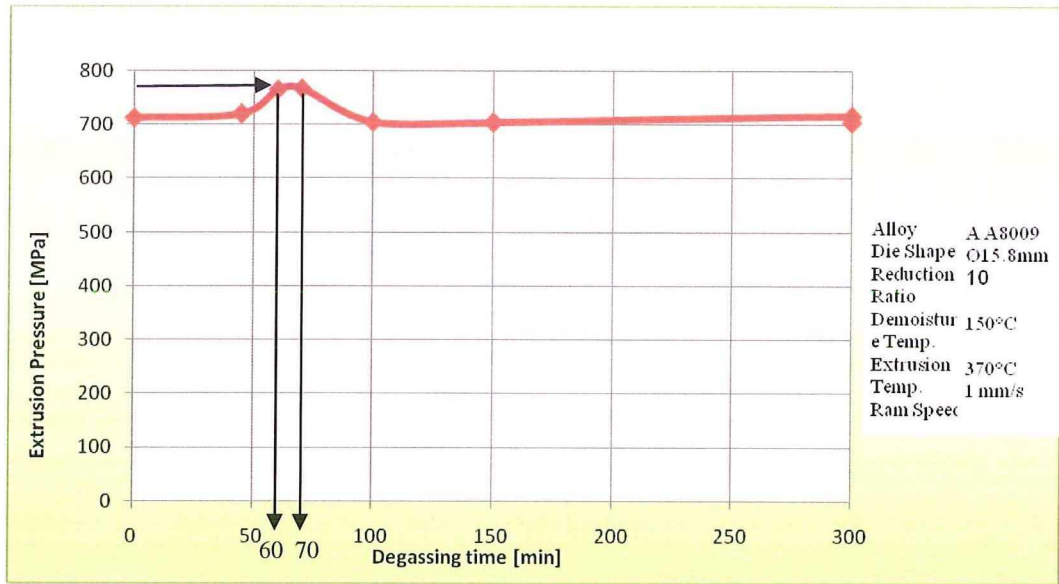


**Figure 4.3.** Plot of the maximum extrusion peaks against demoisturing time.

### 4.1.2 Precipitation and transformations

The results previously obtained from the x-ray diffraction analyses showed that the melt-spun flakes and the as-received extruded rod contained the same type of phases, which were identified as those already in the equilibrium state. Melt-spun aluminium alloys are traditionally related to the formation of non-equilibrium phases because of the rapid cooling rates involved. The non-equilibrium phases have a strong propensity to attain the equilibrium state by precipitating solutes from the supersaturated matrix during extrusion. In the investigation reported below, the effects of extrusion temperature varying between 370 – 460 °C and subsequent annealing treatment at 200 and 350 °C for 100 hr were used as the process parameters to study the structural evolutions in the material.

Fig. 4.4 shows an x-ray diffraction chart, summarizing the changes in diffraction patterns emitted from the reflection plane {400} of the matrices of the extruded material. The results show that the symmetry of the diffraction lines exhibited by the extruded matrix is similar to the ones obtained from the initial melt-spun flakes. However, the diffraction lines from the extruded matrices were still broadened, when compared with those from pure aluminium, indicating that part of the lattice distortions were still retained in the as-extruded matrix.

In addition, the breadths exhibited by the as-extruded matrix decreased progressively with rising extrusion temperature. This type of broadening is ascribed to stresses and strains resulting from heavy deformation at a low temperature (370 °C). However, the overall appearance of the diffraction lines from the extruded samples is the same in terms of the intensities of the Al-matrix diffractions and those of the additional phase(s). This means that the overall composition seemed to be the same, notwithstanding the variations in extrusion and annealing temperatures.

The diffraction lines of the Al-matrix reflections from all the samples are “random” like in comparison to the diffraction patterns of pure aluminium. It suggests that there was neither strong preferred orientation (crystallographic texture) nor any orientation differences in the samples due to the variations in extrusion or annealing temperatures.

The lattice parameters of the as-extruded matrices were calculated from the  $K_{\alpha_1}$  reflection after separation from the  $K_{\alpha_2}$  component. It showed an increase in the size of the lattice parameter as compared with the lattice size of the matrix in the melt-spun flakes, but the lattice parameter was still lower than the pure aluminium lattice size. The increase is apparently attributed to the precipitation of the supersaturated solutes: iron and silicon, both tending to decrease the lattice size of aluminium and being capable of overcoming the reverse effect given by vanadium. Vanadium has a lower solubility in aluminium than iron and silicon. The combined effect of iron and silicon will decrease the lattice constant of aluminium independently, while vanadium will do the reverse.

Another feature noted from the results was that the average lattice parameter of the aluminium matrix in the extruded material decreased from 0.40505 to 0.40481 nm over the extrusion temperature range from 460 to 370 °C. It is in common with the broadening noted earlier. Understandably, these lattice parameters were higher than the lattice parameter of the flakes that is 4.0470 nm.

Another feature of interest was the observed increase to 4.0499 nm in the value of lattice parameter of the as-received sample that was compacted using HIP at 425 °C prior to the extrusion at the same temperature. The implications of the results were that degassing has a similar influence to extrusion, to initiate the evolution of crystals and precipitation in the material. In principle, the improvement in mechanical properties by extrusion can be lost, if the compaction temperature is not checked.

The DSC analyses of the as-received rod extruded at 370 °C (Fig. 3.9) showed an additional high-temperature (734 °C) endothermic peak similar to the one seen on the flakes belonging to the batches of 2003 and 2004 (Figs. 4.6 and 4.7). Apparently, this was a sign indicating the resumption of transformation subsequent to extrusion.

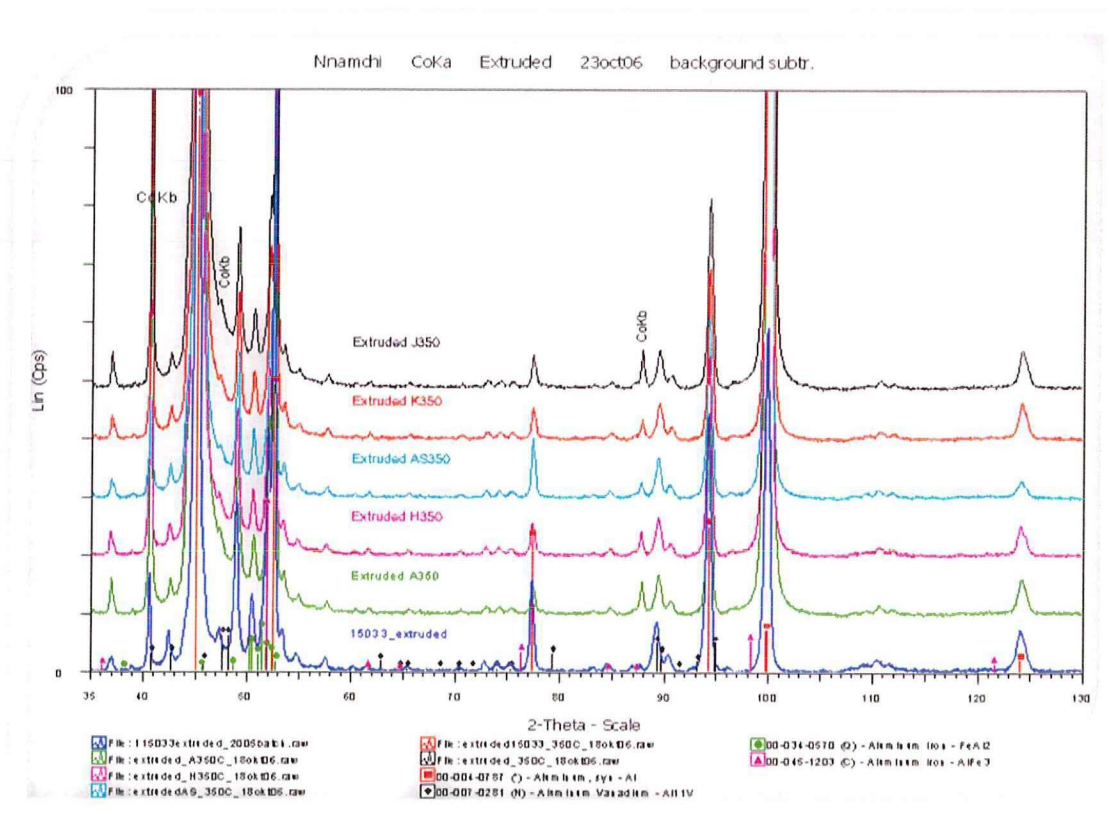


**Figure 4.4.** X-ray diffraction patterns showing the changes with extrusion temperature.

### 4.1.3 The as-extruded microstructure

Fig. 4.5 shows the optical microstructures of the material extruded at 370, 400, 430 and 460 °C and at a reduction ratio of 10:1. Apart from the earlier noted low extrusion

pressure peak, the microstructure of the rod extruded at the highest temperature (460 °C) was less aligned. It was found that the initial flakes were largely retained after the extrusion. Obviously, this is a common feature; if the applied pressure is not sufficiently high, the alignment of the flakes during extrusion will be limited. The presence of large coarse particles that are scarcely distributed in the microstructure was partly a manifestation of the degrading effect of high-temperature extrusion on the mechanical property of the material.

Apparently, the dissolution of the iron- and silicon-containing crystals into the matrix occurred with rising extrusion temperature. The coarsening and the formation of large particles of silicon crystals at a high extrusion temperature is primarily because silicon has a relatively high solid solubility and diffusion coefficient in aluminium. Moreover, extrusion provides easier paths for diffusion to proceed. The growth of the silicon crystals, therefore, becomes inevitable at high temperatures. Interestingly, the microstructures of the rods extruded at 400 and 430 °C did not show significant differences, nor produced any recognizable differences in the sizes of the silicon crystals and particles. The average sizes of the particles were measured to be between 0.1 - 1.5 µm. This means that the variation in the size of the crystals was due to the dependence in the size of the silicon crystals on extrusion temperature as observed by Skinner. This was apparent also in the microstructure of the billets compacted by hot isostatic pressing and the extruded rod [33].

The dependence of extrusion pressure on temperature, exhibited by the alloy, was the main factor that led to a decrease in extrusion pressure peak with rising temperature. Slight demarcations of the cross sections of the flakes can also be seen in the microstructures, but not as pronounced as in the samples extruded at 460 °C. As desired for the achievement of the mechanical properties of the alloy, a very high volume fraction of fine silicon crystals homogeneously distributed was observed in the microstructure. This is true for the microstructure of the rod extruded at 370 °C, as shown in Fig. 4.5. The shape of the particles can be described as spherical. A direct benefit gained from a low extrusion temperature is that the initial microstructure inhomogeneity and the cross sections of flakes observed at other extrusion temperatures were diminished. It was also noted that, under the extrusion condition (a

low temperature and a moderate demoisturing time of 70 min), extensive coarsening, as seen at higher temperature extrusion or fragmentation of silicon crystals, did not occur.

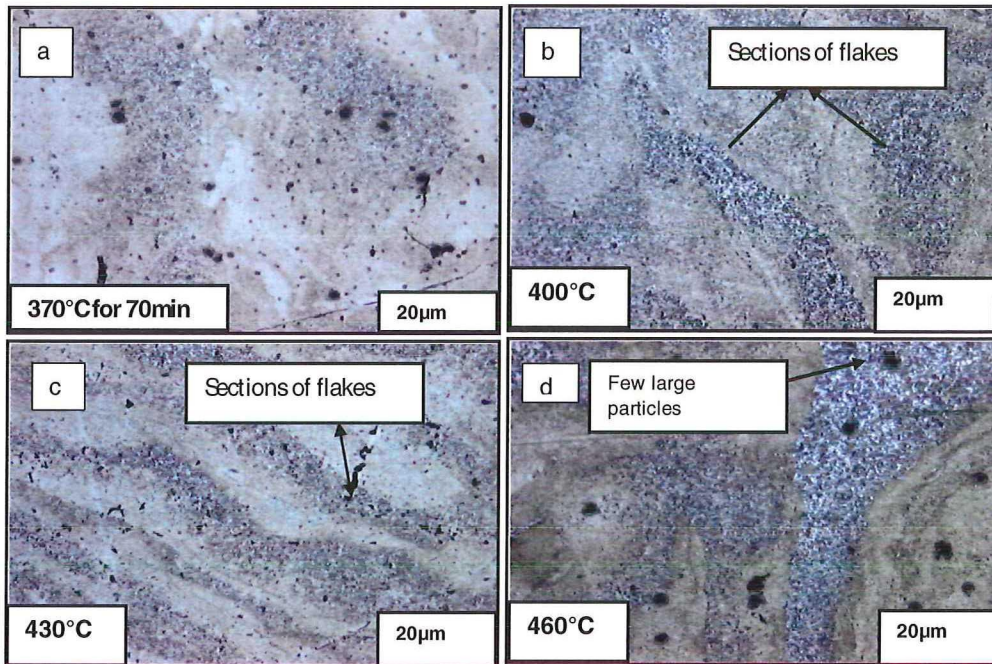


**Figure 4.5.** Representative microstructures of the material extruded at 370, 400, 430 and 460 °C.

Comparison between the microstructures of the demoistured samples and the non-demoistured sample was made. As noted earlier, demoisturing influenced significantly the strength of the material. This was particularly demonstrated with the samples extruded at 370 °C, which exhibited a high extrusion pressure peak. Fig. 4.6 shows the optical microstructures of the samples that were extruded at 370 °C. As evident from the figure for the samples (Fig. 4.6d) demoistured for 300 min, the inhomogeneous structures of the initial flakes, which characterised the samples extruded at higher temperatures, were evident. The reason is similar to that for high-temperature extrusion. The dispersed crystals were dissolved in the matrix due to a long demoisturing time. These dispersed particles were to act as effective obstacles to deformation. Obviously, this would lead to a low mechanical strength of the sample as

observed in the correlation curve between extrusion pressure and demoisturing time. See Fig. 4.3.

The microstructure of the sample demoistured for 70 min (Fig. 4.6b) showed that demoisturing of this material for about 70 min greatly improved the resistance of the alloy to deformation. Silicon and other intermetallic particles were sufficient to provide the required resistance to deformation by acting as effective obstacles to dislocation motion during extrusion. By this means, the strength of the extrudate was increased significantly. Cracks and deformation defects were observed in the samples that were extruded at this temperature without demoisturing, as evident in Fig. 4.6a. This is obviously caused by the strong resistance by a high volume fraction of silicon crystals in the matrix, when the material is extruded at a low temperature of 370 °C. The absence of these cracks was due to demoisturing at 150 °C for 70 min was proven to be effective for the alloy.

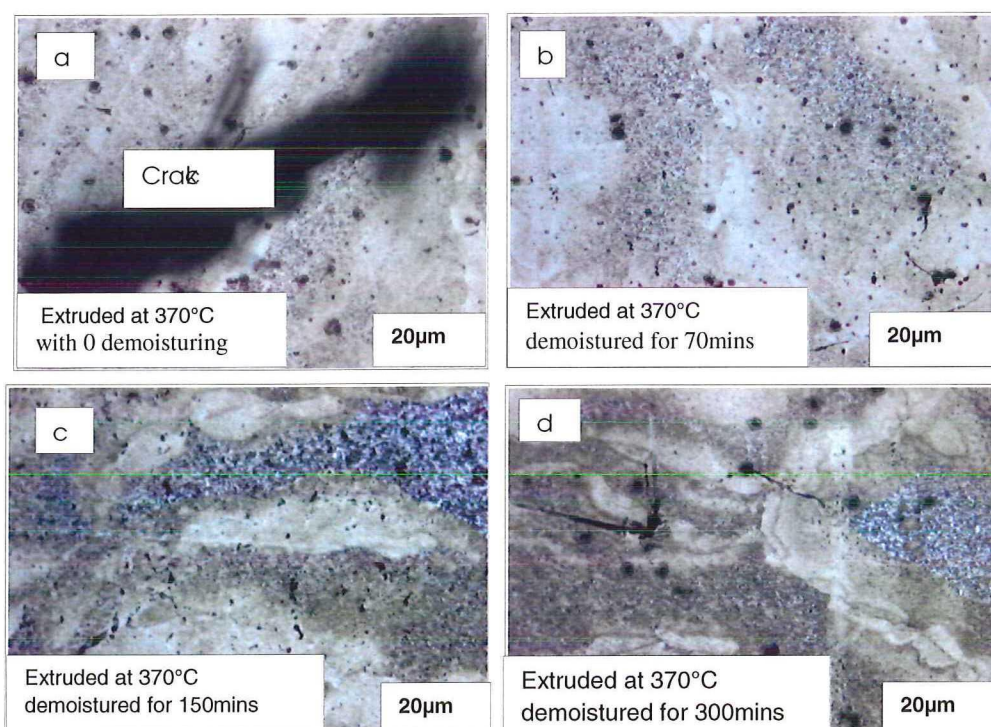


Figure 4.6. **Optical microstructures of the samples demoistured for different times: 0, 70, 150 and 300 mins.**

The influence of high temperature during isostatic pressing (HIP – 425 °C) on the sample prior to extrusion at the same temperature was investigated through an optical microstructure analysis. See Fig 4.7. The comparison between the microstructures of

the as-received HIPed sample and the extruded sample showed that the extruded microstructure is merely a carryover of the HIPed microstructure and no recognisable differences were observed after the extrusion. Close examination of these microstructures showed that they were similar to each other.

A notable feature observed in both of the microstructures is the presence of isolated patches of aluminium grains with precipitates. The presence of these isolated grains may serve as weak spots and will contribute greatly to the loss of mechanical strength at high temperatures. A balance may be made between compaction and extrusion temperatures to avoid losing the envisaged microstructure quality of the extruded material. The significant similarities between the two microstructures suggest that compaction at a high temperature is detrimental to the final strength of the alloy. Since the as-melt-spun microstructure cannot be recovered by heat treatment, it follows that it is essential to maintain a low operating temperature during compaction and extrusion in order to preserve the beneficial microstructures and properties obtained by melt spinning.

The comparison between the microstructures of the as-received extruded sample ( $C_1$ ) and those (D) that were cold compacted and then extruded in the present research showed that the features described above were not apparent in these microstructures. This might affect the final strength of the material. Therefore, a compromise should be made between extrusion and HIP of the flakes.

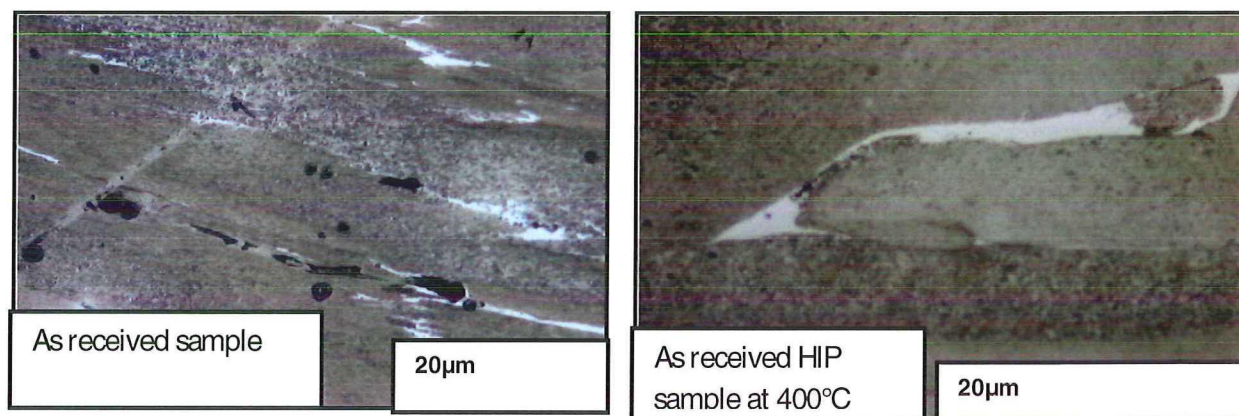
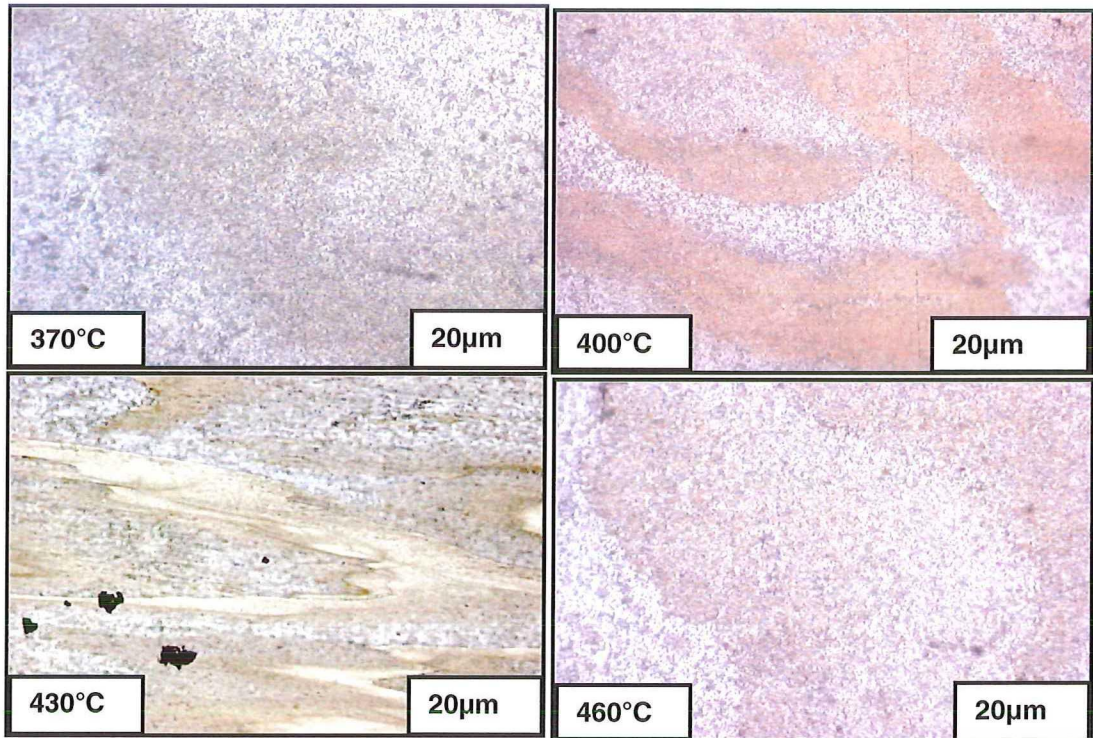


**Figure 4.7.** Microstructure images of the as received HIPed sample and extruded sample.

#### 4.1.4 The as-annealed microstructure

The report below is based upon the influence of separate elevated-temperature annealing treatments at 200, 300 and 350 °C on the microstructure of the extruded material and by extension also to the effect of extrusion temperatures (370 – 460 °C). The investigation did not show any recognizable differences between the microstructure annealed at 100 °C and that without annealing. This means that annealing at 100 °C has little effect on the sizes of crystals and dispersoids. The optical microstructures of the specimens annealed at 200 °C, prior to extrusion at 370, 400, 430 and 460 °C, are displayed in Fig. 4.8. It can be seen that some large particles in the sample after extrusion at 460 °C have been dissolved into the matrix. Apart from the colour changes from gray to orange for the most part of the microstructures, there are no other recognisable effects that are obvious at this extrusion temperature.

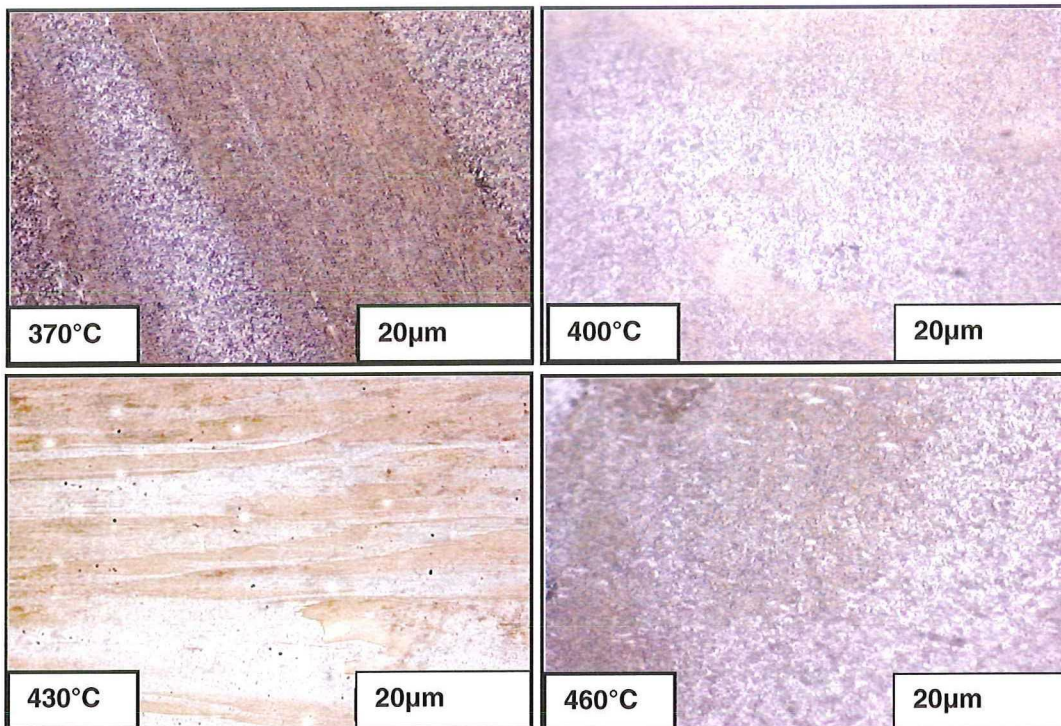
Large intermetallic particles can be noticed from the microstructure of the samples that were extruded at 430 °C. These particles were formed to lower the internal surface energy of the material at the high temperature as a preparatory ground for the coarsening of the particles. The cross-section demarcations of the flakes as evident in the extruded rods that were extruded at high temperatures and the earlier observed high-density crystals in the materials extruded at 370 °C were still visible at this temperature. What could be a source of worry on the various microstructures was the increasing inhomogeneity of particles as displayed by varying colours in the material. These are attributable to the mixed zones in the microstructure.



**Figure 4.8.** Microstructures of the samples extruded at 370, 400, 430 and 460 °C and then annealed at 200 °C for 100 hr.

Fig. 4.9 shows the optical microstructures of the samples annealed at 300 °C after the extrusion at temperatures of 370, 400, 430 and 460 °C and at a reduction ratio of 10:1. Many differences can be observed from the microstructures, which include the coarsening of the aluminium matrix as shown in the microstructure of the rod extruded at 460 °C. The features found in this microstructure can mean a lot of doom for the strength of the sample. In the microstructure of the sample that was extruded at 430 °C, large and circular white patches, which were widely distributed around the areas close to the boundaries between the phases, were also seen. Another major defect includes the increasing non-alignment in the microstructure with rising extrusion temperature.

It was interesting to note that at this temperature the microstructure of the samples extruded at 370 and 400 °C seemed similar with no visible signs of coarsening. The only recognizable difference was that though the number of intermetallic particles gradually decreased with rising extrusion temperatures, there were still some particles retained in the specimen extruded at 400 °C and higher. Owing to these observations, one could infer that the effects of annealing temperature on strength of the materials, as expected, were more pronounced with the rise in extrusion temperature.



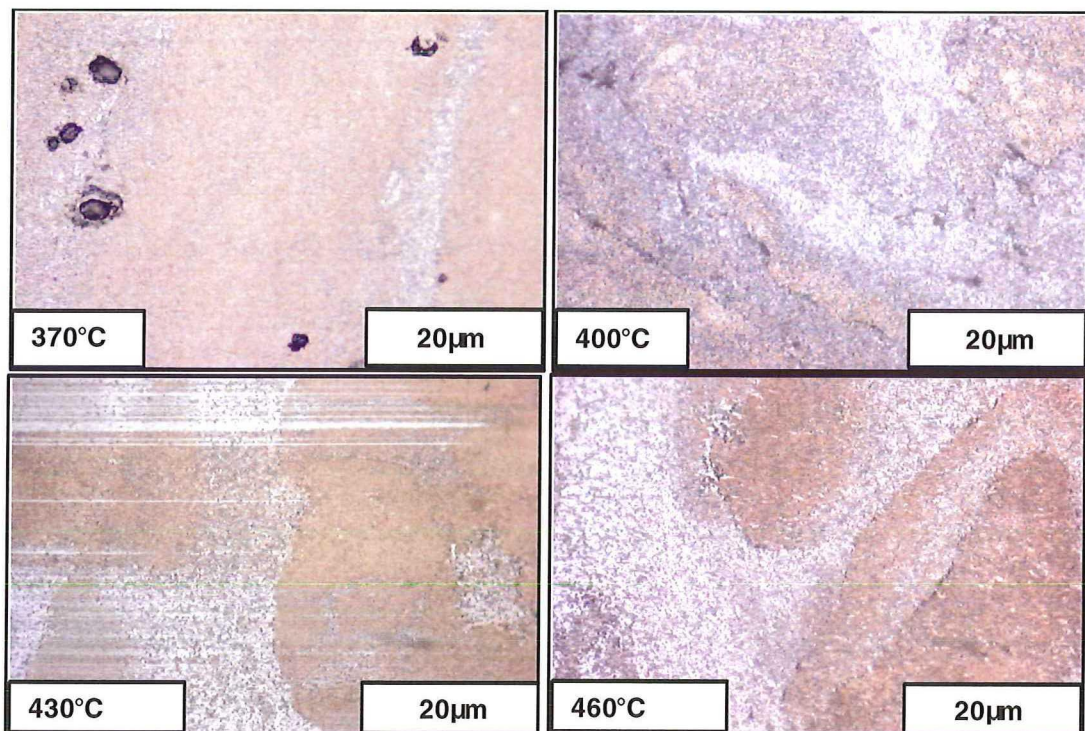
**Figure 4.9.** Microstructures of the samples extruded at 370, 400, 430 and 460 °C and then annealed at 300 °C for 100 hr.

Fig. 4.10 shows the microstructural characteristics of the material extruded at different temperatures and then annealed at 350 °C for 100 hr. The features reported below have been ascribed to the effect of extrusion temperatures on the material. The microstructure of the sample extruded at 460 °C shows a clear indication of degradation. The signs identified as pulling apart of the microstructures were observed in the material extruded at this temperature, which were parallel to the extrusion direction. This can be an indication of the effect of high-temperature annealing on the mechanical properties of the material extruded at this temperature.

The coarsening of the microstructure of the annealed material extruded at this temperature is in common with the reported increase in particle size with rising annealing temperature. Since the rate of coarsening depends on the product of diffusivity, interfacial energy and equilibrium solubility of the elements at the extrusion and annealing temperatures, it may be expected that all the factors must be exceptionally low so as to enable the alloy to maintain a fine structure at a high temperature. It is possible that annealing at a high temperature leads to particles with slightly higher misfit due to dispersion to lose coherency, resulting in that the

interfacial energy is increased, thereby increasing the coarsening rate. This, coupled with the diffusivity of the elements, is expected to increase with rising temperature.

The results generally show that 350 °C is the upper-limit temperature for the material, since notable degradation of microstructure was observed at this annealing temperature. Demoisturing was another factor that was found to have a positive influence both on the room and elevated-temperature microstructures. Less coarsening features were found in the samples extruded at 370°C that were demoistured between 60 to 70 min. However, it could be acceptable to say that extrusion temperature played a paramount role in the changes observed in the microstructure of the material after annealing. See Fig. 4.10.



**Figure 4.10.** Microstructures of the samples extruded at 370, 400, 430 and 460 °C and then annealed at 350 °C for 100 hr.

Fig.4.11 shows the optical microstructures of the samples extruded at 370 °C and then annealed at 100, 200, 300 and 350 °C for 100 hr. From these microstructures, it was only the sample annealed at 350 °C for 100 hr that had the evidence of coarsening characteristics. The samples annealed at lower temperatures possessed features similar to those seen in the material extruded at 370°C. Previous reports on the mechanisms of

coarsening and recrystallisation in aluminium alloys showed that the process of coarsening proceeded rapidly with rising annealing temperature and time [57]. The dispersed particles had double implications on the microstructure when it comes to high temperature. This is because the dissolution of these particles lowers the internal surface energy by increasing the size of the particles, leading to decreases in the hardness and strength of the material. This is especially noted in the microstructure of the sample that was annealed at 350 °C for 100 hr. The reason was that annealing at high temperature soaks up the dispersed silicon crystals and iron-containing intermetallic compounds, making it possible for diffusion and coarsening of the microstructure to proceed at a high rate. The features observed in the microstructures suggest that 350 °C might be the upper limit for this material.

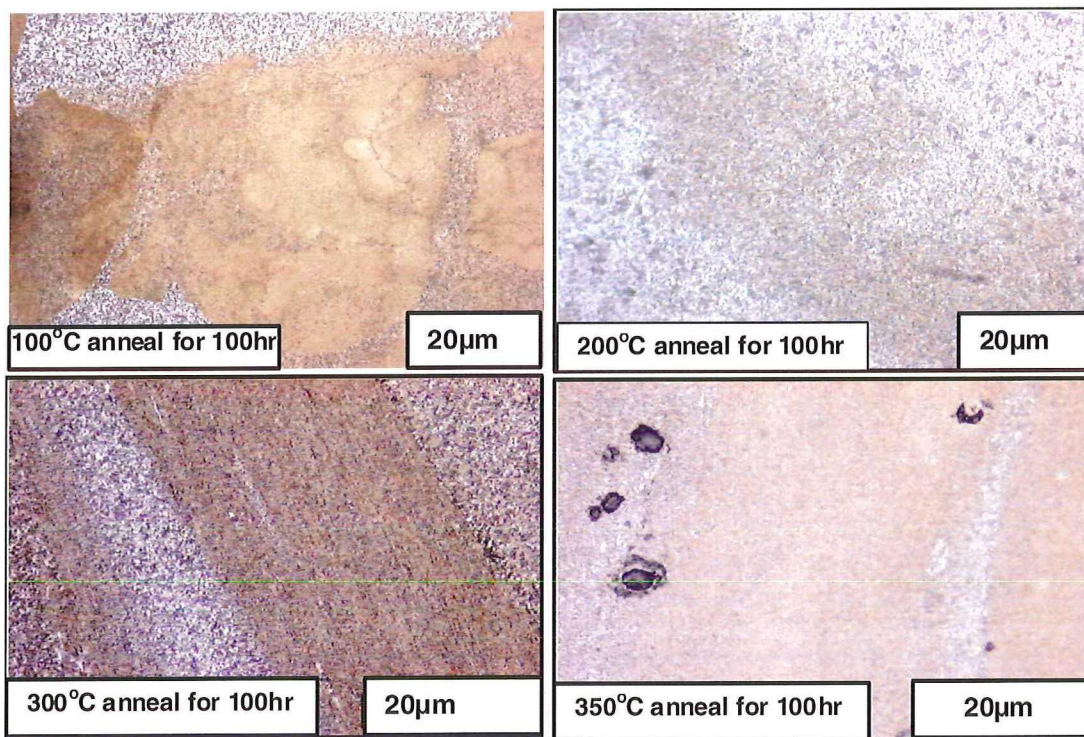


**Figure 4.11.** Microstructures of the samples extruded at 370 °C and then annealed for 100 hr at 100, 200, 300 and 350 °C.

Figure 4.12 shows the microstructures of the samples extruded at 400 °C and then annealed for 100 hr at 100, 200, 300 and 350 °C. These microstructures showed many differences that included the coarsening and weakening of the aluminium matrix. The evidence of coarsening can be found in the microstructure of the materials extruded at 400 °C and then annealed at 300 and 350 °C for 100 hr. The mechanisms of

coarsening noted in these microstructures were similar to those seen in the samples extruded at 370 °C and then annealing at 350 °C.

It was interesting to note that the microstructures of other samples annealed at 100 and 200 °C for 100 hr looked similar to each other in microstructure with no visible signs of coarsening. This suggests that, apart from the high extrusion temperature of 400 °C, annealing condition can affect the strength of this material. These two factors can also complement each other to decrease the strength of the material.

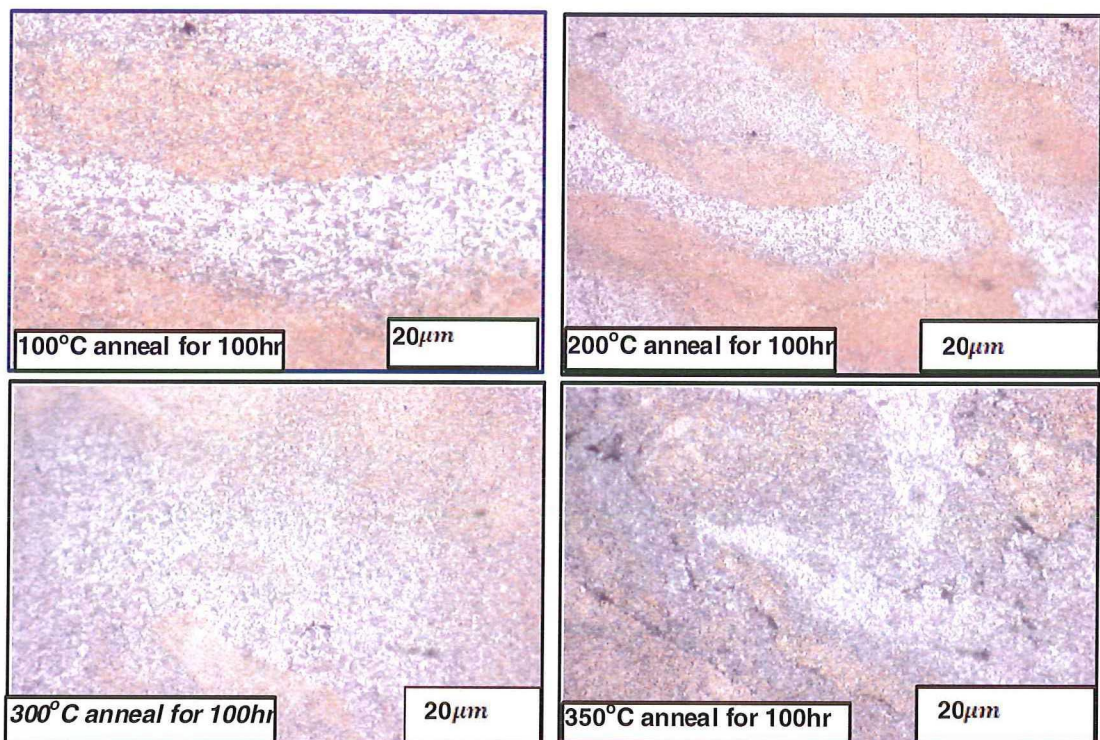


**Figure 4.12.** Microstructures for the samples extruded at 400 °C and then annealed for 100 hr at 100, 200, 300 and 350 °C.

Figure 4.13 shows the microstructures of the samples extruded at 430 °C and then annealed for 100 hr at 100, 200, 300 and 350 °C. The features seen in these microstructures suggest that with rising extrusion temperature the effect of annealing temperature becomes more severe. These include visible initiation of coarsening and weakening of the aluminium matrix in the samples annealed at temperature as low as 200 °C after 100 hr. The presence of large particles in the microstructure was the evidence of particle growth and coarsening of these particles. As stated earlier, this was caused by complementary influence of rising extrusion and annealing temperatures. The mechanisms of coarsening noted in these microstructures were

similar to those seen in the samples extruded at 370 °C and then annealing at 350 °C. However, the microstructure of the sample that was annealed at 100 °C after extruding at 430 °C showed that the structures were similar to the as-extruded material.

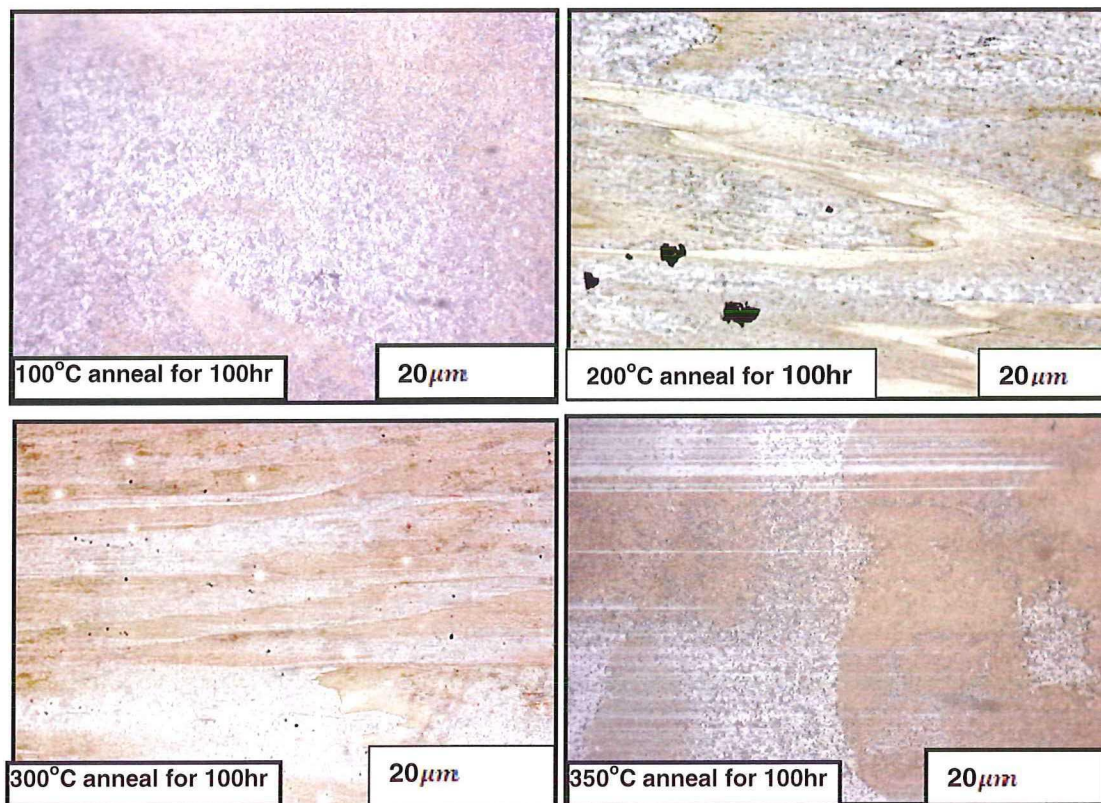


**Figure 4.13.** Microstructures of the samples extruded at 430 °C and then annealed for 100 hr at 100, 200, 300 and 350 °C.

Figure 4.14 shows the microstructures of the samples extruded at 460 °C and then annealed for 100 hr at 100, 200, 300 and 350 °C. Typical complementary mechanisms of high extrusion and annealing temperatures can be seen in these microstructures. The coarsening and tearing of the structures noted in the microstructure of the samples annealed at 200, 300 and 350 °C demonstrated that the effect of annealing temperature was strong when complemented by the extrusion of the material at the high temperature. In these microstructures, coarsening and the tearing of the aluminium matrix were enhanced by the high exposure temperature for 100 hours, thus making it possible for diffusion to proceed without much hindrance.

However, these features or defects were not observed in samples annealed at 100 °C for 100 hr. This suggested that annealing temperature was an important parameter by which the effect of coarsening of this material could be judged.

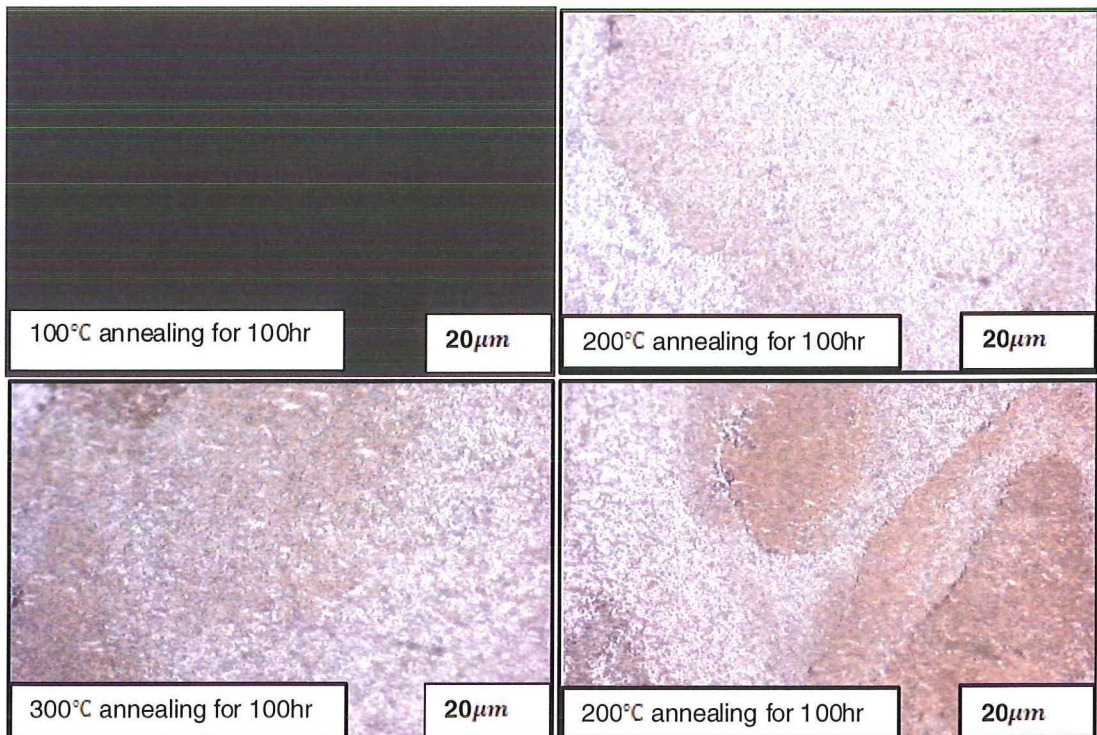


**Figure 4.14.** Microstructures of the samples extruded at 460 °C and then annealed for 100 hr at 100, 200, 300 and 350 °C.

## 4.2 Mechanical properties of the material as affected by extrusion and annealing temperatures

In order to establish the influence of extrusion temperature on the elevated-temperature mechanical properties of the material, tensile tests were carried out on the samples at the ambient temperature, 100, 200, 300 and 350 °C, in addition to hardness tests. Also included in the investigation were the effects of demisting time and long-time exposure for 100 hr at temperatures up to 350 °C on the mechanical properties of the material extruded at these temperatures. The result of these tests (microhardness, yield strength and elongation - ductility at fracture) of the material will be shown in this section.

### 4.2.1 Hardness

Micro Vickers hardness measurements were made with a 0.1 N (10 g) load using a Reichert and Leitz hardness tester. The measurements were carried out on the extruded samples after the annealing treatment at 350 °C for 100 hr. Each microhardness value was the mean value of 12 measurements. An increase in the number of measurements to 20 did not significantly reduce the standard deviation from the mean value. This indicated that the range of hardness values obtained reflected the variations in the as-extruded microstructures rather than the errors introduced in measurement. The results of the micro hardness tests are plotted in Fig. 4.15 as a function of the extrusion temperature and demoisturing time for the samples extruded at 370 °C.

Fig. 4.15 shows the changes in the microhardness values of the samples extruded at various temperatures and subsequent annealing treatment at 350 °C for 100 hr. 370(A), 370(B) and 370(C) represent the samples extruded at 370 °C prior to demoisturing for 300, 70 and 0 min, respectively. Demoisture time of 70min is the best (highest Hv).

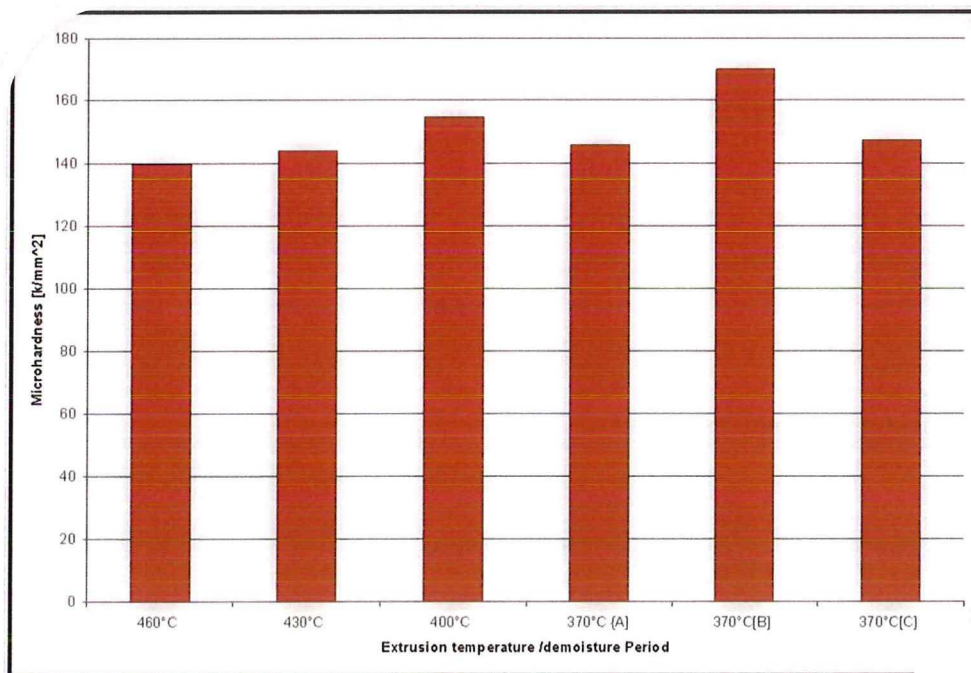


**Figure 4.15.** Changes in microhardness with extrusion temperature after annealing at 350 °C for 100 hr (370(A), 370(B) and 370(C) corresponding to demoisturing times of 300, 70 and 0 min, respectively).

It was observed that the values of microhardness increased with decreasing extrusion temperature from 140 to 170 kg/mm<sup>2</sup>. Also noted was the effect of demoisturing time on microhardness. The results showed that the sample extruded at the lowest temperature (370 °C) after demoisturing for 70 min possessed the maximum value of 170 kg/mm<sup>2</sup> against 145 kg/mm<sup>2</sup> determined in both the non-demoistured (370(C)) and demoistured for 300 min (370(A)). The result was also consistent with the earlier observed trend in extrusion pressure peaks, which shows that extrusion pressure rises with decreasing temperature. The hardness of the samples extruded at 370 °C, demoistured between 60 to 70 min increased by 16% from those extruded at higher temperatures and those demoistured for times exceeding 70 min.

The variations in hardness with the increase in extrusion temperature and demoisturing times were associated with the dissolution of the fine-scale network of silicon crystals and iron-containing intermetallic phases into the matrix solid solution. The results predict a yield strength of ~510 MN/m<sup>2</sup> at room temperature for the extrusion temperature of 370 °C and 420 MN/m<sup>2</sup> for the extrusion temperature of 460 °C after annealing for 100 hr at 350 °C, the approximate relationship  $HV = 3\sigma_y$  is valid for this alloy. The proof strength was also found to be closely related to the microhardness of this alloy. This suggests that room-temperature strength is inversely related to extrusion temperature and can be retained after annealing at temperatures up to 350 °C, with a gradual reduction in strength at higher temperatures. The result supports effectively the trend observed in relation with the microhardness of flakes after annealing for 1 hr between 50 – 450 °C.

#### **4.2.2 Tensile properties**

The results of tensile tests performed with respect to extrusion and annealing temperatures on the samples at room temperature, 200, 300 and 350°C for 100 hr are summarized in Tables 4.1 and 4.2. The tables and the stress-strain curves at room temperature, 100, 200, 300 and 350 °C indicated that significant changes occurred in the mechanical strength of the material. The 0.2% proof strength, ultimate tensile strength and elongation were varied with extrusion temperature. A close look in the

stress-strain curves showed that extrusion pressure peaks and ultimate tensile strength both decreased with rising extrusion temperature, thus suggesting that the similar mechanisms might be responsible for the very wide spread in the strength.

**Table 4.1.** Tensile strengths of the extruded material at room and elevated temperatures.

Extrusion Temp. (°C)	Demoisturing time (min)	UTS (MPa)				0.2% PS (MPa)			
		RT	200 °C	300 °C	350 °C	RT	200 °C	300 °C	350 °C
370	0	447	333	260	248	395	329	-	139
370	70	451	359	256	240	399	350	251	216
370	300	446	324	227	206	392	324	211	111
400	70	434	346	241	205	377	336	231	169
430	70	422	329	228	207	362	270	214	190
460	70	405	344	166	128	342	147	160	124

RT= room temperature. UTS = Ultimate tensile strength. 0.2%PS = 0.2% proof strength

**Table 4.2.** Tensile properties of the extruded material at room and elevated temperatures.

Extrusion Temperature (°C)	Demoisturing time (min)	Elongation (%)			
		RT	200 °C	300 °C	350 °C
370	0	4.3	7.7	-	17.9
370	70	12	13	13.7	13.38
370	300	15	16	16.3	15.9
400	70	16.4	17.1	17.3	14.1
430	70	12.6	12.4	15.9	16.3
460	70	19.0	16.7	16.9	22.2

Typical values of ultimate tensile strength and 0.2% strength indicate that annealing temperature has a significant negative influence on the mechanical strength of the material. Nearly every specimen tested lost more than 25% of its strength by annealing at 200, 300 and 350 °C, irrespective of extrusion temperature. Though the decrease in strength was general, it increased coincidentally with increasing extrusion

temperature from 370 to 460 °C and demoisturing time. However, the specimen extruded at the lowest temperature (370 °C) with a prior demoisturing time of 70 min has an ultimate strength of 451 MPa at room temperature and 359, 256 and 240 MPa at 200, 300 and 350 °C, respectively. The sample extruded at 460 °C with the same prior demoisturing time has an ultimate tensile strength of 405, 344, 166 and 128 MPa at room temperature, 200, 300 and 350°C, respectively. It is to recall that a lower volume fraction of dispersoids and silicon crystals were observed in the microstructure of the material extruded at 460 °C. This was considered to be the reason for decreasing UTS with rising extrusion temperature. See Figs. 4.16 - 5.18.

Table 4.3 gives a summary of the strain hardening range (indicated by the difference between the UTS and the 0.2% proof strength) at room temperature, 100, 200 and 300 °C versus extrusion temperature. Two features are apparent: (i) the strain hardening range goes through a maximum from the extrusion temperature of 370 to 460 °C, and ii) the difference between UTS and proof strength is small at 300 °C, for all the extrusion temperatures.

Comparison between the tensile stress-strain curves from the samples extruded at 370, 400 and 430 °C (Figs. 4.16 - 4.18) showed that the samples extruded at 400 and 430 °C underwent extensive plastic deformation before fracturing, especially at room temperature, more than those extruded at 370 °C. The extensive plastic deformation became reduced as the testing temperature rose. The samples extruded at 370 °C had less plastic deformation before fracturing at room temperature, however, they possessed higher room- and elevated-temperature tensile strengths than those extruded at higher temperatures. This may be because dislocations in the samples (370 °C) were either too low in density or too immobile to allow strains to match the elongation imposed by the testing machine due to the high resistance of the fine dispersed particles to deformation force. However, at elevated temperatures, ductility increased and equalled to that of the material extruded at 400 and 430 °C. In addition, there was no marked yielding point for the material, irrespective of extrusion temperature. Consequently, the rise in temperature increased the energy that had to be provided for dislocations to overcome the barriers they encountered during slip. This dependence

of flow stress on extrusion and annealing temperatures gave an idea about the likely stability range of the microstructure at elevated temperatures.

**Table 4.3.** Strain hardening range for the material extruded at various temperatures and tested at room temperature, 100, 200 and 300 °C.

Extrusion Temp. (°C)	Demoisturing time (min)	Strain hardening rate (given by the difference between UTS and the 0.2% proof strength)			
		RT	200 °C	300 °C	350 °C
370	0	59	4	-	109
370	70	62	9	5	24
370	300	54	0	16	95
400	70	57	10	10	36
430	70	60	59	14	17
460	70	63	197	6	4

\

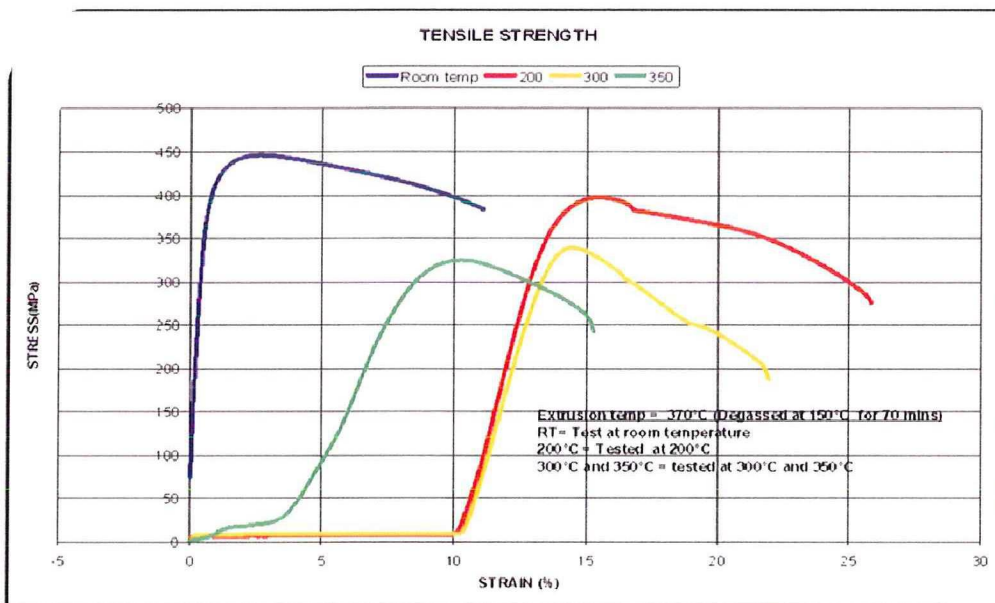


**Figure 4.16.** Stress-strain curves obtained at room temperature, 200, 300 and 350 °C after extrusion at 370 °C and annealing at 350 °C for 100 hr.

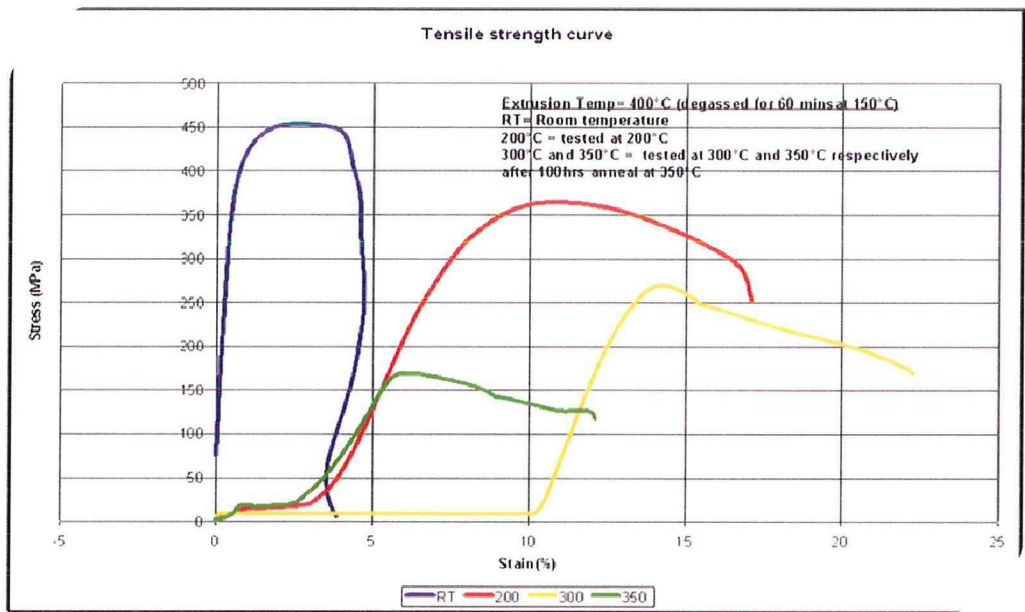


**Figure 4.17.** Stress-strain curves obtained at room temperature, 200, 300 and 350 °C after extrusion at 400 °C and annealing at 350 °C for 100 hr.

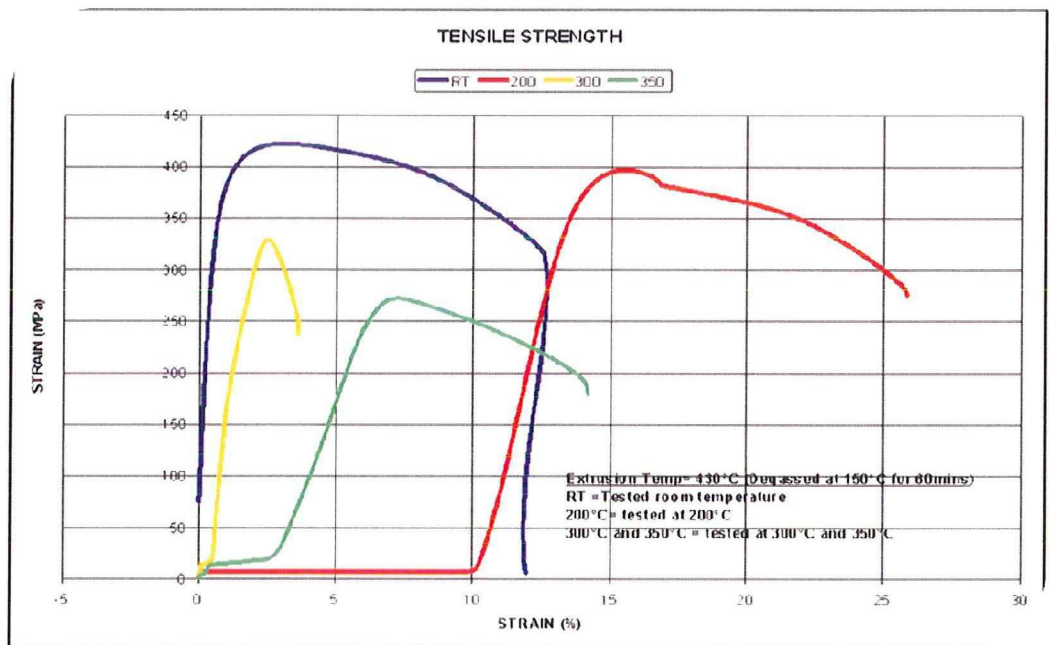


**Figure 4.18.** Stress-strain curves obtained at room temperature, 200, 300 and 350 °C after extrusion at 430 °C and annealing at 350 °C for 100 hr.

## 5. Chapter Five

### 5.1 Discussion on the characteristics of the flakes

#### 5.1.1 Relationship between composition/microstructure and cooling rate

The results given earlier are quite interesting in several aspects concerning the fundamental reasons behind the variations in the characteristics of the flakes: (i) the microstructures and composition of the flakes varied, which seemed to depend on the rapid solidification conditions and (ii) x-ray diffraction indicates that these three flakes consist of similar phases, but the thermal analyses of the flakes show differences in decomposition behaviour and their microstructures looked also quite different. Previous investigations by Bendijk and his co-workers on rapidly solidified Al-Fe-based alloys dealt with microstructural development as a function of alloy composition, presuming that the solidification conditions were identical, as in the present case [9]. Barlock *et al* also observed that for Al-Fe-Si alloys with Fe contents higher than 6 wt.% the cellular phase (Zone A) was the primary phase and acted as a nucleant for the Al phase [58]. This suggested that solidification was primarily diffusionless in this area and silicon- and iron-containing particles were entrapped in the matrix of aluminum. Although such variations in microstructure with alloy composition might occur, it should be noted that slight changes in melt-spinning conditions were the main reason for the variations in microstructure as demonstrated by the present study.

These variations in the overall appearance of the microstructures and in the composition for the whole ribbons that were seemingly of similar composition demonstrate the important effect of solidification condition on the microstructure. In the present study, three different batches of melt-spun ribbons were produced supposedly with one composition and under similar melt-spinning conditions: one whose microstructure consists of mostly Zone A and Zone B almost in equal proportion (*i.e.*  $A_1$ , 2003 batch) while two others (*i.e.*  $A_2$ , 2004 batch and  $A_3$  2005 batch) whose microstructure consist of mainly Zone B and a slight portion of Zone A. The trend in composition indicates that the extended solubility of iron also decreased over the years. See Table 3.1. These results are in agreement with those from the previous investigations by Barlock and his co-worker. Their report was on a splat

quenched material of the same alloy. They found that at a given cooling rate the maximum solubility of iron decreased with increasing silicon and vanadium concentrations. They went further to prove that whereas the silicon solubility is independent of the iron content, vanadium was not [2]. The present observations in agreement with the previous results demonstrate that melt-spinning conditions must be responsible for the variations in microstructure and composition.

The correlation between the flake thicknesses and dendrite arm spacing in the flakes indicates that a cooling rate between  $10^5$  to  $10^6$  K/sec was used in the melt spinning, which went down from flake  $A_1$  to  $A_3$ . This result is in common with the previous reports by Boswel who estimated a cooling rate as high as  $10^{10}$  K/s for the thinnest region, leading to the most extended solubility of alloying elements in the matrix. In such a situation as observed in flakes  $A_2$  and  $A_3$  with various dendrites, Boswell and his co-workers predicted a dendrite arm spacing in such a microstructure, being not larger than  $6 \mu m$  for an estimated cooling rate lower than  $10^7$  K/sec [59]. This is true for the present materials ( $A_2$  and  $A_3$ ). See Figs. 3.2b - 3.3b. In addition, flake  $A_1$ , which had mostly a featureless microstructure according to microscopic observation known as Zone A, was found to have gone through cooling at the highest solidification rate among all the three flakes studied.

In contrast, the presence of a large portion of a coarser microcrystalline structure (Zone B) found in the flakes  $A_2$  and  $A_3$  (batch 2004 and 2005) suggests a solidification rate slower than flake  $A_1$ . This was affirmed by the cooling rates calculated. All these results show that the compositions may have differed, but the changed cooling rate employed during melt spinning is the major reason for the variations in the microstructure of the flakes.

During melt-spinning solidification, cooling rate depends on several combined or aggregate of variables including the casting temperature and velocity, the speed of rotating disk and casting angle, among others. The investigations about these specific parameters were not part of the focus of this study.

Furthermore, the elevated-temperature endothermic peak observed from the thermal analysis of the sample extruded from flake  $A_3$  (the lowest cooling rate), which was previously un-noticed in the flake, showed that more silicon- and iron-containing intermetallic particles were dispersed in the material due to extrusion.

### 5.1.2 Relationship between exposure temperatures and flake microhardness

In the present discussion, it is convenient to use the microhardness of the flakes as a parameter by which the response of the material to annealing is judged. The microhardness study on the flakes showed that some variations in hardness existed across the flake thickness. These changes were considered to be due to the variations in the as-solidified microstructures in the flakes. The results obtained were consistent with the results of Jones, which was also affirmed by Thursheld *et al* who found that the microhardness of Zones A was slightly higher than Zone B [37, 55]. The results also agree with those of Tawfik and his co-workers [54] that the higher microhardness in Zone A were related to the effect of the solute atoms on the solvent lattice and the interactions of different atomic species. This type of change was typically reflected in the slight higher microhardness values on the sections of flake  $A_1$  [37, 54, 56].

The relationship between annealing temperature and the microhardness of flake  $A_3$  showed that large changes occurred as a result of annealing between 50 to 460 °C for 1 hr. The significant increases in microhardness were attributable to a high concentration of hard, fine iron-containing intermetallic phases *e.g.*  $\text{FeAl}_6$  and polygonal silicon crystals from the solid solution matrix where the thermal activation energy was enough for these intermediate phases coherent with the matrix to nucleate, leading to a sharp rise in hardness between 50 and 360 °C after annealing for 1 hr. The annealing of the flakes at a temperature above 370 °C might have led to the dissolution and growth of large particles. This makes the coarsening of the particles proceed more rapidly, with a gradual change in their chemical compositions, resulting in the depletion of these intermediate phases and the formation of needle-shaped phases, *e.g.*  $\text{FeAl}_3$ , (from the X-ray analysis) which were incoherent with the matrix.

The coarsening of the dispersoids was responsible for the observed drop in microhardness after exposure to high temperatures.

## **5.2 Discussion on the extrusion conditions and mechanical properties**

### **5.2.1 Extrusion characteristics and particles/dispersoids interactions**

The alloy described in the present investigation showed outstanding room- and high-temperature mechanical properties. The high-temperature properties are derived from the stable microstructures that prevail at temperatures until 350 °C. The occurrence of outstanding qualities in the alloy was synergically derived from high supersaturation and the extremely fine microstructure directly attributed to high solidification rates during melt spinning and high extrusion force noted with decreasing extrusion temperature. The extrusion characteristics for this material (RSPA8009) exemplified the sort of results that can be achieved by melt spinning, hence demonstrating the important role of this technique in alloy processing.

In the present work, the investigations of extrusion characteristics with respect to extrusion temperature both in the as-extruded and as-annealed microstructures were made. In the same vein, a correlation plot between extrusion peak and extrusion temperature was made, which showed a negative linearity between 370 - 430°C, which means that the alloy has a narrow extrusion temperature window/range. The investigation with optical microscopy revealed the presence of a mixture of coarse and fine particles typically in a size range of 1 - 10  $\mu\text{m}$  and the sizes increased with rising extrusion temperature. This observation goes further to indicate that apart from melt-spinning conditions the extrusion characteristics can affect the envisaged microstructure and strength of the material. The results clearly showed that extrusion pressures increased with decreasing extrusion temperature. The correlation of the temperature-compensated strain rate,  $Z$ , with extrusion pressure could not be made, because a constant reduction ratio was used during the investigation. However, the trends in the extrusion characteristics show that applying a high  $Z$  value, which corresponds to a low temperature and a high reduction ratio, will effectively enhance the mechanical properties of the material, mainly because this will raise extrusion

pressure. It is therefore of great importance to optimize the processing conditions by adjusting the process parameters, mainly extrusion temperature and reduction ratio. As shown above, their combined effect can be reflected by the temperature-compensated strain rate,  $Z$ . Hence, an appropriate process condition can be set by adjusting this parameter.

Furthermore, the changes in extrusion pressure peak with rising temperature can be explained by the microstructural observations made by Skinner and his co-workers [27]. They emphasized that a high degree of super-saturation and the formation of dispersoids were the main reasons for the high extrusion pressure requirement. This suggested that the high extrusion pressure peaks observed at a low extrusion temperature (370 °C) were attributable to Zener pinning on metal flow by these dispersoids. These dispersoids grew larger, driven by the tendency to reduce their internal surface energy, and became dissolved in the matrix of the material, when the material was exposed to a high extrusion temperature. The observation was supported by the optical microstructures of the specimens extruded between 370 – 460 °C. As extrusion temperature rose, solute diffusion, silicon crystal dissolution and dislocations would be so active that strain hardening was restricted to very low levels, as evidenced by a large slope in extrusion pressure verses ram displacement curves. The retention of the cross sections of the flakes, which were unaligned and inhomogeneous in the microstructure of the material extruded at a high temperature, occurred. This is because, when the applied stresses were not sufficiently high, the alignment of the flakes during extrusion would be limited [56].

The lowered extrusion pressure peak and the inhomogeneous microstructure with rising extrusion temperature reflect two competing mechanisms, *i.e.* strain hardening and recovery, with recovery becoming easier at higher temperatures, resulting in a decrease in the strain hardening rate. Also, dislocation mobility in Al may be further enhanced above 370 °C due to the activation of new slip systems, *e.g.* {111}, {100}, {211} and {151}, which may also contribute to the low extrusion pressure peak and strain hardening rate [50].

The higher extrusion pressure requirement of the present alloy, compared to the conventional 2000 series aluminium alloys, is considered to be due to four factors: (i) the fine second-phase network spacing, (ii) the formation of hard iron-containing intermetallic particles in the base alloy due to melt spinning and the precipitation of silicon crystals and iron-containing intermetallic particles during extrusion, (iii) almost more than 80% of the 1 wt.% vanadium added held in the solid solution, and (iv) the grain-refining effect of vanadium and significantly smaller grains in the as-melt-spun material. The apparent retention of vanadium and iron in the solid solution up to 350 °C and the maintenance of a finer grain size offset some of the softening due to the breakdown of the network structure above ~200 °C during extrusion and annealing. These factors contribute greatly to the improved strength below 350 °C, which is attributed to the precipitation of iron- and vanadium-containing intermetallic particles (Al-Fe and V-Al) and silicon crystals [54].

The rapid coarsening noted in the microstructure of the samples extruded at temperatures above 400 °C, after exposure to a temperature above 200 °C for 100 hr is primarily because silicon has a relatively high solid solubility above 200 °C especially for a long annealing time and its diffusion coefficient in aluminium is also high. The mechanism of the coarsening of the silicon crystals is by atomic diffusion from dissolving crystals to growing ones and as a result, at high temperatures almost no thermally stable internal particles are available to effectively hinder diffusion from taking place because silicon- and iron-containing precipitates have been dissolved due to high extrusion temperatures. On the other hand, extrusion creates subgrain boundaries that provide easier paths for diffusion. The coarsening of the particles in the base alloy therefore becomes inevitable at high temperatures [60].

### **5.2.2 Precipitation and transformation due to extrusion characteristics**

The results obtained from x-ray diffraction analyses, being not in common with other reports, showed that the melt-spun flakes and the extruded rods contained the same type of phases, which were identified as those already in the equilibrium state. Apparently, these were not consistent with other x-ray investigations of melt-spun flakes and extruded Al-Fe-Si-V alloys. Similar result reoccurred after repeated tests to

investigate the influence of extrusion temperature (370 – 460 °C) and subsequent annealing treatment at 200, 300 and 350 °C for 100 hr, which was used as the process parameter to study the structural evolutions in the material. The observed decreasing peaks in the diffraction lines with rising extrusion temperature meant that the sizes of particles in this material were smaller or more refined at a lower extrusion temperature.

The lattice parameters of the as-extruded matrices calculated from the  $K_{\alpha_1}$  reflection after separation from the  $K_{\alpha_2}$  component showed that the average lattice parameter of the aluminum matrix in the extruded material decreased from 0.40505 to 0.40481 *nm* over the extrusion temperature range from 460 to 370 °C. The decrease was apparently attributed to the precipitation of the supersaturated solutes: iron and silicon tend to decrease the lattice size of aluminium and are capable of overcoming the reverse effect given by vanadium. Vanadium has the least solubility in aluminium, compared to iron and silicon. The combined effects of iron and silicon in the Al solid solution will decrease the lattice constant independently, while vanadium will do the reverse. In this case, the crystals of vanadium phase are increasingly dissolved in the matrix with rising extrusion temperature, thus accounting for the disparity in lattice parameter values. In addition, the increased breadths exhibited by the as-extruded matrices, which decreased progressively with rising extrusion temperature were ascribed to stresses and strains resulting from high pressure required for deformation at a low extrusion temperature (370 °C).

Another interesting observation was the increase in the value of lattice parameter of the as- received sample, compacted by hot isostatic pressing at 425 °C prior to the extrusion at the same temperature to 4.0499 *nm*. The implication of these results was that degassing at a high temperature had similar effect on the alloy as extrusion at the high temperature. This is because during compaction, the fine grained material is usually subjected to reheating and precipitation and coarsening can develop as a result. Going by this principle, the improvement of mechanical properties by extrusion can be lost, if the compaction temperature is not checked. To avoid the undesirable coarsening of the microstructure during compaction or practical use, it is of great

importance that a balance between the degassing and extrusion temperatures in order to have a better microstructure and mechanical property during practical use of this material.

### **5.2.3 Mechanical properties in relation to extrusion and annealing temperatures**

In general, the strength of the alloy is attributed to the fine grained nature of the melt-spun microstructure containing silicon and iron precipitates, *i.e.* a Hall-Petch type of relationship. The microhardness and tensile strength tests showed that a significant decrease occurred with rising extrusion temperature for both the as-extruded and annealed samples at room and elevated temperatures. This can be attributable to the influence of temperature on the diffusivity, equilibrium solubility and the interfacial energy of the alloy. This is especially evident in the samples extruded above 400 °C and annealed at a higher temperature for 100 hr. The microstructure is unstable, if the total interfacial free energy is not at its minimum. As a result, small precipitates of a high density in the matrix tend to coarsen into larger particles of a lower density with a lower total interfacial energy. Optical microscopy investigation confirmed the relationship between the coarsening of the precipitates with rising extrusion temperature. As with grain growth, the rate of coarsening increases with temperature and this is of particular concern in the design of materials for high-temperature applications.

In addition, melt-spun alloy specimens contained particles of a range of sizes due to the differences in the time of nucleation and growth rate. At a high temperature, if diffusion rate changes, there will be a concentration gradient in the matrix in order to reduce the total free energy, which will cause solutes to diffuse in the direction of the larger particles away from the smallest, so that small particles will disappear while large particles grow. The overall result is that the total number of particles decreases and the mean radius increases with time. Since diffusivity and equilibrium solubility increase exponentially with temperature, the rate of coarsening will increase rapidly with increasing annealing temperature.

## 6. Chapter Six

### 6.1 Conclusions

The results obtained from this experimental research may be divided into two aspects: (i) the characterisation of the three batches of melt-spun Al-Fe-V-Si (AA8009) flakes and (ii) the optimization of extrusion conditions, focused on extrusion temperature and annealing treatment to enhance the elevated-temperature mechanical properties of the material. The details of the conclusions are summarised below in two parts.

#### Part 1: Evaluation of the characteristics of melt-spun ribbons

1. The results of the characterisation of three batches of melt-spun Al-Fe-V-Si (AA8009) flakes coded:  $A_1$ ,  $A_2$  and  $A_3$  corresponding to the flakes produced in 2003, 2004 and 2005, respectively, varied significantly. This is based upon the microstructures, compositions and thermal analyses. Flake  $A_1$  consisted of the feature-less Zone A and microcrystalline Zone B microstructures in a ratio of 40 to 60, while flakes  $A_2$  and  $A_3$  consisted predominantly of the coarser microcrystalline (highly dendritic) Zone B microstructure. The variation in the as-melt-spun microstructure was considered to be due to variations in solidification rate.
2. In the correlation analyses between the flake thicknesses and dendrite arm spacing, the cooling rate used during the melt-spinning operations decreased over the years (2003 to 2005) from  $5.2 \times 10^6$  to  $2.14 \times 10^5 \text{ Ksec}^{-1}$ . These variations in cooling rate were strongly dependent upon variations in melt-spinning conditions.
3. The microhardness study on flake  $A_3$  after annealing treatments at temperatures up to 450 °C for 1 hr showed that after the temperature of 350 °C, the microhardness of the flakes started decreasing remarkably. This is considered to be due to the coarsening of the initial microstructure and dissolution of the dispersed crystals into the matrix of the flakes. This result has very important implications for the development of high-performance elevated-temperature aluminium alloys.

## Part 2: Evaluation of extrusion characteristics

4. The extrusion of the melt-spun Al-Fe-V-Si (AA8009) alloy was characterised by a high pressure requirement rising with decreasing extrusion temperature. This was also the case for the slopes in the extrusion pressure versus ram displacement curves. This was considered to be caused by strong internal resistance to metal flow due to a high volume fraction of dispersoids with decreasing temperature.
5. The material exhibited a narrow extrudable temperature range between (370 – 430 °C): at a low extrusion temperature of 370 °C, the power limit of the press was approached, while after extrusion at a high temperature of 460 °C at a reduction ratio of 10:1, the as-extruded microstructure showed that the flakes were unaligned due to a low extrusion force. A dip was also seen in the correlation curve between extrusion pressure peak and temperature above 430 °C. The low extrusion pressure peak and the unaligned microstructure with rising temperature reflect two competing mechanisms, *i.e.* strain hardening and recovery, with recovery becoming easier at higher temperatures, resulting in a decrease in the strain hardening rate with rising extrusion temperature.
6. The impact of demoisturing time on the extrusion peaks and the as-extruded microstructure were also investigated. Using an extrusion temperature of 370 °C, the results showed that a demoisturing time between 60 - 70 min at 150 °C was optimum for this alloy prior to its extrusion. This conclusion was based on the compromise between high extrusion pressure requirement and fractures free microstructure in the demoistured samples after extrusion at the temperatures of 370 °C as opposed to low extrusion pressure peaks, which were apparent in the over-demoistured samples (~300 min) and cracked surfaces observed in the microstructures of the undemoistured samples. This demoisturing time was considered the best in terms of microstructure and mechanical properties.
7. The reduction in the volume fraction of post-extrusion intermetallic crystals and the increase in their sizes with rising extrusion temperature were also observed. This was considered to be due to increased dissolution of crystals in the matrix

with rising extrusion temperature. This can also be an indication of increased diffusion of crystals with rising temperature.

8. The elevated-temperature mechanical properties of the melt-spun Al-Fe-V-Si (AA8009) material were evaluated between 23 and 350 °C, with particular reference to the extrusion and annealing temperatures. As the annealing temperature was raised, the dispersoids coarsened, and bands of coarsened grains were formed, parallel to the extrusion direction. Thus, both hardness and tensile strength decreased as the coarsening increases. The coarsening rate was correlated with extrusion temperature. Strain hardening also dropped with increasing extrusion temperature (370 – 460 °C). The reason being that extrusion being a thermal process created subgrain boundaries that provided easier paths for diffusion to proceed. The coarsening of silicon crystals and other intermetallic phases in the alloy, therefore, became inevitable at high temperatures. This is closely related to the low tensile strengths noted with an increase in the exposure temperatures, as can be seen from the stress -train curves.
9. Annealing at high temperatures for 100 hr after extrusion had a negative impact on the microstructure and mechanical strength of the material. The coarsening of the microstructure and the eventual reduction in tensile strength after annealing at high temperatures above 300 °C for 100 hr was noted. A correlation with rising extrusion temperatures was also apparent. This was considered to be due to the dissolution of the dispersoids after annealing for a long time at these temperatures. The annealing could have caused an increase in the sizes of crystals. The non-uniformity and growth of larger particles sizes at the expense of smaller ones to decrease their surface energy obviously promoted the coarsening of microstructures, when the material was exposed to a high temperature during tensile tests.

## 7. Recommendations

Several dedicated research efforts aimed at achieving a high strength to weight ratio were paid off with notable improvements in the elevated-temperature mechanical properties of aluminum-based materials. The relatively low cost of aluminum in comparison to titanium was also an added attraction. Previous research in this area pointed to the AA8009 [Al-Fe-Si-V] aluminum alloy as a good representative of the elevated-temperature alloy, due to the low diffusivities and low interfacial energies of the alloy elements (*e.g.* Fe and V). However, most of the improvements were only realized after the invention of the melt-spinning technique by Mr. Pol Duwez at the California Institute of Technology and intensive research in Allied Signal. It is now possible to produce alloys with grain sizes in a range of micrometers or nanometers and even those that are usually coarse grained by this technique. The product from the melt-spinning process is usually ribbons of small thicknesses and these are compacted and hot extruded in order to produce bulk material, while retaining the majority of the ultra-fine microstructure of the initial ribbons.

This study investigated the reason for the variations in the properties of three batches of ribbons and optimized the elevated-temperature mechanical properties of the bulk material from one batch. These ribbons were presumably produced using similar processing conditions and compositions. At the end of this study, a number of recommendations can be given.

- 1) The results obtained from this study proved that the processing conditions and subsequently the ribbons differed in many aspects including composition, microstructure and thickness. The correlation between the results and the cooling rate used during melt spinning showed that the cooling rates of these ribbons were quite different (decreased over the years). This led to the variations in the properties of the bulk materials. A cooling rate of  $5.0 \times 10^6$  K/s was determined for flake A<sub>1</sub>, which had the best microstructure. This cooling rate could be used as the critical lower limit for this alloy. It is recommended that the melt spinning parameters be upscaled to improve the cooling rate and to ensure that it does not change after each batch.

- 2) The comparison of the results in composition, thermal transformation sequence, lattice parameter and X-ray diffraction with the literature data showed that the ribbons contained an equilibrium silicide phase  $\text{Al}_{12}(\text{Fe},\text{V})_3\text{Si}_2$ , which had a primitive lattice, instead of the bcc phase  $\text{Al}_{13}(\text{Fe},\text{V})_3\text{Si}$  which is described in the literature as a stable phase at elevated temperatures. They can be distinguished from each other by composition and lattice parameter. It is recommended that the alloy design be reviewed with a view to obtain the exact silicide phase in the material. See ref.28.
- 3) The comparison between the microstructure of the as-received material (compacted by hot isostatic pressing at 425 °C) and the as-cold-compacted microstructure (as used in this study) showed that undesirable reheating, precipitation and coarsening of the microstructure due to exposure to high temperatures were prevented by cold compaction. The melt-spun microstructures were also retained in the compacted billets. It is therefore recommended that lower temperature be used for the compaction of this material in order to obtain a good post-compaction microstructure.
- 4) The microstructures from these two compaction methods were also compared with their extruded microstructures. This investigation revealed that there was no distinction between the HIP and its extruded microstructures, because similar temperatures were used for compaction and extrusion. This result increases the need to widen the temperatures for the compaction and extrusion of this material. Based on this result, it is advised that the temperature between extrusion and compaction be spaced for this material.
- 5) The comparison between the microstructure and strength of the materials extruded at temperatures from 370 to 460 °C showed that the material extruded at 370 °C had the best microstructure and overall mechanical strength. It is therefore recommended that an extrusion temperature of 370 °C or lower depending on the limit of the extrusion press be used in order to improve the microstructure and optimize the room- and elevated-temperature strength of this alloy.

- 6) Demoisturing in the way as employed in this study was quite a new approach to increase the alignment of the ribbons and the strength of the extruded material. In this study, demoisturing of the compacted billet at 150 °C between 60 - 70 min improved the surface quality and extrusion pressures of this material. It is therefore recommended that demoisturing be used to improve the quality of the material especially when extruded at low temperatures, but necessary effort should be made to control the timing.
  
- 7) Since annealing above 200 °C for 100 hr led to drastic reductions in the strength of the material especially at elevated temperatures, it is recommended that annealing above 200 °C be avoided for this material.

## 8. References

- [1] P. Duwez, "Rapidly chilled amorphous alloy films", U.S. Patent 3297436, Trans. Am. Soc. Metals, **60** (1967), pp. 607-626.
- [2] C.M. Adam, B. H. Kear, B. C. Giessen and M. Cohen, "Rapidly solidified amorphous and crystalline alloys", Materials Research Society Proceedings, **8**, Materials Research Society, Pittsburgh, PA (1982), pp. 411-420.
- [3] C.M. Hildeman, Citation and references; US Patent 4379 719, 1983.
- [4] N.J. Kim and S.K. Das, Citation and references; "Science and technology of rapidly quenched alloys", Materials Research Society, L. Johnson (eds.), Pittsburgh, PA. (1987) p.35
- [5] D.J. Skinner, R.L. Bye, D. Raybould and A.M. Brown, "Dispersion strengthened Al-Fe-V-Si alloys", Scr. Met., **20** (1986), pp. 867-872
- [6] S.L. Sobolev, "Rapid solidification under nonequilibrium conditions", Physical Rev. E, **55-6** (1997), pp. 6845 -6854.
- [7] A. Inoue, "Amorphous, nanoquasicrystalline and nanocrystalline alloys in Al-based systems", Prog. Mat. Sci., **43** (1998), pp. 365-520.
- [8] M.A. Rodriguez and D.J. Skinner, "Compositional analysis of the cubic silicide intermetallics in dispersion strengthened Al-Fe-V-Si alloys", Mat. Sci. Let., **9**(1990), pp. 1292-1293.
- [9] A. Bendijk, R. Delhez, L. Katgerman, Th.H. De Keijser, E.J. Mittemeijer and N.M. van der Pers, "Characterization of Al-Si-alloys rapidly quenched from melt", Mat. Sci. & Eng., **15** (1980), pp. 2803-2810.
- [10] H. Fredrickson, A. Ostlund and H. Soderhjelms, "A theoretical study of the transition from crystalline to amorphous structure in alloys produced by the melt spinning", Rapid Quenching of Metals, **3-7** (1984), pp.187-200.

- [11] L. Katgerman and P.J. van den Brinck, "A mathematical model for melt spinning of crystalline alloys", Proceedings 4th International Conference on Rapidly Quenched Metals, Sendai, Japan (1981), pp. 61–4.
- [12] H.H. Lieberman: "The dependence of the geometry of glassy alloy ribbons on the chill block melt-spinning process parameter", *Mat. Sci. & Eng.*, **43** (1980), pp. 203-210.
- [13] T.W. Clyne, "Numerical modeling of rapid solidification topics on nucleation", Rapid Solidification held at the Foundry Institute, the Technical University of Aachen, FRG (1983), pp. 96–130.
- [14] D.R. Poirier and G.H. Geiger, *Transport Phenomena in Materials Processing*, The 1st Ed., TMS, Warrendale, PA, 1994.
- [15] S. Kavesh, "Principles of fabrication of metallic glass", American Society for Metals, Metals Park, OH, (1978), pp. 36-73.
- [16] E.S. Humphrey, P.J. Warren, J.M. Titchmarsh and A. Cerezo, "Microstructure and chemistry of Al–V–Fe–Si nanoquasicrystalline alloys", *Mat. Sci. & Eng. A*, **304**, (2001), pp. 844-848.
- [17] D. Rayboulod, "Forming of rapidly solidified elevated temperature aluminium alloys produced by planner flow casting", *Dispersion Strengthened Aluminum Alloys*, Phoenix, Arizona; USA (1988), pp.199-215.
- [18] J.V. Wood, "Rapid solidification processes and perspective part II", *Mat. & Design*, **4** (1983), pp. 712-715.
- [19] H. Jones, "Microstructure of rapidly solidified materials", *Mat. Sci. & Eng.*, **19** (1984) pp. 1043-1056.
- [20] S. Yaneva, "Structure development in rapidly solidified Al–Fe–V–Si ribbons", *Mat. Sci. & Eng. A.*, **373** (2004), pp. 90-98.

- [21] A. Kalkanli and S. Angi, "Effect of cooling rate on microstructure and high temperature stability of rapidly solidified Al-Fe-V-Si alloys", *Powder Met.*, **42**, No. 4(1999), pp. 359-365.
- [21] A. Ruder and D. Elieze, "Microstructure and thermal stability of a rapidly solidified Al-4Er alloy", *Mat. Sci. & Eng.*, **25** (1990), pp. 3541.
- [22] M.A. Rodriguez and D.J. Skinner: "Compositional analysis of the cubic silicide intermetallics in dispersion strengthened Al-Fe-V-Si alloys", *Mat. Sci. Let.*, **9** (1990), pp. 1292-1293.
- [23] H. Jones: "Observations on a structural Transition in aluminium alloys hardened by rapid solidification", *Mat. Sci. & Eng.*, **5** (1969), pp. 1-18.
- [24] L.A. Bendersky, A. J. McAlister and F.S Biancaniello, "Phase transformation during annealing of rapidly solidified Al-rich Al-Fe-Si alloys", *Mater. Sci. & Eng.*, **19A** (1988). pp. 2893-2900.
- [25] W.J. Park, S. Ahn and N.J. Kim, "Evolution of microstructure in a rapidly solidified Al-Fe-V-Si alloy", *Mat. Sci. & Eng. A*, **189** (1994), pp. 291-299.
- [26] R. Tongri, E.J. Minay, R.P. Thackray, R.J. Dashwood and H.B. McShane, "Microstructures and their stability in rapidly solidified Al-Fe-(V,Si) alloy powders", *Mat. Sci. & Eng.*, **36** (2001), pp. 1845-1856.
- [27] Allied Signal Inc., "Dispersion-strengthened aluminium alloy", Patent statement for AA8009 (FV0812).
- [28] D.J. Skinner, "Physical metallurgy of dispersion strengthened Al-Fe-V-Si alloys" in *Dispersion Strengthened Aluminium Alloys*, as edited by Y.-W. Kim and W.M.Griffith. The Mineral, Metals and Material Society Annual Meeting, Warrendale, PA, (1988), pp. 437-450.
- [29] S. Lee, D.Y. Kim and J.L. Nack, "Correlation of microstructure and fracture toughness of a rapid solidification-powder metallurgy Al-Fe-V-Si alloy," *Mat. Sci. & Eng. A*, **147** (1991), pp. 33-44.

- [30] L.M. Peng, S.J. Zhu, F.G. Wang, H.R. Chen, Z.Y. Ma and J. Bi, "High temperature creep deformation of an Al-Fe-V-Si Alloy", *Mat. Sci. & Eng. A*, **259** (1999), pp. 25-33.
- [31] U. Orhan, T. Karaaslan and M. Keskin, "Production and structure of rapidly solidified Al-Si alloys", *Turk. J. Physics*, **25** (2001), pp. 455-466.
- [32] H. Jones, "On the prediction of lattice parameter vs. concentration for solid solutions extended by rapid quenching from the melt", *Scripta Mater.*, **17** (1983), pp. 97-100.
- [33] V.V. Tcherdyntsev, S.D. Kaloshkin, D.V. Gunderov, E.A. Afonina, I.G. Brodova, V.V. Stolyarov, Yu.V. Baldokhin, E.V. Shelekhov and I.A. Tomilin, "Phase composition and microhardness of rapidly solidified Al-Fe alloys after high pressure torsion deformation", *Mat. Sci. & Eng. A*, **375-377** (2004), pp. 888-893.
- [34] V.G. Rivlin and G.V. Raynor, "Critical evaluation of constitution of aluminium-iron-silicon system", *Intern. Met. Review*, **3** (1981), pp. 133-152.
- [35] P. Morgan, "The diagram of state for Fe-Al solid solution", *Met. Trans.*, **1** (1970), pp. 331-2332.
- [36] E. Gebhardt and G. Joseph: "Metals Handbook, Metallography, Structures and Phase Diagrams", 8th Edition, (1961), P. 310.
- [37] H.J. Steinbach, C. Diepersa and B. Beckermann, "Transient growth and interaction of equiaxed dendrites", *J. of Crystal Growth*, **275** (2005), pp. 624-638.
- [38] H.K.D.H. Bhadeshia, <http://www.msm.cam.ac.uk/phase-trans/abstracts>.
- [39] Y. Birol and M. Karlik, "Microstructure of a thin-cast Al-Fe-Mn-Si strip", *Mat. Sci. & Eng.*, **31** (1996), pp. 2139-2143

- [40] B. Cantor, "Development of microstructure in advanced solidification processing", *Micron*, **25** (1994), pp.551-556.
- [41] P.G. Boswell and G. Chadwick, "The grain size of splat quenched alloys", *Scripta Met.*, **2** (1977), pp. 459-465.
- [42] A. Kirin, A. Tonejc and A. Bonefačić, "Change in the lattice parameter of aluminium under the influence of rapid quenching from the liquid state", *Scr. Met. & Mat.*, **3** (1969), pp. 943-946.
- [43] M. Yan, W.Z. Zhu and B. Cantor, "The microstructure of as-melt-spun Al-7%Si-0.3%Mg alloy and its variation in continuous heat treatment", *Mat. Sci. and Eng. A*, **284** (2000), pp. 77-83.
- [44] B. D. Cullity, "Elements of x-ray diffraction", The 3rd Edition, B.D. Cullity (1996), pp. 137-145.
- [45] E.J. Mittemeijer and R. Delhez, "Concentration variations within small crystallites studied by x-ray diffraction line profile analysis", *J. Appl. Phys.*, **49** (1978), pp. 3875-3879
- [46] R. Jenkins and R.L. Snyder, "Introduction to x-ray powder diffractometry", John Wiley Publications, The 4<sup>th</sup> Eds (1996), p. 45.
- [47] R. Dunlap, "Formation, structure, and crystallization of metastable quasi-crystalline Al-transition metal alloys prepared by rapid solidification", *Can. J. Phys.*, **63** (1985) pp. 267-282.
- [48] C. M. Allen, K.A.Q. O'Reilly, P.V. Evans and B. Cantor, "The effect of vanadium and grain refiner additions on the nucleation of secondary phases in 1xxx Al alloys", *Acta Mat.*, **47**, No 17, (1999), pp. 4387-4403.
- [49] N.J. Kim, S.K. Das, L.E. Tenhover, L. E. Tanner and W. L. Johnson (eds.), "Science and Technology of Rapidly Quenched Alloys", Materials Research Society, Pittsburgh, PA (1987), pp. 35-40.

- [50] S. Mitra, "Elevated temperature mechanical properties of a rapidly solidified Al-Fe-V-Si alloy", *Scripta Met. & Mat.*, **27** (1992), pp. 521-526.
- [51] C.R. Ho and B. Cantor, "Heterogeneous nucleation of solidification of Si in Al-Si and Al-Si-P alloys", *Acta Metall. Mater.*, **43** (1995), pp. 3231-3246.
- [52] V.I. Surikov, M.K. Borzhitskaya, A.K. Shtol'ts, V.L. Zagryazhskii and P.V. Gel'd, "The structure and superconducting behaviour of some V-Al binary alloys and of ternary 'β-W' alloys based on the V-Al", *Fiz. Met. Metalloved.*, (1970), pp. 1167-1170
- [53] N.L. Tawfik, "Mechanical properties of rapidly solidified ribbons of some Al-Si based alloys", *J.Mat. Sci.*, **32** (1997), pp. 2997-3000.
- [54] G. Thuishield and M.J. Stowell, "Mechanical properties of Al-8wt%Fe -based alloys prepared by rapid quenching from liquid state", *Mat & Eng.*, **9** (1974), pp. 1644-1660.
- [55] J. Zhou, J. Duszczuk and B.M. Korevaar, "Mechanical response and structural development during the hot extrusion of a rapidly solidified Al-20Si-7.5Ni-3Cu-1Mg alloy powder", *J. Mat. Sci.*, **27** (1992), pp. 3856-3868.
- [56] P.Cottrell and P.R. Mould, "Recrystallisation and Grain Growth in Metals", Surrey University Press, London (1976), P.54.
- [57] J.G. Barlock and L.F. Mondolfo, "Structure of some aluminium-iron-magnesium-manganese-silicon alloys", *Z. Metallkd.*, **66** (1975), pp. 605-611.
- [58] P.G. Boswell and G. Chadwick, "The grain size of splat quenched alloys", *Scr. Met.* **6** (1977), pp. 459-465.
- [59] J. Zhou and J. Duszczuk, "Fracture features of a silicon-dispersed aluminium alloy extruded from rapidly solidified powder", *J. Mat. Sci.*, **25** (1990), pp. 4541 - 4548.